Determination of the reconstruction efficiency of low energy π^0 mesons at the *BABAR* experiment

Diplomarbeit
zur Erlangung des akademischen Grades
Diplom-Physiker

vorgelegt von

Clemens Räder

geboren in Eberswalde

Institut für Kern- und Teilchenphysik
Fachrichtung Physik
Fakultät Mathematik und Naturwissenschaften
der Technischen Universität Dresden
2007

1. Gutachter: Prof. Dr. Michael Kobel

2. Gutachter: Dr. Heiko Lacker

Datum des Einreichens der Arbeit: 19. 03. 2007

Kurzfassung

In der vorgelegten Arbeit wird die Effizienz für die Rekonstruktion von π^0 Mesonen im *BABAR* Detektor mit einem mittleren rekonstruierten Impuls von 220 MeV/c bestimmt. Bisherige Messungen haben die π^0 Effizienz des *BABAR* Detektors nur für hochenergetische π^0 Mesonen aus τ Ereignissen und D^0 Zerfällen bestimmt und nicht in einer geeigneten B Meson Zerfallsumgebung. Die durchgeführte Messung basiert auf einem Datensatz von ca. 210 Millionen $e^+e^- \to \Upsilon(4S) \to B\overline{B}$ Ereignissen, die mit dem *BABAR* Experiment in den Jahren 1999 bis 2004 aufgezeichnet wurden. Für die Bestimmung der π^0 Rekonstruktionseffizienz im *BABAR* Detektor wird der B-Meson Zerfall $B^0 \to D^{*-}\pi^+$ mit $D^{*-} \to D^-\pi^0$ selektiert. Rekonstruiert man die Zerfälle ohne das π^0 bei der Rekonstruktion zu verlangen als $B^0 \to D^-\pi^+$, bilden sie im Spektrum der im e^+e^- Schwerpunktsystem definierten kinematischen Variable $\Delta E = E^*_B - E^*_{beam}$ eine charakteristische Anhäufung bei negativen Werten. Die mit einem „*“ gekennzeichneten Variablen sind dabei ebenfalls im e^+e^- Schwerpunktsystem definiert. Ihre Gesamtzahl wird aus einen gebinnten χ^2 Fit an die gemessene ΔE Verteilung extrahiert, der auf simulierten Ereignissen validiert wird. Verlangt man zur Rekonstruktion des Zerfalls $B^0 \to D^{*-}\pi^+$ das langsame π^0, so zeigt die gemessene ΔE Verteilung einen Peak um Null. Wiederum kann mittels eines χ^2 Fits die Anzahl der so rekonstruierten Signalereignisse extrahiert werden. Die π^0 Effizienz des *BABAR* Detektors wird über das Verhältnis der Ereignisse bestimmt in denen das π^0 zur Rekonstruktion des B-Meson Zerfalls verlangt wird zur Anzahl der Ereignisse in denen es nicht zur Rekonstruktion verlangt wird. In der Analyse wurde für das relative Verhältnis der π^0 Effizienz im *BABAR* Detektor zwischen Daten und Simulation ein Wert von $\frac{\varepsilon_{Data}}{\varepsilon_{MC}} = (90.0 \pm 6.6_{stat} \pm 0.4_{sys})\%$ gemessen. Das Ergebnis ist innerhalb der Fehler konsistent mit den Resultaten aus vorangegangenen Studien.

Abstract

The presented analysis determines the reconstruction efficiency of π^0 mesons with the *BABAR* detector with an average reconstructed momentum of 220 MeV/c. Previous studies have measured the π^0 efficiency of the *BABAR* detector for high energy π^0 mesons using τ events and D^0 decays but not in a dedicated B meson decay environment. The measurement is based on a dataset of approx. 210 million $e^+e^- \to \Upsilon(4S) \to B\overline{B}$ events, recorded at the *BABAR* experiment from 1999 till 2004. For the determination of the π^0 reconstruction efficiency in the *BABAR* detector the B meson decay $B^0 \to D^{*-}\pi^+$ with $D^{*-} \to D^-\pi^0$ is selected. Reconstructing these decays without requiring the π^0 for the reconstruction as $B^0 \to D^-\pi^+$, they generate a characteristic bump in the spectrum of the variable $\Delta E = E^*_B - E^*_{beam}$, defined in the e^+e^- center-of-momentum frame, at negative values. The “*” denotes that the variables are also defined in the e^+e^- center-of-momentum frame. Their total number is extracted from a binned χ^2 fit to the measured ΔE distribution, validated on simulated events. If the slow π^0 is required for the reconstruction of the decay $B^0 \to D^{*-}\pi^+$, the measured ΔE spectrum shows a peak around zero. The number of these reconstructed signal events can be extracted again from a χ^2 fit. The π^0 efficiency of the *BABAR* detector is determined using the ratio between the events where the π^0 is required for the reconstruction of the B meson decay to the number of events where the π^0 is not required for the reconstruction. This analysis measures a relative ratio of the π^0 efficiency of the *BABAR* detector between data and simulated events of $\frac{\varepsilon_{Data}}{\varepsilon_{MC}} = (90.0 \pm 6.6_{stat} \pm 0.4_{sys})\%$. The result is compatible with previous studies within the errors.

Contents

List of Figures

List of Tables

Chapter 1

Introduction

> *"A theory is a good theory if it satisfies two requirements: it must accurately describe a large class of observations on the basis of a model that contains only a few arbitrary elements, and it must make definite predictions about the results of future observations."*
>
> Stephen Hawking [1]

The *Standard Model* (SM) of particle physics is the current theoretical description of the elementary particles and of the three of four fundamental interactions between them, mediated by gauge bosons[1]. The elementary particle can be divided into three sorts: leptons, quarks and gauge bosons. The *Standard Model* describes the weak and the strong interaction of quarks and leptons by gauge theories, namely the unified electroweak theory and the *Quantum Chromodynamics* (QCD). The weak interaction distinguishes between weak and mass eigenstates and allows flavor changing transitions of quarks into each other. The transition from mass eigenstates into weak eigenstates is mediated by the Cabibbo-Kobayashi-Maskawa (CKM) matrix [2, 3]. The matrix is characterized by four independent parameters, three angles and one phase. If this phase is different from zero, it is responsible for *CP* violation[2] in the *Standard Model*. The study of *CP* violation is of crucial importance for the understanding of the matter versus antimatter discrepancy of the universe in which we live.

The presented analysis is performed within the scope of the *BABAR* experiment. The purpose of the *BABAR* experiment is to measure parameters of the *Standard Model* of particle physics very accurately and to test experimentally predictions of that model. In particular the experiment focuses on the measurement of *CP* violation in B meson decays. In *BABAR* the B mesons are produced in the decay of the $\Upsilon(4S)$ resonance, which is an excited and bound state of $b\overline{b}$ quarks. B mesons are short-lived particles and are consequently not detected directly by the *BABAR* detector, but by

[1] Bosons refer to particle states with integer spin.

[2] *CP* violation means that particles and its corresponding anti-particles behave asymmetric.

the measurement of its decay products. Thus, the detector observes only the most stable end products - the final state particles. These are electrons, muons, photons, pions, charged kaons or protons. The original B decay is reconstructed based on the measurement of these particles.
Therefore, it is important to understand the detector very well and to know how efficient the single particles are reconstructed in order to allow a precise measurement. In particular the reconstruction efficiency of exclusive B decays is very sensitive to the π^0 reconstruction efficiency of the *BABAR* detector.
The reconstruction of B mesons is also studied in detector simulations with generated particles. The efficiency ratio between real data and simulations can be used to correct the efficiency on simulated data.

Previous measurements determine the π^0 reconstruction efficiency in the *BABAR* detector as a function of the π^0 meson momentum by using τ events or D^0 decays. They are not able to cover the range of very low π^0 momenta below about 300 MeV. Since many studies in *BABAR* depend on B decays, involving low energy π^0 mesons, it is necessary to include also regions of low momenta and energies.

The aim of the presented analysis is to determine the π^0 reconstruction efficiency of low energy π^0 mesons in the *BABAR* detector in a dedicated B meson decay environment. The study uses the decay $B^0 \to D^{*-}\pi^+$ and is performed on data and on simulated events separately. In addition the ratio of the efficiency between data and simulations is calculated.

It is started with a short description of the *BABAR* detector in chapter 2. Chapter 3 gives an introduction to the π^0 meson reconstruction in *BABAR* and presents briefly the previous validation methods to determine the π^0 efficiency of the *BABAR* detector. The chapter ends with a detailed explanation of the new strategy to measure the π^0 efficiency of the *BABAR* detector, used in this analysis. The following chapter 4 summarizes the used data samples and explains the event selection. The fit strategy to extract the the number of the decays $B^0 \to D^{*-}\pi^+$ is described in chapter 5. Chapter 6 presents the results of our analysis and discusses the statistical and systematic uncertainties. Finally, we give an overview about possible improvements of this study in chapter 7 and a summary of all results in chapter 8.

Chapter 2

The *BABAR* Experiment

The *BABAR* experiment is located at the Stanford Linear Accelerator Center (SLAC), in California. The research facility includes the Linear Accelerator (LINAC), the PEP-II storage rings and the *BABAR* detector.
The primary physics goal of the experiment is the study of *CP* violating asymmetries in the decay of neutral B mesons. Additionally, measurements of rare B decays, *CKM* matrix elements and further experimental test of predictions of the *Standard Model* of particle physics are part of the research agenda.
About 600 physicists and engineers from 80 institutes in 11 different countries run the experiment and are joined together in a worldwide collaboration.
The following brief introduction in the *BABAR* experiment is based on Refs. [4, 5], which provide more information.

2.1 The B Meson Factory PEP-II

The electrons and positrons, which are accelerated inside the Linear Accelerator, are injected in the PEP-II storage rings and are collided in the interaction point inside the *BABAR* detector.

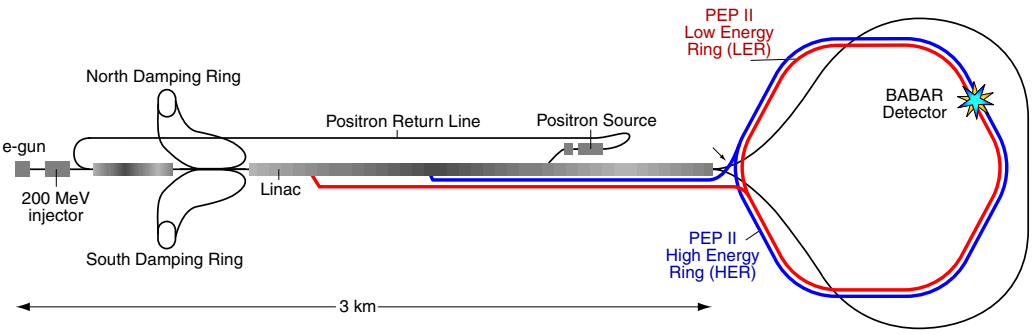

Figure 2.1: The Linear Accelerator (LINAC) and the PEP-II storage rings.

$e^+e^- \rightarrow$	cross section
$b\overline{b}$	1.10 nb
$c\overline{c}$	1.30 nb
$s\overline{s}$	0.35 nb
$u\overline{u}$	1.39 nb
$d\overline{d}$	0.35 nb
$\tau^+\tau^-$	0.94 nb
$\mu^+\mu^-$	1.16 nb
e^+e^-	≈ 40 nb

Table 2.1: The effective cross section at the $\Upsilon(4S)$ resonance ($\sqrt{s} = 10.58\,\text{GeV}$). Except the $b\overline{b}$ cross section, which is taken from [7], the reported cross sections from [4] are quoted.

The electron beam is stored in the high energy ring with an energy of about 9 GeV, whereas the positrons in the low energy ring have an energy of about 3.1 GeV. The collision of the electron and the positron beam results in a center-of-momentum energy of $\sqrt{s} = 10.58\,\text{GeV}$ which is equal to the rest energy of the $\Upsilon(4S)$ resonance. The generated resonance decays nearly completely in $B\overline{B}$ pairs ($\mathcal{B}(\Upsilon(4S) \rightarrow B\overline{B}) > 96\%$ [6]). Beside the $\Upsilon(4S)$ resonance, other quark-antiquark and lepton-antilepton pairs are generated. A summary of the various cross sections in e^+e^- annihilation processes at a center-of-momentum energy of $\sqrt{s} = 10.58\,\text{GeV}$ is quoted in Tab. 2.1.

Due to the different beam energies, the $\Upsilon(4S)$ resonance is generated with a Lorentz boost of $\beta\gamma = 0.56$ with respect to the laboratory frame. Thus, it allows to measure the distance between the decay vertices of both B mesons and thereby, to study the time dependence of these decays.

Since the beginning of data taking in 1999, PEP-II has surpassed its design luminosity of $\mathcal{L} = 3 \cdot 10^{33}\,\text{cm}^{-2}\text{s}^{-1}$ significantly. So far, a peak luminosity of $\mathcal{L} = 12.07 \cdot 10^{33}\,\text{cm}^{-2}\text{s}^{-1}$ was achieved on August 16 ,2006.

From November 1999 till August 2006, PEP-II delivered an integrated luminosity of $\mathcal{L}_{int} = 406.28\,\text{fb}^{-1}$ from which the *BABAR* detector recorded an integrated luminosity of $\mathcal{L}_{int} = 390.85\,\text{fb}^{-1}$. A performance plot is shown in Fig. 2.2.

2.2 The *BABAR* Detector

The *BABAR* detector consists of 5 major detector subsystems. Fig. 2.3 shows a schematic view of the detector. All components are positioned symmetrically around the beam pipe, starting with the Silicon Vertex Tracker followed by the Drift Chamber, the Cherenkov Detector and the Electromagnetic Calorimeter. The complete configuration is surrounded by a superconducting coil, generating a magnetic field of 1.5T, and by the Instrumented Flux Return.

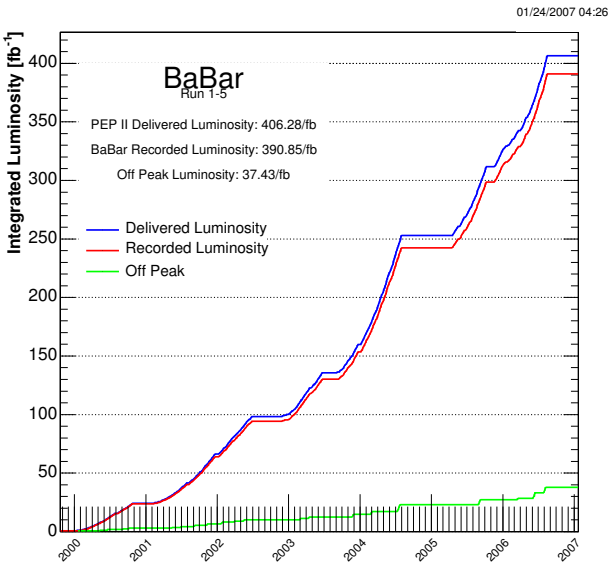

Figure 2.2: Integrated luminosity delivered by PEP-II and recorded by the *BABAR* detector. The presented analysis is based on the dataset, recorded from November 1999 to July 2004.

2.2.1 The Coordinate System

The origin of the *BABAR* coordinate system is defined as the nominal interaction point. The z axis points in the direction of flight of the electrons and is parallel to the magnetic field. The y axis points vertically upwards while the x axis is directed horizontally such that a right handed system is obtained.

2.2.2 The Silicon Vertex Tracker (SVT)

The main purpose of the Silicon Vertex Tracker is to measure charged particle trajectories and decay vertices very close to the interaction point. As innermost subdetector it is the only detector component to provide the tracking of charged particles with transverse momenta less than 120 MeV/c, decaying before they reach the Drift Chamber. Together with the Drift Chamber, the SVT allows a precise measurement of the momenta and the angles of the detected charged particles with higher transverse momenta. In addition the measurement of the distance between the decay positions of the two B mesons is possible.

The SVT consists of 5 concentric cylindrical layers of double-sided silicon microstrip detectors with radii between 32 mm and 144 mm. A cross-sectional view of the SVT is shown in Fig. 2.4. The inner three layers provide a very precise vertex reconstruction with a spatial resolution of 10 - 15 μm. The two outer layers reach a spatial resolution of 30 - 40 μm.

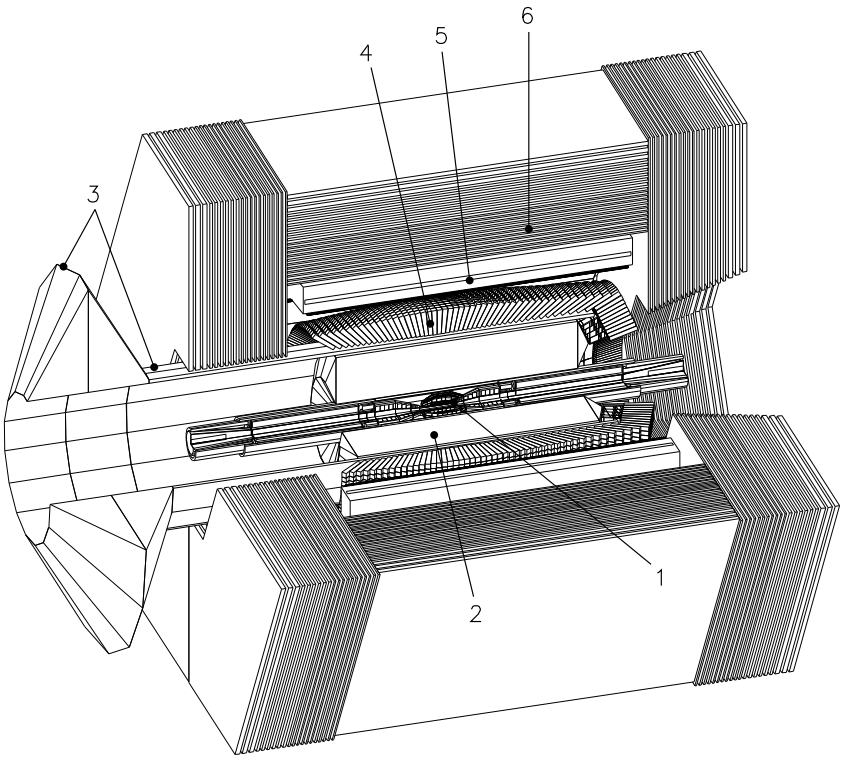

Figure 2.3: The *BABAR* detector. The major subsystems of the detector are: 1) The Silicon Vertex Tracker 2) The Drift Chamber 3) The Detector of Internally Reflected Cherenkov light 4) The Electromagnetic Calorimeter 5) The superconducting coil 6) The Instrumented Flux Return

2.2.3 The Drift Chamber (DCH)

As main tracking device of the *BABAR* detector the Drift Chamber provides the measurement of the momenta of charged particles with $p_T > 100\,\mathrm{MeV}/c$. Additionally its important task is to provide particle identification information for low momentum tracks by measuring the ionization loss dE/dx.
The DCH is almost 280 cm long with an inner radius of 23.6 cm and an outer radius of 80.9 cm. It consists of 40 concentric, cylindrical layers of small hexagonal cells. The drift cells are formed by sense wires of gold plated tungsten-rhenium and gold plated aluminum field wires. The field wires are at ground potential while the sense wires operate with a high voltage of 1960 V. To minimize multiple scattering in the DCH, a 80:20 mixture of Helium:isobutane gas is chosen, which provides a good spatial and dE/dx resolution. A side view of the DCH is shown in Fig. 2.5.

2.2.4 The Cherenkov Detector (DIRC)

The primary task of the Detector for Internally Reflected Cherenkov light is to provide pion and kaon separation up to high momenta of about 4 GeV/c. It is also

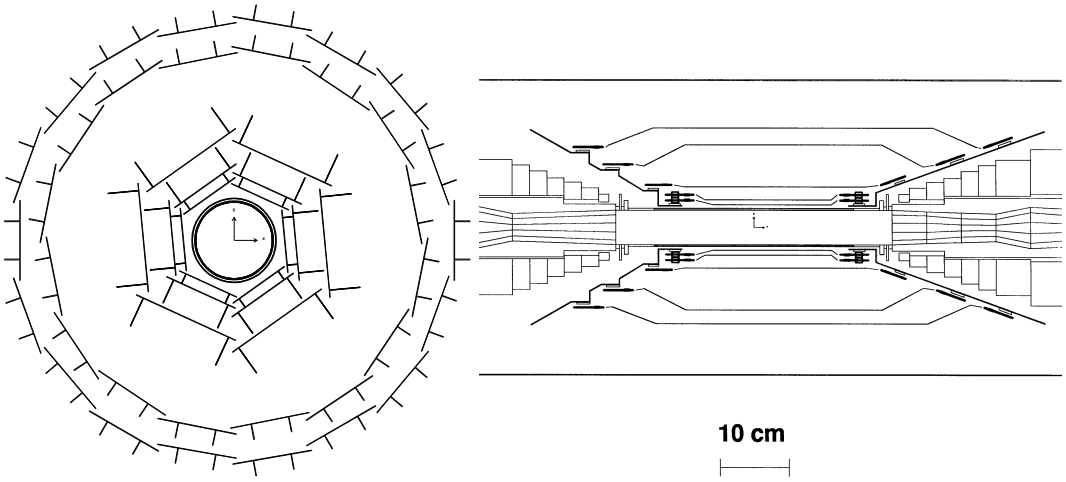

Figure 2.4: Cross-sectional view of the Silicon Vertex Tracker shown in a plane orthogonal to the beam axis (left) and longitudinal to the beam axis (right).

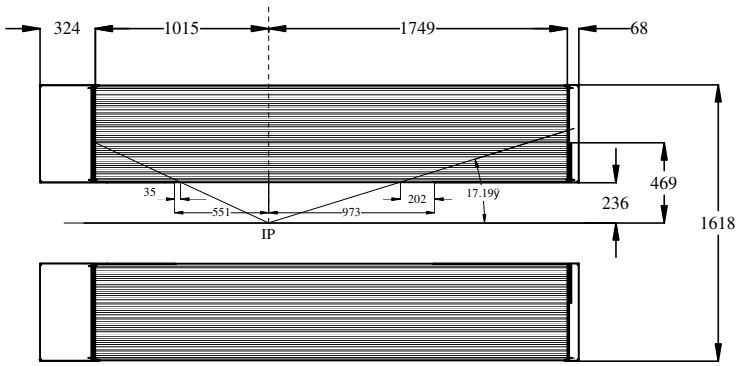

Figure 2.5: Schematic side view of the Drift Chamber. The information about the dimensions are in mm.

used for particle identification of other charged particles (e.g. μ, e^-). The DIRC consists of 144 bars of fused silica arranged in a 12-sided polygonal barrel. The components of the DIRC are schematically illustrated in Fig 2.6.

If a particle passes the DIRC with a velocity higher than the velocity of light in fused silica, Cherenkov light is emitted due to the polarization of the molecules in the material. Afterwards, the Cherenkov photons are transfered by internal reflection, which preserves the angle, to a water filled standoff box at the backward end. The light is observed by an array of around 11000 photo multiplier tubes (PMT) at the outside of the tank.

The Cherenkov angle Θ_C is the angle between the particle direction and the direction of the emitted photons. It depends on the velocity v of the particle and the refraction index n of the material ($n_{silica} = 1.473$). With $\beta = v/c$ and the velocity of light c

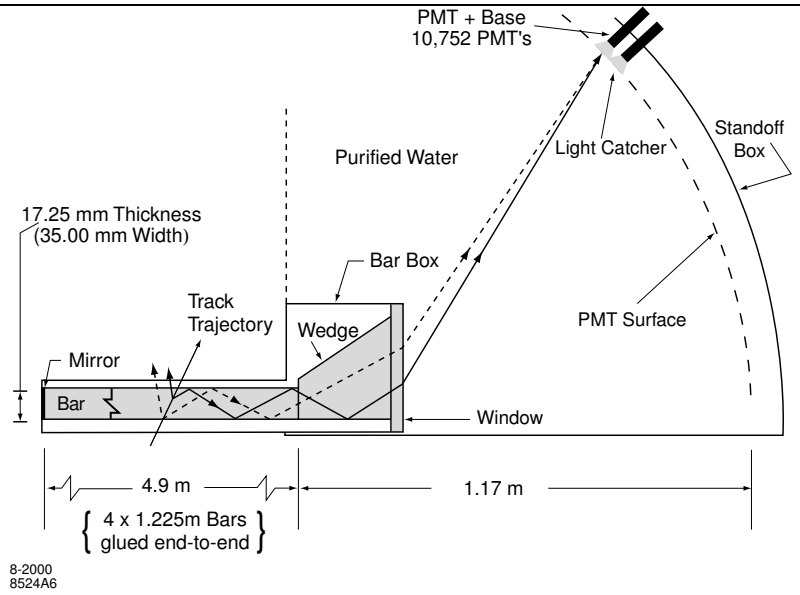

Figure 2.6: Schematics of the Cherenkov Detector

the relation for the Cherenkov angle Θ_C is given by

$$\cos\Theta_C = \frac{1}{\beta n}$$

The Cherenkov angle is reconstructed through the coordinates of the hit PMT and the detection time.

2.2.5 The Electromagnetic Calorimeter (EMC)

The main purpose of the Electromagnetic Calorimeter is to determine the position and energy of photons, electrons and long-living neutral hadrons(K_L). This subdetector is crucially important to reconstruct π^0 mesons which decay into two photons ($\pi^0 \to \gamma\gamma$).
The EMC is composed of 6580 thallium-doped cesium iodide (CsI(Tl)) crystals, arranged in a cylindrical barrel and a conical forward endcap, shown in Fig. 2.7. The barrel contains 48 rings with 120 crystals each, whereas the endcap holds 8 rings with a total of 820 crystals. The complete EMC covers the full azimuthal range and the barrel crystals cover a solid angle corresponding to

$$\begin{aligned} -0.775 \leq \cos\theta_{Lab} \leq 0.962 \qquad & in\ the\ laboratory\ frame \\ -0.916 \leq \cos\theta_{CMS} \leq 0.895 \qquad & in\ the\ center-of-momentum\ frame \end{aligned}$$

To allow the best covarage of the energy deposition of electromagnetic showers, the length of the CsI crystals varies as a function of the crystal position between $16.1X_0$ and $17.5X_0$. The radiation length X_0 of CsI is $X_0(CsI) = 1.85\,\text{cm}$.

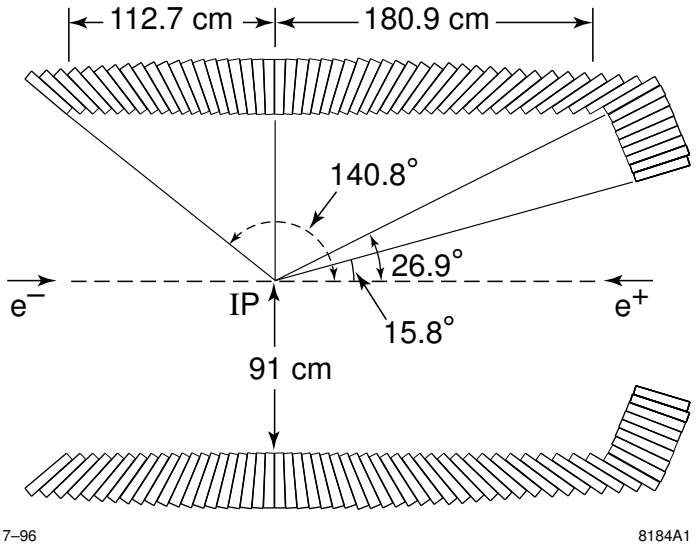

Figure 2.7: Cross-sectional view of the Electromagnetic Calorimeter layout.

The absorbed energy of the shower particles is transfered into atomic excitations. The reemitted scintillation light is detected by two silicon photo diodes at the backward end of each crystal, which is coupled to two low noise and charge sensitive preamplifiers.

Besides, a particle identification is possible due to different shower shapes of the particles.

The crystals have to be calibrated frequently due to the fact that the light yields of the individual crystals vary significantly and change with time under the impact of beam generated radiation. Therefore, it is calibrated at different energies, corresponding to different average shower penetration, to track the effects of radiation damage.

A radioactive photon source (^{16}N) with an energy of 6.13 MeV is used for calibration at low energies, while at high energies ($3 - 9\,\mathrm{GeV}$) electrons from radiative Bhabha events are used.

The EMC measures electromagnetic showers in the range from 20 MeV to 9 GeV with an energy resolution

$$\frac{\sigma_E}{E} = \frac{(2.32 \pm 0.30)\%}{\sqrt[4]{(E/\,\mathrm{GeV})}} \oplus (1.85 \pm 0.12)\%$$

and an angular resolution of

$$\sigma_\phi = \sigma_\Theta = \left(\frac{3.87 \pm 0.07}{\sqrt{(E/\,\mathrm{GeV})}} + (0.00 \pm 0.04) \right) \text{ mrad.}$$

2.2.6 The Instrumented Flux Return (IFR)

The Instrumented Flux Return and the solenoid are the outermost subdetectors. Located between the EMC and the IFR the superconducting solenoid coil provides a magnetic field of 1.5 T and operates at a current of $I = 4.6A$. The magnetic field is crucial to determine the charge and the momentum of the particle from the direction and curvature of the track.
The magnetic flux of the solenoid is returned in an iron yoke which is composed of steel plates with an increasing thickness from 2 to 10 cm from the inside outward. At the beginning of the experiment the IFR consisted of resistive plate chambers (RPC) to identify muons and detect long-lived neutral hadrons. Due to rapid aging and efficiency loss of the original RPCs in the forward endcap and barrel, it was necessary to replace them. The RPC sextants were replaced by Limited Streamer Tubes (LST) in the period between 2004 and summer 2006. Each of the LST sextants contains 12 layers of LSTs and 6 layers of brass absorber.
In addition the IFR serves as the basis for μ/π discrimination since muons are able to penetrate more layers of iron or steel than pions.

Chapter 3

π^0 Efficiency

In this chapter we start with a general introduction in the detection of photons and the reconstruction of π^0 meson decays with the *BABAR* detector. Afterwards, we present briefly the previous methods to measure the reconstruction efficiency of π^0 mesons with the *BABAR* detector. In the end, our new method and analysis strategy to determine the π^0 efficiency of the *BABAR* detector is explained in details.

3.1 π^0 Reconstruction with the *BABAR* Detector

In the following chapter we elucidate the reconstruction process of π^0 mesons with the *BABAR* detector. This information is necessary to understand the event selection criteria used in the new analysis method.
In *BABAR*, the detection of photons from π^0 meson decays ($\pi^0 \to \gamma\gamma$) is provided by the Electromagnetic Calorimeter by measuring their positions, energies and shower shapes. Each absorbed particle in the EMC generates showers of new particles, whereas the energy and the momentum of the original particle is distributed among the shower particles.

The reconstruction of π^0 mesons begins with the energy deposition of the electromagnetic shower, which spreads over many adjacent crystals in the EMC and forms clusters of energy deposits.

cluster: A cluster is defined as a set of crystals, all with an energy above 0.5 MeV and with the sum of their energies above 20 MeV.

In addition a refined definition of energy deposits, denoted as bumps, is introduced to take care of overlapping energy deposits from particles with small angular separation.

bump: Bumps consist of one and only one local maximum within the cluster, caused by a single particle interaction. Thus, clusters contain always one or more bumps.

The reconstruction procedure of the π^0 meson, which decays into two photons ($\pi^0 \to \gamma\gamma$) is subdivided in two categories according to the π^0 energies.
Below π^0 meson energies of about 1 GeV the angle between the two photons is sufficient to produce two well separated clusters. Thus, the π^0 is reconstructed using the four-vectors of the two photons.
For π^0 energies above 1.5 GeV, the separation of the clusters becomes increasingly challenging or at highest energies (e.g. $B \to \pi^0\pi^0$) even impossible. The problem in such cases of high energy photons and π^0 mesons is solved by applying algorithms which use the distribution of energy within the cluster.

In general electromagnetically and hadronically interacting particles are distinguished in the EMC by their lateral distribution of energy within the cluster. Electromagnetically interacting particles are characterized by a cylindrical and symmetrical shape, in contrast to hadronically interacting particles which produce hadronic showers with irregular and less predictable energy deposits.
To discriminate between electromagnetic and hadronic showers, the lateral moment LAT is used. It describes the lateral energy distribution of showers.

LAT: is defined [4] by using the variables N, being the number of crystals associated with the shower, and E_i as the energy deposition in the ith crystal. The numbering of the energies E_i follows the scheme $E_1 > E_2 > \ldots E_N$.

$$LAT = \frac{\sum_{i=3}^{N} E_i r_i^2}{\sum_{i=3}^{N} E_i r_i^2 + E_1 r_0^2 + E_2 r_0^2}$$

Coordinates are expressed in polar notation (r_i, ϕ_i) in the plane perpendicular to the line pointing from the interaction point to the shower center. The average distance between two crystals, denoted as r_0, is approx. 5 cm.

A small value of the variable LAT corresponds to electromagnetic showers which deposit their energy in two or three crystals.

The presented analysis includes π^0 meson decays with low energies and below π^0 momenta of about 300 MeV,where the corresponding photons of the π^0 decay produce well separated clusters in the EMC and are characterized by small values of the variable LAT. We discuss the π^0 meson selection criteria in details in chapter 4.3.

3.2 Previous Measurements of the π^0 Efficiency

This section explains the basic ideas of the previous measurements in order to understand the difference to the new approach. The first analysis selects τ events to determine the relative π^0 efficiency of the *BABAR* detector between data and simulated events. The second method measures the π^0 efficiency of the *BABAR* detector by using decays $D^0 \to K^{\mp}\pi^{\pm}\pi^0$.

3.2.1 Measurement of the π^0 Efficiency using τ Decays

The τ analysis [8] determines the relative π^0 efficiency of the *BABAR* detector between data and simulated events by using τ decays which are generated in *BABAR* in the process $e^+e^- \to \tau^+\tau^-$.

A detailed description what simulated events are and how they are produced in *BABAR* is given in section 4.2. At this point it is only important to know that simulated events are computer generated particle decays.

The selection criteria in the τ analysis are defined such that one of the τ leptons decays in the channel $\tau^+ \to e^+\nu\bar{\nu}$, whereas the other one decays in $\tau^\pm \to h^\pm\nu$ with $h^\pm = \{\pi^\pm, \rho^\pm\}$.
The basic idea of this study is to measure the yields N in the data and the simulation for the decay $\tau \to \pi^\pm\nu$ and $\tau \to \rho^\pm\nu$ with $\rho^\pm \to \pi^\pm\pi^0$ in order to calculate the ratios of the yields

$$\frac{N_{Data}(\tau \to \pi^\pm\nu)}{N_{Sim}(\tau \to \pi^\pm\nu)}, \frac{N_{Data}(\tau \to \rho^\pm\nu)}{N_{Sim}(\tau \to \rho^\pm\nu)}$$

This approach uses the fact that in good approximation the yield $N(\tau \to \pi^\pm\nu)$ is just proportional to the $\pi^\pm$ efficiency, while the yield $N(\tau \to \rho^\pm\nu)$ is proportional to the reconstruction efficiency of the $\pi^\pm$ and the π^0 meson. Thus, only the relative π^0 efficiency is left in the double ratio R.

$$R = \frac{\frac{N_{Data}(\tau\to\rho^\pm\nu)}{N_{Sim}(\tau\to\rho^\pm\nu)}}{\frac{N_{Data}(\tau\to\pi^\pm\nu)}{N_{Sim}(\tau\to\pi^\pm\nu)}}$$

The double ratio R corresponds the ratio of the π^0 efficiency of the *BABAR* detector between the data and the simulation.

3.2.2 Measurement of the π^0 Efficiency using D^0 Decays

This study, described in [9], uses D^0 meson decays to determine the π^0 efficiency ratio R between data and the simulation with the *BABAR* detector. The events are selected such that the D^0 meson is reconstructed either in the channel $D^0 \to K^\mp\pi^\pm$ or in the channel $D^0 \to K^\mp\pi^\pm\pi^0$.
By measuring the signal yields $N(D^0 \to K^\mp\pi^\pm)$ and $N(D^0 \to K^\mp\pi^\pm\pi^0)$ the relative π^0 efficiency is determined by the double ratio R.

$$R = \frac{\frac{N_{Data}(D^0\to K^\mp\pi^\pm\pi^0)}{N_{Data}(D^0\to K^\mp\pi^\pm)}}{\frac{N_{Sim}(D^0\to K^\mp\pi^\pm\pi^0)}{N_{Sim}(D^0\to K^\mp\pi^\pm)}} = \frac{\varepsilon_{Data}}{\varepsilon_{Sim}}$$

In good approximation the $\pi^\pm$ and kaon efficiencies cancel, leaving the relative π^0 efficiency between the data and the simulation.

3.3 New Validation Method of the π^0 Efficiency using B Meson Decays

This section describes the new strategy, which is applied in the presented study, to determine the reconstruction efficiency of low energy π^0 mesons with the *BABAR* detector. Referring to the previous validation methods this is the first study which is performed in a dedicated B decay environment and with low energy π^0 mesons.

To explain the details of the strategy, it is necessary to introduce two kinematic variables defined in the e^+e^- center-of-momentum frame. The first variable ΔE is defined as

$$\Delta E = E_B^* - E_{beam}^* \qquad with \qquad E_{beam}^* = \sqrt{s}/2, \tag{3.1}$$

where E_B^* is the reconstructed energy of the B meson and $\sqrt{s}$ the total energy of the e^+e^- system, both in the center-of-momentum frame.
If a B meson decay is reconstructed correctly, the calculated value of ΔE results in $\Delta E \approx 0$.
The second variable is the energy-substituted mass m_{ES}, which is expressed as

$$m_{\mathrm{ES}} = \sqrt{E_{beam}^{*2} - \vec{p}_B^{*2}}, \tag{3.2}$$

where $\vec{p}_B^*$ is the momentum of the B meson in the center-of-momentum frame, derived from the momenta of its decay products.
Correctly reconstructed B meson decays are characterized by a m_{ES} value around the nominal B mass.

The basic idea of the new analysis strategy is to use the decay $B \to D^*\pi$ with $D^* \to D\pi^0$. The selected decay $B \to D^*\pi$ is appropriate to determine the reconstruction efficiency of low energy π^0 mesons with the *BABAR* detector because the π^0 mesons from the decay $D^* \to D\pi^0$ are characterized by their low energies, due to the kinematics.
On the one hand we reconstruct this decay $B \to D^*\pi$ without requiring the π^0 meson for the reconstruction as $B \to D\pi$. These events generate a peaking structure at negative ΔE values in the ΔE spectrum of the reconstructed decay $B \to D\pi$ because of the missing π^0 energy.
On the other hand the slow π^0 is required for the reconstruction of the decay $B \to D^*\pi$. These decays peak in the ΔE spectrum of the reconstructed decay $B \to D^*\pi$ at $\Delta E = 0$. In both cases we fit the ΔE spectrum in order to extract the number of events $B \to D^*\pi$ which are reconstructed as $B \to D\pi$ or as $B \to D^*\pi$. The π^0 efficiency of the *BABAR* detector is determined using the ratio between the events where the π^0 is required for the reconstruction of the B meson decay to the number of events where the π^0 is not required for the reconstruction.

We declare in our analysis two variables, denoted as $N_{D\pi}$ and $N_{D\pi}^{\pi^0}$, to distinguish the events $B \to D^*\pi$ which are reconstructed as $B \to D\pi$ from events which are correctly reconstructed as $B \to D^*\pi$.

$N_{D\pi}$: The variable $N_{D\pi}$ refers to the number of decays $B \to D^*\pi$ which are reconstructed as $B \to D\pi$ where the π^0 is not required for the reconstruction. They generate a bump in the ΔE spectrum of the reconstructed decay $B \to D\pi$ at negative ΔE values.

$N_{D\pi}^{\pi^0}$: The number of decays $B \to D^*\pi$ which are reconstructed correctly as $B \to D^*\pi$ and where the π^0 is required for the reconstruction is denoted as $N_{D\pi}^{\pi^0}$. These events peak in the ΔE distribution of the reconstructed decay $B \to D^*\pi$ at $\Delta E = 0$.

We extract the yields $N_{D\pi}$ and $N_{D\pi}^{\pi^0}$ from a fit to the ΔE spectrum in order to determine the π^0 reconstruction efficiency as follows

$$\varepsilon(\pi^0) = \frac{N_{D\pi}^{\pi^0}}{N_{D\pi}}. \tag{3.3}$$

The $\pi^\pm$ and kaon efficiencies cancel in good approximation in equation 3.3. By measuring the efficiencies on data and on simulated events we also determine the π^0 efficiency ratio R between data and the simulation.

$$R = \frac{\left(\frac{N_{D\pi}^{\pi^0}}{N_{D\pi}}\right)_{Data}}{\left(\frac{N_{D\pi}^{\pi^0}}{N_{D\pi}}\right)_{Sim}} = \frac{\varepsilon_{Data}}{\varepsilon_{Sim}}$$

In principle both, neutral and charged B mesons, can be used in our analysis with the following decay channels.

1. $B^0 \to D^{*-}\pi^+$ with $D^{*-} \to D^-\pi^0$ ($D^- \to K^+\pi^-\pi^-$)
2. $B^+ \to D^{*0}\pi^+$ with $D^{*0} \to D^0\pi^0$ ($D^0 \to K^-\pi^+$)

We only use the neutral B mesons in this study. In our π^0 efficiency validation method, the second decay channel $B^+ \to D^{*0}\pi^+$ is not appropriate because of the following crossfeed from other decays.

- $B^+ \to D^{*0}\pi^+$ with $D^{*0} \to D^0\gamma$ ($D^0 \to K^-\pi^+$)
- $B^0 \to D^{*-}\pi^+$ with $D^{*-} \to D^0\pi^-$ ($D^0 \to K^-\pi^+$).

The reconstruction of the decay $B^+ \to D^{*0}\pi^+$ as $B^+ \to D^0\pi^+$ produces signal-like shapes in ΔE for the decays $B^+ \to D^{*0}\pi^+$ ($D^{*0} \to D^0\gamma$) reconstructed with a missing photon and $B^0 \to D^{*-}\pi^+$ ($D^{*-} \to D^0\pi^-$) reconstructed with a missing charged pion, which are hard to separate from signal decays. Thus, the determination of the π^0 reconstruction efficiency would depend on the γ and charged pion efficiency too.

The dominating Feynman-Graph for the used decay channel $B^0 \to D^{*-}\pi^+$ is illustrated simplified in Fig. 3.1 and for the decay $B^0 \to D^-\pi^+$ in Fig. 3.2.

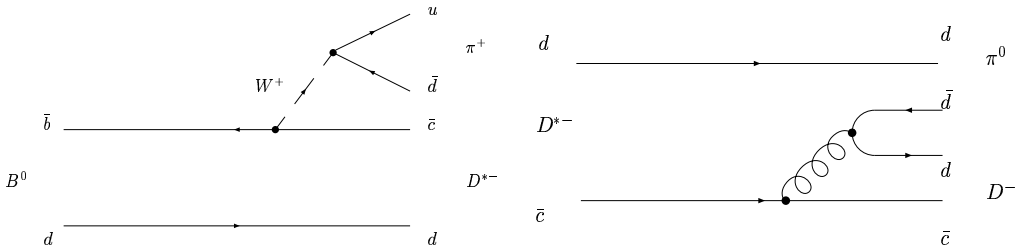

(a) $B^0 \to D^{*-}\pi^+$ (b) $D^{*-} \to D^-\pi^0$

Figure 3.1: Dominating Feynman-Graphs for the decay $B^0 \to D^{*-}\pi^+$ and $D^{*-} \to D^-\pi^0$

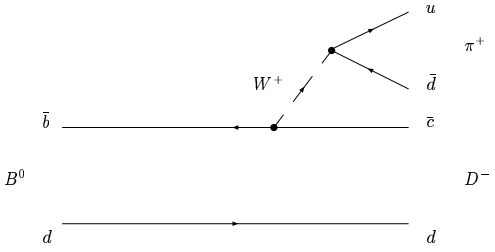

Figure 3.2: Dominating Feynman-Graph for the decay $B^0 \to D^-\pi^+$

Chapter 4

Event Selection

The aim of the presented analysis is the determination of the reconstruction efficiency of low energy π^0 mesons with the *BABAR* detector in a B decay environment, using the decay $B^0 \to D^{*-}\pi^+$ ($D^{*-} \to D^-\pi^0$, $D^- \to K^+\pi^-\pi^-$)[1]. On the one hand we reconstruct this decay without requiring the π^0 meson for the reconstruction as $B^0 \to D^-\pi^+$ ($D^- \to K^+\pi^-\pi^-$). On the other hand we require the slow π^0 for the reconstruction as $B^0 \to D^{*-}\pi^+$ ($D^{*-} \to D^-\pi^0$, $D^- \to K^+\pi^-\pi^-$).
In this chapter the underlying dataset is presented, which is followed by a section where the different reconstruction stages of the particles and the decays are described. The second part of this chapter deals with the refined event selection of the decays under consideration. Finally, methods to suppress background are presented and detailed background studies are performed.

4.1 Skim Production

In this section we introduce briefly the method how the data from the e^+e^- collision is recorded and processed in *BABAR*.

Every high energy e^+e^- collision produces a shower of particles which passes the single layers of the detector. Thus, signals in each detector component are generated, digitalized, and saved as raw data. With this data, tracks and clusters are reconstructed. In the following, particle identification (PID) algorithms are used to assign types of particles to the tracks and clusters. The data produced represents the *AllEvents* dataset. This is the basis for the creation of the *AllEvents* skims where specific tag variables are added. A skim is a subset of the full dataset, which includes particular tag variables (e.g. number of tracks per event). Tag variables are used to describe characteristics of the whole event and to allow a fast selection of events with certain criteria. Thus, all other skims are derived from the *AllEvents* skim.

[1] If nothing else is mentioned, the entire study includes the charge conjugate decays as well.

The *BSemiExcl* skim [10] is an appropriate choice to reconstruct the B meson decays $B^0 \to D^{*-}\pi^+$ and $B^0 \to D^-\pi^+$, but for our analysis method we could not use the *BSemiExcl* skim. The *BSemiExcl* skim selects B meson decays in a narrow ΔE window of $|\Delta E| < 0.2\,\text{GeV}$ which conflicts with our strategy to extract the number of events $N_{D\pi}$ from the ΔE sideband ($-0.3\,\text{GeV} < \Delta E < -0.1\,\text{GeV}$) for the reconstructed decay $B^0 \to D^-\pi^+$.
Thus, we produced our own *modified BSemiExcl* skim, using the algorithms to select fully reconstructed hadronic B decays of the original *BSemiExcl* skim as template. The important modifications compared to the *BSemiExcl* skim are:

- tagging and selection of 14 dedicated B decays instead of more than 100 B decays to reduce the CPU time for the skimming and the size of the final sample
- looser cuts on ΔE: $-0.4\,\text{GeV} < \Delta E < 0.4\,\text{GeV}$ instead of $|\Delta E| < 0.2\,\text{GeV}$

The 14 selected B decays include the two relevant B decays for this analysis and 12 additional B decay modes which are studied by Thorsten Brandt. He was the person who programmed the major part of our new *modified BSemiExcl* skim. A complete list of the skimmed decay modes is summarized in Appendix B.

4.1.1 Skim Software

To analyze and process the data, we use the common *BABAR* software environment. The software is controlled by the application framework `Beta` and consists of different specific software packages [11] which are provided in software releases. For the skim production we use the software release *18.6.3i*. In the following list, all relevant software packages used in addition are quoted. The tag "HEAD" refers to the latest version of the package.

- BRecoilTools HEAD
- CompositionSequences V00-05-03
- CompositionTools V01-06-00
- FilterTools V00-19-02
- PackageList V00-11-01
- SkimMini V00-04-15
- VcbRecoil HEAD
- workdir V00-04-20

The B mesons are already reconstructed in the skim, using the software packages *CompositionSequences* and *CompositionTools*. The new skim is produced with the software package *SkimMini* and is written in dedicated collection files. These collections represent the new skim and are used for the subsequent analysis.

4.2 Monte Carlo and Data Samples

The entire analysis is based on the *BABAR* dataset, recorded from November 1999 to July 2004 with a corresponding total integrated luminosity of $209.48\,\text{fb}^{-1}$. Most

	Run 1	Run 2	Run 3	Run 4	Run 1-4
onpeak data	20.06	58.83	32.07	79.49	190.45
offpeak data	2.32	5.41	2.46	8.84	19.03

Table 4.1: Summary of the integrated onpeak and offpeak luminosities (in fb^{-1}) used in this analysis and subdivided in run periods.

of the data, approx. $190.45\,\mathrm{fb}^{-1}$, has been collected at the $\Upsilon(4S)$ resonance with a center-of-momentum (C.M.) energy of $\sqrt{s} = 10.58\,\mathrm{GeV}$ and is denoted as onpeak data. Using the cross section value $\sigma = 1.101\,\mathrm{nb}$ [4] of the process $e^+e^- \to b\overline{b}$, a luminosity of $190.45\,\mathrm{fb}^{-1}$ corresponds to approximately $210 \cdot 10^6$ $B\overline{B}$ events.
About 10% of the data are taken at a C.M. energy about 40 MeV below the $\Upsilon(4S)$ resonance, where $e^+e^- \to b\overline{b}$ production is kinematically forbidden. This data, labeled as off-resonance data, is important for studying the background from $e^+e^- \to q\overline{q}$ where $q = \{u, d, s, c\}$.
In Tab 4.1 the luminosities for onpeak and offpeak data are summarized.

Simulated events are used to develop and validate the analysis method. In total, two different classes of events are generated:

generic[2] $B\overline{B}$ **events** which consist of decays:
$e^+e^- \to \Upsilon(4S) \to B\overline{B}$ with $B\overline{B} = \{B^0\overline{B}^0, B^+B^-\}$

continuum events which include decays:
$e^+e^- \to q\overline{q}$ with $q\overline{q} = \{u\overline{u}, d\overline{d}, c\overline{c}, s\overline{s}\}$

In *BABAR*, the event generators `EvtGen` [12] and `Jetset` [13] are used for these Monte Carlo (MC) simulations. `EvtGen` is the main generator of B decays for about 50% of all final states. With `Jetset` generic continuum events and the remaining 50% of B decays are simulated by fragmentation.
The *BABAR* detector response is simulated based on the simulation tool `GEANT` [14]. This software takes the detector geometry as well as the particle interactions with the detector material into account. When analyzing the simulated events an additional information about the true decay is available. This *MC Truth* information contains all relevant data of the decay generated by the event generator. The information of the true decay helps to study the reconstructed decays in the detector.
In the presented analysis the true decay is often labeled as generated decay. The simulated events used are produced in the Monte Carlo Simulation Production cycle SP8.

4.2.1 Creation of the Monte Carlo Sample

The Monte Carlo samples used are a mix of simulated generic $B\overline{B}$ and continuum events. This work bases on two different mixes of this kind. The first one which

[2] In generically simulated $B\overline{B}$ events the B mesons can decay in all known decay channels with the associated branching fractions.

is denoted as mixed Monte Carlo sample is used for the comparison with real data and for the fit on simulated data. Our Monte Carlo model for the fit is generated from events of the second statistical independent sample.

mixed Monte Carlo sample This sample consists of simulated generic $B\overline{B}$ and continuum events which are mixed according to the corresponding cross sections. The luminosity of this sample is comparable to the data luminosity.

Monte Carlo Model sample The simulated generic $B\overline{B}$ and continuum events which are not used in the mixed Monte Carlo sample form this sample. In contrast to the mixed Monte Carlo sample the are not mixed according to the cross section.

The number of Monte Carlo events for every Run is quoted in Tab. 4.2.
For the creation of the mixed Monte Carlo sample it is assumed that the $\Upsilon(4S)$ resonance decays equally into B^+B^- and $B^0\overline{B}^0$ pairs. Due to the limited number of continuum events it is necessary to normalize on the number of $e^+e^- \rightarrow q\overline{q}$ with $q\overline{q} = \{u\overline{u}, d\overline{d}, s\overline{s}\}$ events. To determine the number of the other events ev_i which are used to form the mixed sample, we use the equation

$$\frac{ev_i}{ev_{u,d,s}} = \frac{\sigma_i}{\sigma_{u,d,s}} \qquad with\ i = \{c\overline{c}, B^+B^-, B^0\overline{B}^0\}$$

with the cross sections σ_i from Tab.2.1.
From the total number of events we select this calculated fraction ev_i randomly in order to generate the mixed Monte Carlo sample. This procedure is done separately for every run, and afterwards they are merged together.
The applied routine includes the creation of the Monte Carlo Model sample as well because every event which is not selected for the mixed sample is filled in another individual file. Finally, there are two files which contain a disjunct set of all events.

Run 1				
Monte Carlo Type	Total events N_{tot}	σ (nb)	Selected events N_{Mix}	N_{Mix}/N_{tot}
$u\overline{u}, d\overline{d}, s\overline{s}$	42.580.000	2.09	42.580.000	1.0
$c\overline{c}$	26.952.000	1.30	26.485.167	0.98
B^+B^-	33.038.000	0.545	11.103.397	0.33
$B^0\overline{B}^0$	34.034.000	0.545	11.103.397	0.32

Run 2				
Monte Carlo Type	Total events N_{tot}	σ (nb)	Selected events N_{Mix}	N_{Mix}/N_{tot}
$u\overline{u}, d\overline{d}, s\overline{s}$	141.640.000	2.09	141.640.000	1.0
$c\overline{c}$	119.190.000	1.30	88.101.435	0.74
B^+B^-	134.319.800	0.545	36.934.832	0.28
$B^0\overline{B}^0$	155.112.000	0.545	36.934.823	0.24

Run 3				
Monte Carlo Type	Total events N_{tot}	σ (nb)	Selected events N_{Mix}	N_{Mix}/N_{tot}
$u\overline{u}, d\overline{d}, s\overline{s}$	88.494.000	2.09	88.494.000	1.0
$c\overline{c}$	92.222.000	1.30	55.041.114	0.59
B^+B^-	119.124.000	0.545	23.076.186	0.19
$B^0\overline{B}^0$	123.544.000	0.545	23.076.186	0.19

Run 4				
Monte Carlo Type	Total events N_{tot}	σ (nb)	Selected events N_{Mix}	N_{Mix}/N_{tot}
$u\overline{u}, d\overline{d}, s\overline{s}$	159.292.000	2.09	159.292.000	1.0
$c\overline{c}$	122.968.000	1.30	99.081.148	0.81
B^+B^-	155.872.000	0.545	41.537.866	0.27
$B^0\overline{B}^0$	160.356.000	0.545	41.537.866	0.26

Table 4.2: The number of simulated Monte Carlo events N_{tot} for every Run is shown. The column "Selected events" contains the number of events which are used to create the mixed Monte Carlo sample. We normalize on the number of $e^+e^- \to q\overline{q}$ with $q\overline{q} = \{u\overline{u}, d\overline{d}, s\overline{s}\}$ events. The ratio N_{Mix}/N_{tot} gives the fraction of the total events used to form the mixed sample. The cross sections are taken from Tab. 2.1.

4.3 Event Reconstruction

The actual event reconstruction is already done on `Beta` level during the skim production. There, the considered 14 B meson decays are reconstructed and tagged so that they could be easily filtered out. For filtering and for saving the complete event information we use another software release, analysis-31, with the same software packages as for the skim production.
In addition, the following packages [15] listed are used for energy smearing and shifting in order to improve the agreement between simulation and data when reconstructing neutral particles on simulated events.

- EmcCalibToo V01-00-02-01
- EmcSequence V00-06-02-04-01

All relevant event information is saved in `Root` tuples, provided by the software package *VcbRecoil*. For the subsequent study of these tuples, we use the `Root` software environment [16].

4.3.1 Reconstruction and Identification of Charged Tracks

The reconstruction of charged particles in this analysis is based on the lists *ChargedTracks*, consisting of all reconstructed charged tracks in the detector, and the refined list *GoodTracksVeryLoose*. Particles of *GoodTracksVeryLoose* fulfill the additional criteria:

- maximal momentum in the laboratory frame: $p < 10\,\mathrm{GeV}/c$
- distance of closest approach to the beamspot
  - in the x-y plane: $d_{xy} < 1.5\,\mathrm{cm}$
  - in direction of the z axis: $-10\,\mathrm{cm} < \mathrm{d_z} < 10\,\mathrm{cm}$

At the *BABAR* detector charged particles are mainly identified by the silicon vertex tracker (SVT), the drift chamber (DCH) and the cherenkov detector (DIRC). There, the collected informations complement each other. The particle identification (PID) is realized by a software in two steps. At first the response of each detector component is analyzed independently. For every particle hypothesis (e, μ, π, K, p) a likelihood [17] is assigned. In a second step the different subdetector informations are combined and the particle candidates are saved in different PID lists according to the different selection criteria and particle hypothesis.

4.3.2 K and π Meson Reconstruction

In our analysis pions from the *GoodTracksVeryLoose* list and kaons which have passed the *KLHNotPion* likelihood selector are combined to reconstruct D mesons. Likelihood selectors rely on the computed likelihood functions during the reconstruction.
The reconstruction of B mesons is performed with pions and kaons of the neural network based *KNNTight* list, which are grouped in a *piKList* [10] list. The neural network selector uses the combination of different PID variables. Using tracks from *GoodTracksVeryLoose*, the *piKList* is defined as follows:

- all tracks are discarded which overlap with:
  - electrons from the *PidLHElectrons* list
  - muons from *muNNTight*
  - electrons from *gamma conversions* ($\gamma \to e^+e^-$)
  - pions from the decay $\Lambda \to p\pi$
- tracks from the *KNNTight* list are assigned to kaons and all the other particles are treated as pions

4.3.3 π^0 Meson Reconstruction

The π^0 mesons in this analysis are taken from the *pi0DefaultMass* list, which is made of photon candidates passing the following requirements.

- a lateral moment: $0 < LAT < 0.8$
- an invariant $\gamma\gamma$ mass (before the mass constraint) in the range: $115\,\mathrm{MeV}/c^2 < m_{\gamma\gamma} < 150\,\mathrm{MeV}/c^2$
- an energy in the laboratory frame above: $E^{\pi^0}_{lab} > 200\,\mathrm{MeV}$

Both photon four-momenta are combined with simple four-vector addition. To improve the reconstruction of the π^0 momentum, a kinematic fit with a mass constraint $(p_{\gamma_1} + p_{\gamma_2})^2 = m^2_{\pi^0}$ and a primary vertex constraint, which requires the π^0 decay vertex to be the primary event vertex, is performed.

4.3.4 D Meson Reconstruction

We take the D mesons in our study from the composite list *DcToKPiPiLoosePID*, where pions from *GoodTracksVeryLoose* are combined with kaons from *KLHNotPion* by four-vector addition. Further properties of the D mesons from this list are:

- an invariant $K\pi\pi$ mass $|m_{K\pi\pi} - m_{D^-}| < 0.02\,\mathrm{GeV}/c^2$ around the nominal mass of $m_{D^-} = 1.8693\,\mathrm{GeV}/c^2$ [6]
- a momentum in the center-of-momentum system in the range $1.0\,\mathrm{GeV}/c < p < 2.5\,\mathrm{GeV}/c$

4.3.5 Reconstruction of $B^0 \to D^-\pi^+$

To reconstruct the complete $B^0 \to D^-\pi^+$ decay, particles from the *piKList* are combined with D mesons from the composite list *DcToKPiPiLoosePID*. In addition all events have to pass the $R2$ filter. R2 is one of the tag variables which is calculated during the skim production.

$R2$: The variable $R2$ is defined as the ratio of the 2nd and the 0th Fox-Wolfram moment.

$$R2 = \frac{H_2}{H_0}, \tag{4.1}$$

where the Fox-Wolfram moments [18] are given by

$$H_l = \sum_{i,j} \frac{|\vec{p}_i| \cdot |\vec{p}_j|}{E_{vis}^2} P_l(\cos\Theta_{ij}) \tag{4.2}$$

with the particle momenta $\vec{p}_{i,j}$. P_l represents a Legendre polynomial and the opening angle between the particles i and j is Θ_{ij}. E_{vis} stands for the total visible energy in the event.

$R2$ is confined between 0 and 1 with small values of $R2$ corresponding to isotropic events while jet-like events tend to be close to 1. B decays are characterized by an isotropic decay topology.

In this analysis only events with $R2 < 0.5$ are selected.
For the final reconstruction of $B^0 \to D^-\pi^+$ only decays are accepted in the ΔE range $-0.4\,\mathrm{GeV} < \Delta E < 0.4\,\mathrm{GeV}$. If the B^0 mesons are reconstructed correctly they should peak in the ΔE spectrum at $\Delta E = 0$ and in m_{ES} at the nominal B^0 mass $m_{B^0} = 5.2794\,\mathrm{GeV}/c^2$ [6]. Reconstructing the decay $B^0 \to D^{*-}\pi^+$ ($D^{*-} \to D^-\pi^0$) as $B^0 \to D^-\pi^+$ with a missing π^0, these events are expected to peak in the ΔE spectrum of the reconstructed decay $B^0 \to D^-\pi^+$ at negative ΔE values.

4.3.6 Reconstruction of $B^0 \to D^{*-}\pi^+$

The decay $B^0 \to D^{*-}\pi^+$ is not included directly in the skim, but the decay is added if the difference of the invariant masses ΔM between the combination of the particles $(K\pi\pi)\pi^0$ and $(K\pi\pi)$ is less than

$$|m_{(K\pi\pi)\pi^0} - m_{K\pi\pi}| < 0.16\,\mathrm{GeV}/c^2$$

If the requirement is fulfilled, the decay $B^0 \to D^{*-}\pi^+$ ($D^{*-} \to D^-\pi^0$) is reconstructed by combining the D meson candidate from the *DcToKPiPiLoosePID* list, the π^0 from the *pi0DefaultMass* list and the particles from the *piK* list, using four-vector addition. A detailed description of the technical implementation of the decay $B^0 \to D^{*-}\pi^+$ is given in Appendix B.

All events have to pass the $R2 < 0.5$ selection and only decays within the ΔE range $-0.4\,\mathrm{GeV} < \Delta E < 0.4\,\mathrm{GeV}$ are accepted. Again it is expected that correctly reconstructed $B^0 \to D^{*-}\pi^+$ should peak in the ΔE spectrum at $\Delta E = 0$ and in m_{ES} at the nominal B^0 mass $m_{B^0} = 5.2794\,\mathrm{GeV}/c^2$ [6].

4.3.7 Decay Mode Numbers

This section elucidates some technical details concerning the reconstruction of the decays.

A property of the presented analysis is the use of decay mode numbers, where every reconstructed B meson decay is assigned to a certain combination of numbers. The calculation of this number is already done at the `Beta` level and provided by specific classes of the software package *VcbRecoil*. The complete decay tree of the B meson and its daughter particles is examined and the calculated decay mode number for every decay in the event is written directly into the `Root` tuple.

Without further studies, it is not possible to deduce unambiguously the exact decay topology. However, using the list of B (Tab. B.3) and D meson decay modes (Tab. B.2) and applying simple mathematical operations on the decay mode number, some general propositions about the decay can be made.

We explain this procedure briefly on the example of the decay $B^0 \to D^-\pi^+$ with $D^- \to K^+\pi^-\pi^-$, which is assigned to the decay mode number 12101. The information about the decay of the B meson is given by the remainder on dividing 12101 by 100:

$$12101 \; \textit{modulo} \; 100 = 1 \qquad \Rightarrow B \to D^{\pm}\pi$$

The obtained result "1" corresponds in the list of B decay modes (Tab. B.3) to the decay $B \to D^{\pm}\pi$. The decay mode of the D meson for the considered decay $B^0 \to D^-\pi^+$ is calculated as the following quotient

$$12101/100 = 121 \qquad \Rightarrow D^{\pm} \to K\pi\pi$$

where only the integer part is regarded. In the list of the D decay modes (Tab. B.2) the result "121" stands for the decay $D^{\pm} \to K\pi\pi$. Taking both results into account a general proposition about the decay, assigned to the decay mode number 12101, can be made.

$$12101 \equiv B \to D^{\pm}\pi \; \textit{with} \; D^{\pm} \to K\pi\pi$$

A complete list of all decays presented in this analysis and their decay mode number is quoted in Appendix B. To ease the reading, the document uses as often as possible the corresponding decay instead of the decay mode number.

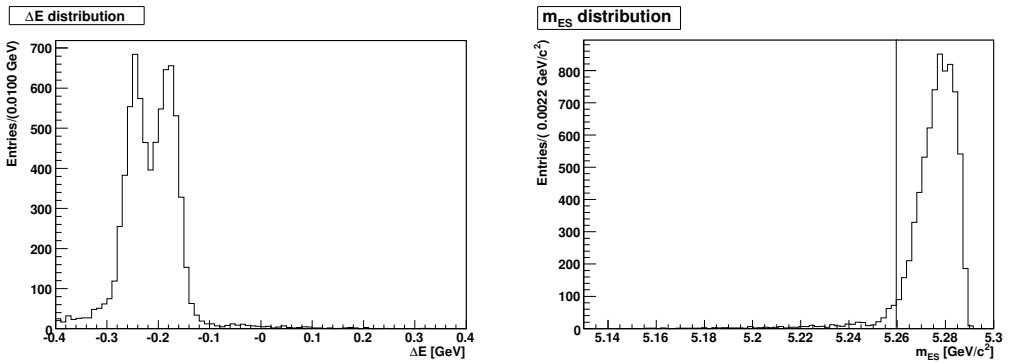

Figure 4.1: ΔE and m_{ES} spectrum for the true signal decay $B^0 \to D^{*-}\pi^+$ which is reconstructed as $B^0 \to D^-\pi^+$.

4.4 Refined Event Selection for the Decay $B^0 \to D^-\pi^+$

In this section the refined selection criteria for the decay $B^0 \to D^-\pi^+$ are presented. First, the expected ΔE and m_{ES} distributions are studied on Monte Carlo simulations and hence criteria to suppress the background are derived. The following paragraphs explain these steps in detail. Finally, a shift in the ΔE spectrum between the data and the Monte Carlo simulation is discussed and the procedure for a correction as well.

4.4.1 ΔE and m_{ES} Distribution

In the ΔE distribution of the reconstructed decay $B^0 \to D^-\pi^+$ we expect a peak at $\Delta E \approx 0$ and a significant peaking structure at negative ΔE values, representing the actual signal events $B^0 \to D^{*-}\pi^+$. If there is a true decay $B^0 \to D^-\pi^+$ which is also reconstructed as $B^0 \to D^-\pi^+$,the calculated ΔE value should be 0. These correctly reconstructed $B^0 \to D^-\pi^+$ decays are denoted as pseudo signal.
We expect that our signal events $B^0 \to D^{*-}\pi^+$ produce a peaking structure in the range $-0.3\,\mathrm{GeV} < \Delta E < -0.1\,\mathrm{GeV}$. Fig. 4.1 shows the ΔE and m_{ES} distribution for the true decays $B^0 \to D^{*-}\pi^+$, which are reconstructed as $B^0 \to D^-\pi^+$ by using the mixed Monte Carlo sample. The origin of the characteristic double peak structure is explained in Appendix A. This structure is very useful for extracting the actual signal when reconstructing the decay $B^0 \to D^-\pi^+$. In Fig. 4.2, the ΔE and m_{ES} spectrum for the reconstructed decay $B^0 \to D^-\pi^+$ as found in the Monte Carlo simulation is shown.
The different Monte Carlo sources are marked with colors but the peaking structure in the range $-0.3\,\mathrm{GeV} < \Delta E < -0.1\,\mathrm{GeV}$ is hardly visible.
To suppress background, a cut on the variable m_{ES} is applied.

$$m_{\mathrm{ES}} > 5.26\,\mathrm{GeV}/c^2,$$

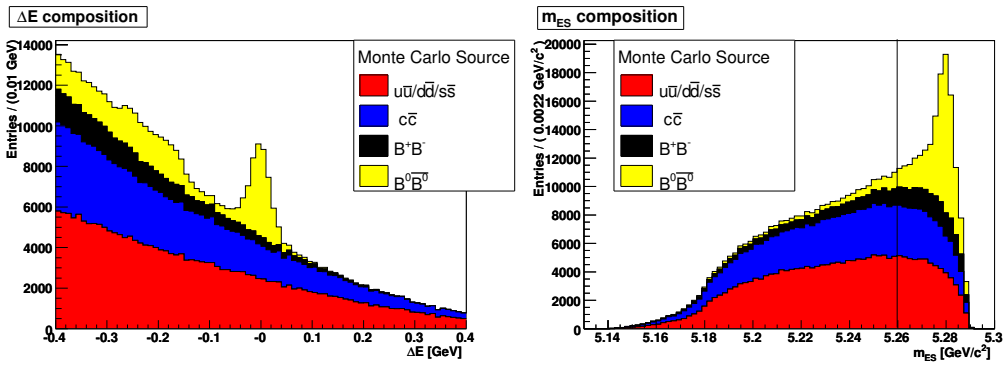

Figure 4.2: ΔE and m_{ES} spectrum for the reconstructed decay $B^0 \to D^-\pi^+$ on the mixed Monte Carlo sample with the background included. The signal is in the range $-0.3\,\mathrm{GeV} < \Delta E < -0.1\,\mathrm{GeV}$. The various Monte Carlo sources are distinguished using different colors.

which reduces a lot of background according to Fig. 4.2 and causes only a small loss of signal, according to Fig. 4.1.

4.4.2 Background Suppression: Neural Network versus Fisher Discriminant

Due to the large number of continuum events denoted as combinatorial background, it is necessary to suppress this background as good as possible. For this purpose, a combination of 8 variables is used to build a Neural Net [19, 20] and to calculate a Fisher discriminant [21]. Both methods are implemented using the software package TMVA [22] version 1.1 which includes several discrimination techniques to separate signal from background.
The Fisher discriminant used describes a linear equation in the hyper-plane, spanned by the 8 input variables, which separates signal from background events. In the training process, the so called Fisher coefficients are determined such that the variance between signal and background events is maximized and events of the same class (signal and background) are confined in a close vicinity. For the later application of the Fisher discriminant the saved Fisher coefficients are used, determined in the training.
A general advantage of artificial neural networks is that non-linear correlations between the input variables are taken into account.
The artificial neural network used is structured in three different layers of neurons. The neurons form the smallest unit of the algorithm and each of them is able to process input and output signals. The input layer consists of the same number of neurons as there are input variables. The output layer contains two neurons to separate a signal class and a background class. Between the input and the output layer an arbitrary number of hidden layers can be added. The connections between the single neurons are weighted differently. During a phase of training the best

value for these weights is determined to obtain the best separation between signal and background. The resulting weight matrix is saved and used later when the Neural Net is applied. The tool TMVA includes three different implementations of Neural Nets.
The following variables are used as input variables for the Neural Net and the Fisher discriminant. All are calculated in the $\Upsilon(4S)$ rest frame.

thrust: The variable thrust allows to describe the decay topology of the event. For the calculation, the thrust axis $\hat{T}$ and the three momenta $\vec{p}_i$ of all particles in the event are used.

$$T = \frac{\sum_{i=1} |\hat{T} \cdot \vec{p}_i|}{\sum_{i=1} |\vec{p}_i|} \qquad with\ T \in [0.5, 1] \tag{4.3}$$

The notation is based on Ref. [23]. The thrust axis $\hat{T}$ represents direction for which the momenta of the particles is maximized. Continuum events are jet-like events with $T \approx 1$. B decays are characterized by isotropic decay topologies corresponding to $T \approx 0.5$.

sphericity: This variable is also used to distinguish between different decay topologies. Determined by the measure of the sum of the squares of the transverse momenta for each particle in the whole event, the sphericity is defined [24] as follows:

$$S = \frac{3}{2}(\lambda_2 + \lambda_3). \tag{4.4}$$

λ_2 and λ_3 represent the largest eigenvalues of the sphericity tensor $S^{\alpha\beta}$.

$$S^{\alpha\beta} = \frac{\sum_{i=1} p_i^\alpha \cdot p_i^\beta}{\sum_{i=1} p_i^2} \tag{4.5}$$

The notation $\alpha, \beta = 1, 2, 3$ corresponds to the x,y,z components for all particles in the event, and p_i stands for the three momenta. The variable sphericity S is limited to the range $S \in [0, 1]$. For jet-like events S tends to 0, whereas isotropic events are characterized by $S \approx 1$.

$R2$: This variable is already defined in section 4.3.5. Small $R2$ values correspond to isotropic events while jet-like events tend to $R2 \approx 1$.

$\cos\Theta_{thrust}$: The variable $\cos\Theta_{thrust}$ is defined as the cosine of the angle between the thrust axis of the B candidate and the thrust axis of all charged and neutral particles in the event not belonging to the B candidate.

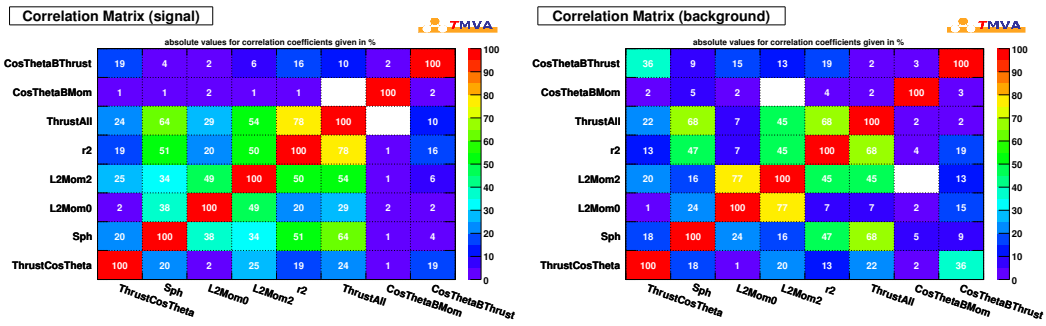

Figure 4.3: Correlation matrices for the various variables which discriminate the signal and the background, obtained for the Neural Net.

L_0, L_2**:** The energy flow moments L_0 and L_2 are defined by the general formula:

$$L_j = \sum_{i=1}^{roe} p_i \cdot |\cos\Theta_i|^j \tag{4.6}$$

p_i is the absolute value of the three momentum of particle i in the rest of the event (roe). The angle Θ_i corresponds to the angle between the thrust axis of the B candidate and the momentum of the ith particle in the rest of the event.

$\cos\Theta_{Bthrust}$**:** This is the cosine of the angle between the thrust axis of the B candidate and the beam axis.

$\cos\Theta_{Bmom}$**:** This is the cosine of the angle between the momentum vector of the B candidate in the $\Upsilon(4S)$ frame and the beam axis.

The variables thrust, sphericity, L_0, L_2 and R2 which are used to describe the decay topology of the event are highly correlated, but nevertheless each of them reflects another aspect of the decay. The correlation matrices for the Neural Net are shown in Fig. 4.3.
The separation power of each variable is shown in Fig. 4.4, and the resulting output of the Fisher and the Neural Net for the signal and background sample is illustrated in Fig 4.5.

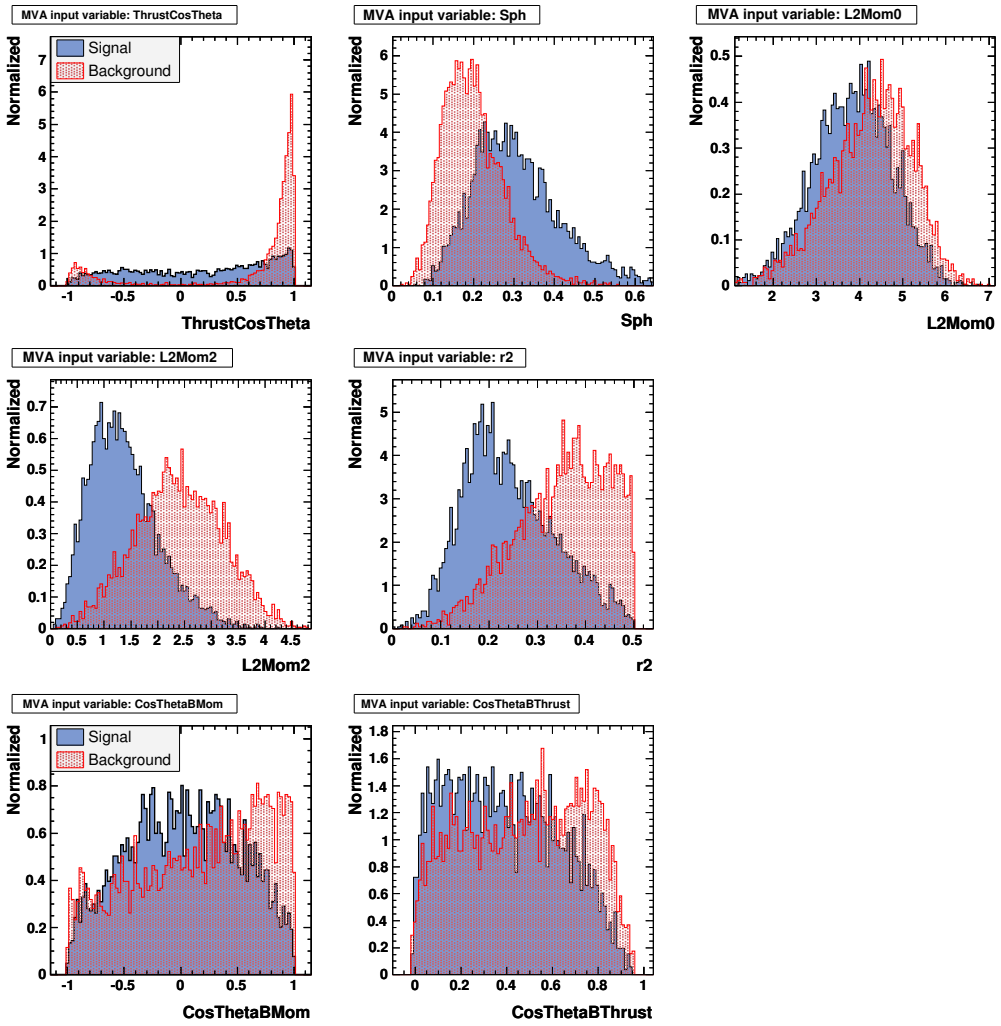

Figure 4.4: 8 discriminating variables are used to train the Neural Net. The output is generated with the TMVA package.

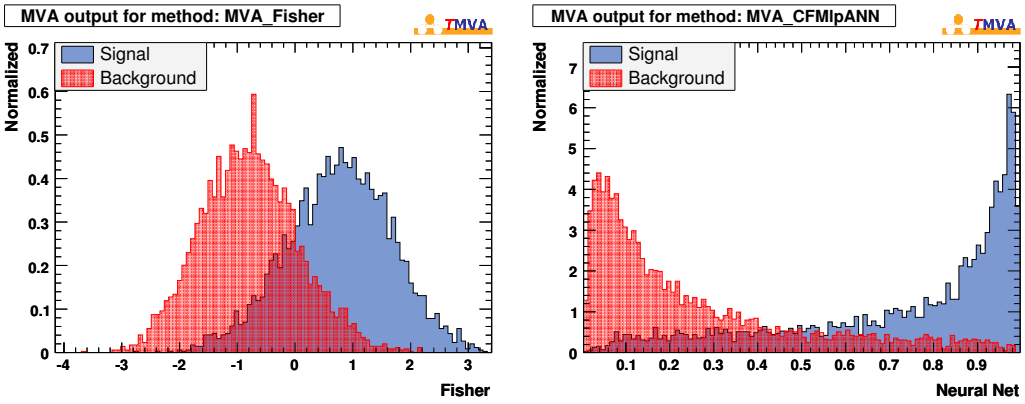

Figure 4.5: Resulting distribution for the Fisher discriminant and the Neural Net for simulated signal events and simulated continuum events.

Applied Cuts for training	
cut	value
ΔE	$-0.31\,\mathrm{GeV} < \Delta E < -0.11\,\mathrm{GeV}$
m_{ES}	$m_{\mathrm{ES}} > 5.26\,\mathrm{GeV}/c^2$
$m_{K\pi\pi}$	$1.8550\,\mathrm{GeV}/c^2 < m_{K\pi\pi} < 1.8825\,\mathrm{GeV}/c^2$
Best B meson candidate selection	

Table 4.3: The cuts applied for training the Neural Net.

Number of	Input events	Events passed cut	Training events	Test events
Signal	76545	9051	4500	4500
Background	402440	10217	4500	4500
Total	478985	19268	9000	9000

Table 4.4: Number of events used for the Neural Net training sample. The total amount of events in the training sample is fixed by the number of signal events passing the cuts.

Neural Net Setup and Training

This analysis uses a Artificial Neural Network [25] with 8 input variables. The configuration of the layers consists of one input layer and two hidden layers where each of them contains 8 neurons and an output layer with two neurons.

The signal class is defined by using tight cuts especially in the ΔE-m_{ES} plane which are quoted in Tab 4.3. A detailed description of these cuts is given in the following sections. For the signal and the background class the decay $B^0 \to D^-\pi^+$ is reconstructed.

As signal, only $B^0\overline{B}^0$ events from the mixed Monte Carlo sample of Run 1-2 are used.

The background class consists of continuum events of the same mixed Monte Carlo sample. Simulated events are used due to the small statistics in offpeak data.

We train the Neural Net against these continuum events in 5000 training cycles. The training process is subdivided into the following steps. After applying all cuts from Tab. 4.3, the number of signal events and background events passing the cuts is determined. Half of these events is used for training and the other one for testing. The decomposition of the training sample is quoted in Tab. 4.4.

To decide whether to use the Fisher discriminant or the Neural Net to suppress the continuum background in our analysis, we compare the ratio of background rejection versus the signal efficiency as shown in Fig. 4.6. Furthermore, we apply both techniques on data and compare the double peak structure at negative ΔE values for the reconstructed decay $B^0 \to D^-\pi^+$. Finally, the Neural Net showed a slightly better performance compared to the Fisher discriminant.

In this analysis the Neural Net is selected to suppress the continuum background.

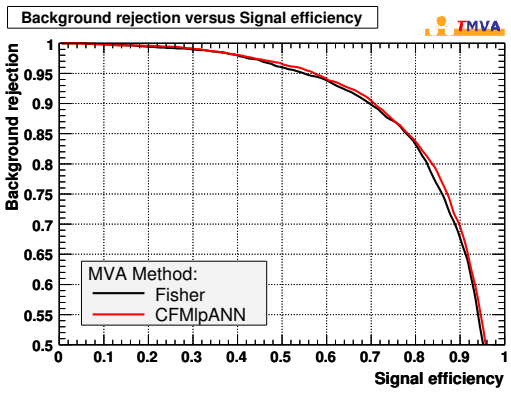

Figure 4.6: Background rejection versus the signal efficiency for the discrimination techniques Fisher discriminant and Neural Net (CFMlpANN).

Cut Optimization

The optimal Neural Net cut is chosen by determining the maximum of the significance. For that purpose we have written an own procedure and we have implemented this function in the TMVA software package. Furthermore, we have programmed an own `Root` macro for evaluation and added this macro to the TMVA package too. Denoting ε_S as signal efficiency, ε_B as background efficiency and N as the total number of events, the significance is calculated as follows:

$$\begin{aligned} \textit{significance} &= \frac{S}{\sqrt{N}} = \frac{S \cdot \epsilon_S}{\sqrt{S \cdot \epsilon_S + B \cdot \epsilon_B}} \\ &= \sqrt{S}\frac{\epsilon_S}{\sqrt{\epsilon_S + \frac{B}{S} \cdot \epsilon_B}} \end{aligned} \tag{4.7}$$

The efficiencies are provided by TMVA as a function of the Neural Net cut. The variables S and B are the expected numbers of signal and background events which has to be determined beforehand. In this analysis these numbers are specified by using the signal box as defined in Tab. 4.3. The expected numbers of signal and background events are $S = 2740$ and $B = 10215$. The resulting significance is plotted in Fig. 4.7 where the optimal cut at the maximum is determined as:

$$cut_{NN}^{opt} = 0.661$$

When applying the Neural Net cut on the mixed Monte Carlo sample for Run 1-4, a significant suppression of the continuum background is obtained. Fig. 4.8 shows the ΔE distribution for the reconstructed decay $B^0 \to D^-\pi^+$ with respect to the Monte Carlo decomposition before and after the Neural Net cut.

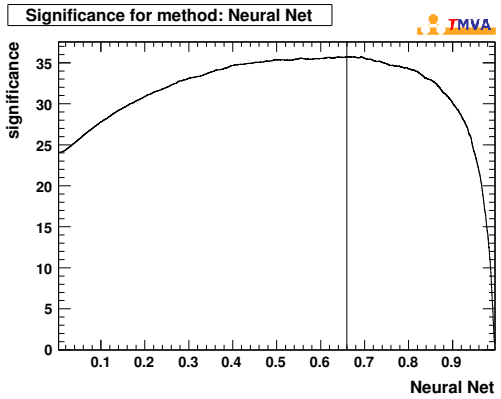

Figure 4.7: Significance plot for the Neural Net. The vertical line marks the optimal cut.

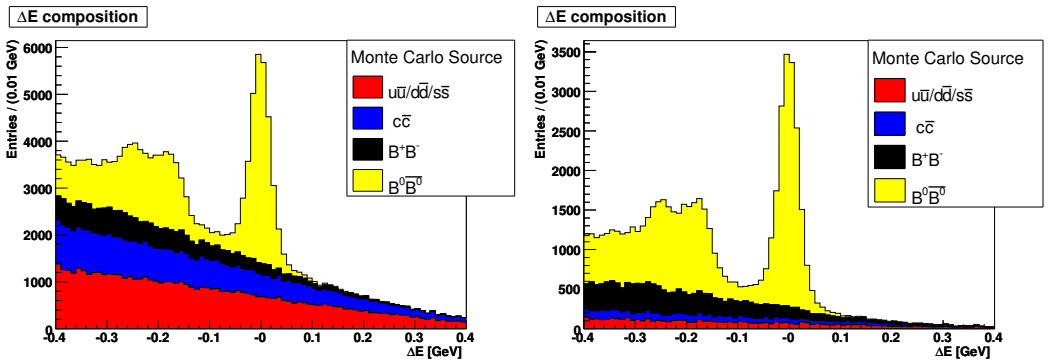

(a) before the Neural Net cut

(b) after the Neural Net cut

Figure 4.8: The plot on the left shows the ΔE distribution for the reconstructed decay $B^0 \to D^- \pi^+$ before the Neural Net cut and the right one after the cut has been applied, for the mixed Monte Carlo sample (Run 1-4).

	Events with multiple cand.	N_{multi}/N_{tot}	D combinations	π combination
Monte Carlo	21120	4.3%	20467	653
Data	22252	4.7%	21460	792

Table 4.5: The number of multiple candidates with the same decay mode in the Monte Carlo and the data sample after the event reconstruction for Run 1-4 is quoted. N_{multi}/N_{tot} is the ratio between the total events and the events with multiple candidates with the same decay mode.

4.4.3 Best B Meson Selection

When reconstructing events on `Beta` level, more than one B meson candidate may be reconstructed due to the different possible particle combinations. These events contain more than one B candidate, whereas each of them has the same decay mode $B^0 \to D^-\pi^+$ ($D^- \to K^+\pi^-\pi^-$). A summary of the number of multiple candidates per event with the same decay mode and the particle combinations, defined in the following, is quoted in Tab. 4.5. The values refer to the mixed Monte Carlo and the data sample after the event reconstruction without any cuts.
We distinguish between the two particle combinations.

D combination The B candidates in the event with the same decay mode differ in their values for ΔE and the invariant $K\pi\pi$ mass.

π combination All B candidates in the event with the same decay mode have the same invariant $K\pi\pi$ mass, but a different ΔE value. In that case the D meson is combined with another pion to form the B meson.

In order to select one of the B meson candidates with the same decay mode the invariant $K\pi\pi$ mass is used.
If a D combination is found in the event, the B candidate with an invariant $K\pi\pi$ mass closest to the nominal D meson mass $m_{D^-} = 1.8693\,\mathrm{GeV}/c^2$ [6] is selected. If there are several possible combinations of a D meson with pions, one of them is chosen randomly. Otherwise if an event contains D and π combinations, the decision between the π combination and the best D combination is randomly as well.

4.4.4 D Mass Cut

A further option to suppress the background of continuum events is provided by a tighter cut on the invariant $K\pi\pi$ mass. Fig. 4.9 shows the invariant $K\pi\pi$ mass distribution for the reconstructed decay $B^0 \to D^-\pi^+$. The vertical lines in this representation mark the tighter cut range which is set to:

$$1.8550\,\mathrm{GeV}/c^2 < m_{K\pi\pi} < 1.8825\,\mathrm{GeV}/c^2$$

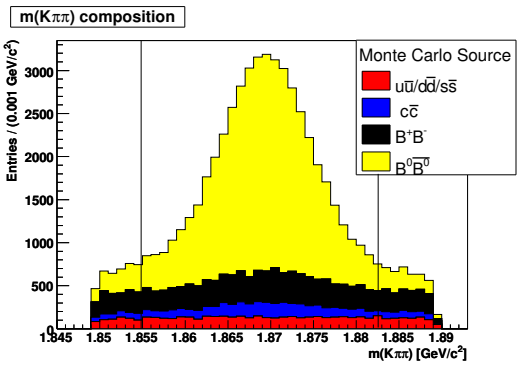

Figure 4.9: Invariant $K\pi\pi$ mass distribution for the reconstructed decay $B^0 \to D^-\pi^+$.

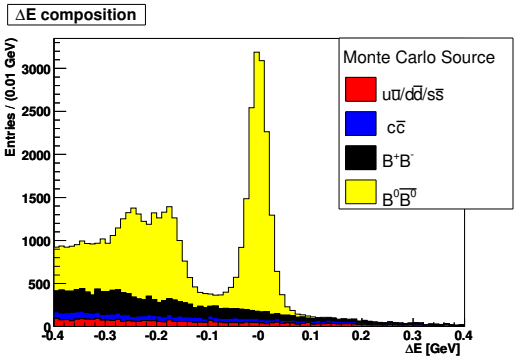

Figure 4.10: ΔE spectrum for the simulated decay $B^0 \to D^-\pi^+$ with the Neural Net cut, $m_{\mathrm{ES}} > 5.26\,\mathrm{GeV}/c^2$, $1.8550\,\mathrm{GeV}/c^2 < m_{K\pi\pi} < 1.8825\,\mathrm{GeV}/c^2$ and the best B meson candidate selection.

Fig. 4.10 shows the resulting ΔE spectrum on the Monte Carlo sample when all cuts are applied.
Now, the double peak structure of the signal events $B^0 \to D^{*-}\pi^+$ at negative ΔE values is clearly visible.

4.4.5 ΔE Shift

Comparing the ΔE distribution when reconstructing the decay $B^0 \to D^-\pi^+$ on the mixed Monte Carlo sample and on data, we observe a clear difference between both near $\Delta E = 0$, as shown in Fig. 4.11. For the comparison we use the fit strategy as presented in chapter 5 and we define pull values

$$pull = \frac{data - fit}{\sqrt{\sigma^2_{data} + \sigma^2_{fit}}}, \tag{4.8}$$

where the σ_i are the statistical errors. The pull is calculated for each bin and the

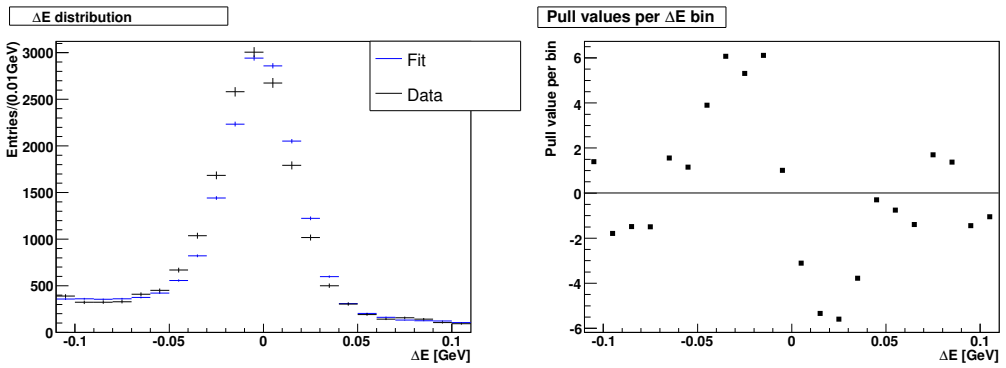

Figure 4.11: Comparison of the ΔE spectrum between data and Monte Carlo simulation before the ΔE shift. The focus is on the range $-0.1\,\text{GeV} < \Delta E < 0.1\,\text{GeV}$. The peak at $\Delta E = 0$ is one of the criteria used to find the optimal shift. On the right the pull distribution, as described in the text, is plotted. The structure around $\Delta E \approx 0$ is obvious.

pull value is filled in the corresponding bin of the ΔE distribution. Large deviations indicate a discrepancy between the Monte Carlo simulation and the data.
The pull distribution in Fig. 4.11 shows that the discrepancy might be caused by a systematic shift in ΔE. This shift is very important in our analysis. A difference between Monte Carlo and data is not negligible because the fit procedure uses the shape of ΔE distributions to extract the number of signal events $N_{D\pi}$ and $N^{\pi^0}_{D\pi}$.
To correct the shift in the ΔE spectrum, all Monte Carlo events are shifted by a constant value of ΔE and the best value for the shift is determined by minimizing the global χ^2 of the fit. We obtain the ΔE shift

$$shift_{\Delta E} = -3.5\,\text{MeV}.$$

The resulting comparison between data and fit and the corresponding pull distribution as a function of ΔE are shown in Fig. 4.12.
In the entire analysis all Monte Carlo events are shifted in ΔE by $-3.5\,\text{MeV}$.

We exclude that this shift is caused by a difference [26] between the real beam energy delivered by PEP-II and the value assumed in the reconstruction because our software release, used for the event reconstruction, contains the corrected values for the beam energy.
The origin of this effect has not been completely identified, but we suppose that the shift might be caused by uncertainties of the measurement of the particle momenta due to uncertainties from the track reconstruction.

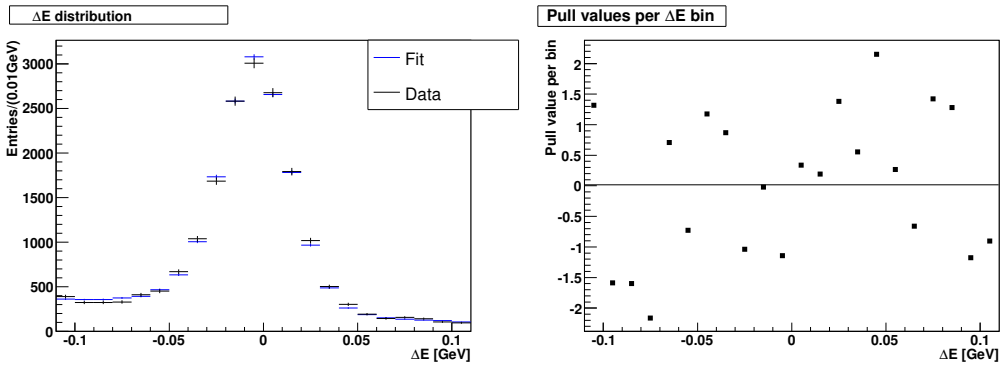

Figure 4.12: Comparison of the ΔE spectrum between data and Monte Carlo after the ΔE shift. The pull plot on the right shows that the structure around $\Delta E = 0$ has almost disappeared.

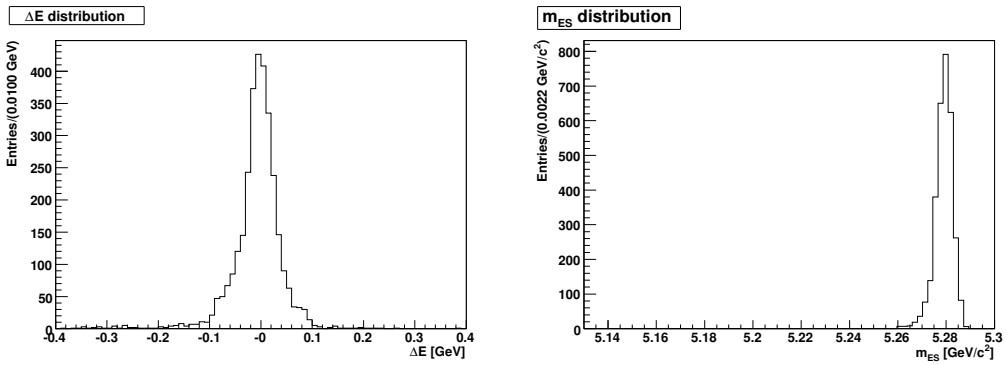

Figure 4.13: ΔE and m_{ES} distribution for the generated and reconstructed signal decay $B^0 \to D^{*-}\pi^+$

4.5 Refined Event Selection for the Decay $B^0 \to D^{*-}\pi^+$

In this subchapter the refined event selection for the decay $B^0 \to D^{*-}\pi^+$ with $D^{*-} \to D^-\pi^0$ is discussed. First, we analyze the expected ΔE and m_{ES} distributions. All cuts which are determined for the decay $B^0 \to D^-\pi^+$ are also applied for this decay without any change. Afterwards an additional cut on the difference between the mass of the D^* and the D meson is presented.

4.5.1 ΔE and m_{ES} Distribution

We expect that the signal events $B^0 \to D^{*-}\pi^+$ peak in the ΔE spectrum of the reconstructed decay $B^0 \to D^{*-}\pi^+$ at $\Delta E \approx 0$. The corresponding ΔE and m_{ES} spectrum is shown in Fig. 4.13, based on the mixed Monte Carlo sample and contains no background events because only the decay $B^0 \to D^{*-}\pi^+$ is simulated. An illustration of the ΔE and m_{ES} distribution for all generated decays which are reconstructed as $B^0 \to D^{*-}\pi^+$ is shown in Fig. 4.14. The peak in the range $0.1\,\mathrm{GeV} < \Delta E < 0.3\,\mathrm{GeV}$ comes mainly from true decays $B^0 \to D^-\pi^+$ which are incorrectly reconstructed by adding a π^0. In the further analysis they are denoted as pseudo signal.
To reduce the background, we define a further cut criterion.

4.5.2 ΔM cut

The difference between the invariant $(K\pi\pi)\pi^0$ and $K\pi\pi$ mass, defined as $\Delta M = |m_{(K\pi\pi)\pi^0} - m_{K\pi\pi}|$, offers the opportunity to reduce the background further, as shown in Fig. 4.15. The expected signal peak is at the nominal mass difference $m_{D^{*-}} - m_{D^-} = 140.64\,\mathrm{MeV}/c^2$ [6]. Fig. 4.15 shows also the specified cut range which we have chosen in that way that no signal is lost according to Fig. 4.16.

$$\Delta M < 0.147\,\mathrm{GeV}/c^2$$

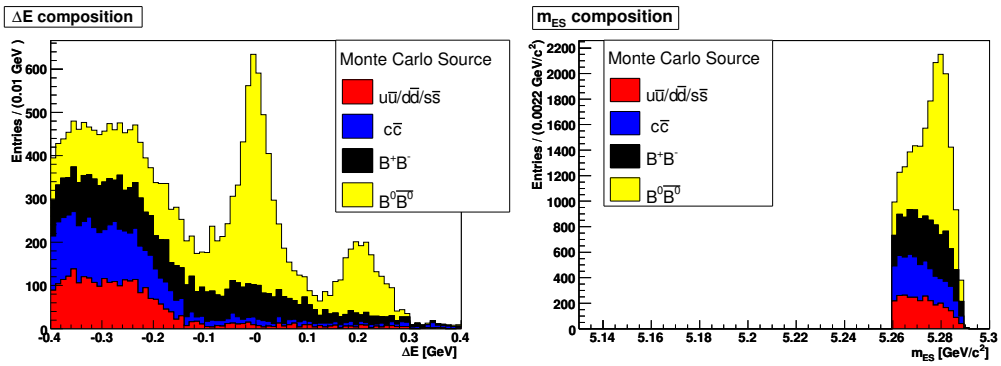

Figure 4.14: ΔE and m_{ES} distribution for all generated decays which are reconstructed as $B^0 \to D^{*-}\pi^+$. The various Monte Carlo sources are distinguished using different colors.

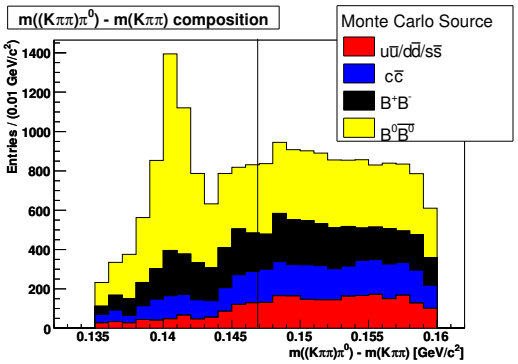

Figure 4.15: ΔM distribution for the reconstructed decay $B^0 \to D^{*-}\pi^+$. The variable ΔM is defined as invariant mass difference $\Delta M = |m_{(K\pi\pi)\pi^0} - m_{K\pi\pi}|$. The different Monte Carlo sources are denoted with colors.

A tighter cut on ΔM would cause a bias of our π^0 efficiency study which we want to avoid. The plot of the ΔE spectrum when all cuts are applied is shown in Fig. 4.17. There can be seen that the background has been reduced significantly compared to Fig. 4.14.

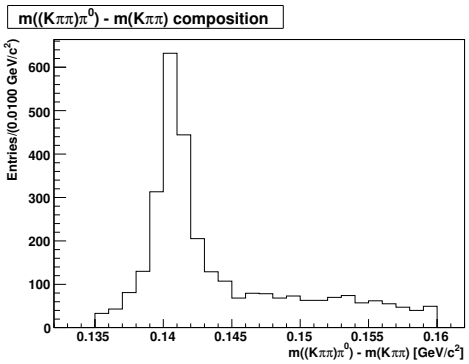

Figure 4.16: ΔM distribution for the generated and reconstructed decay $B^0 \to D^{*-}\pi^+$ on the mixed Monte Carlo sample.

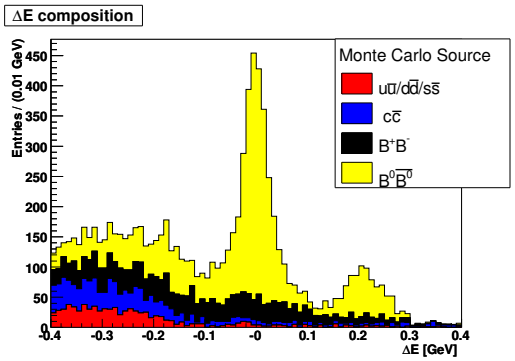

Figure 4.17: Final ΔE distribution for the reconstructed decay $B^0 \to D^{*-}\pi^+$ with the ΔM cut included.

4.6 Background Studies

In this chapter we compare the ΔE distributions between data and Monte Carlo simulations in details, and we study the decomposition of the background on Monte Carlo samples in order to identify the main background sources.

4.6.1 Monte Carlo and Data Comparison

In the following we compare the ΔE distributions between data and Monte Carlo simulation in three different regions in the variable m_{ES} in order to validate the background model as well as the model for the signal and the pseudo signal in the simulation.
The three m_{ES} regions are defined as follows:

- signal region: $m_{\mathrm{ES}} > 5.26\,\mathrm{GeV}/c^2$
- sideband 1: $5.24\,\mathrm{GeV}/c^2 < m_{\mathrm{ES}} < 5.26\,\mathrm{GeV}/c^2$
- sideband 2: $m_{\mathrm{ES}} < 5.24\,\mathrm{GeV}/c^2$

The comparison is performed separately for the reconstructed decay $B^0 \to D^-\pi^+$ and $B^0 \to D^{*-}\pi^+$ and is based on the mixed Monte Carlo sample which is scaled to data luminosity.

Monte Carlo and Data Comparison for the Reconstructed Decay $B^0 \to D^-\pi^+$

In general we find a good agreement of the ΔE spectra between data and the Monte Carlo simulation. The signal region, illustrated in Fig. 4.18, shows deviations near $\Delta E = 0$ and in the range $-0.3\,\mathrm{GeV} < \Delta E < -0.2\,\mathrm{GeV}$. In sideband 1 and 2 the simulation and the data agree very well, as shown in Fig. 4.19 and Fig. 4.20.

Monte Carlo and Data Comparison for the Reconstructed Decay $B^0 \to D^{*-}\pi^+$

We find again a good agreement between data and Monte Carlo simulation in all three m_{ES} regions. In the signal region, shown in Fig. 4.21, we observe small deviations at $\Delta E = 0$ and in the range $-0.3\,\mathrm{GeV} < \Delta E < -0.2\,\mathrm{GeV}$. Data and Monte Carlo simulation agree well in sideband 1, as shown in Fig. 4.22. In sideband 2, shown in Fig. 4.23, the simulation underestimates the data and a slight positive slope in the ratio between data and Monte Carlo simulation can not be excluded.

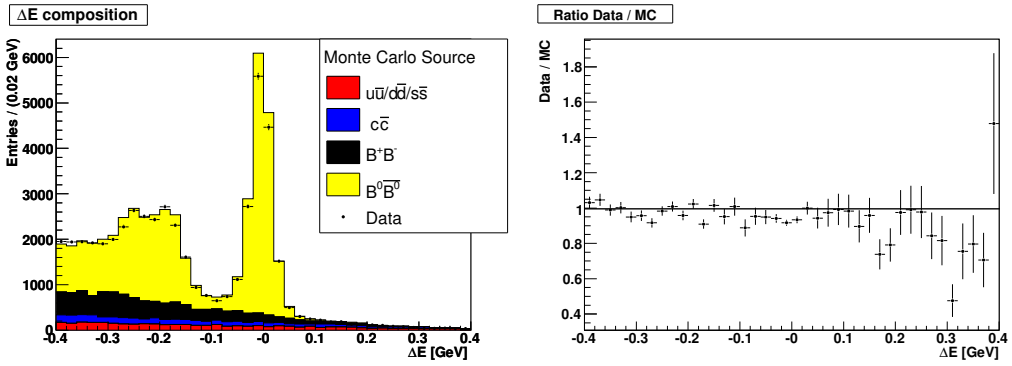

Figure 4.18: Monte Carlo and Data Comparison for the reconstructed decay $B^0 \to D^-\pi^+$ in the defined signal region ($m_{\mathrm{ES}} > 5.26\,\mathrm{GeV}/c^2$). The plot on the right shows the ratio between data and Monte Carlo simulation.

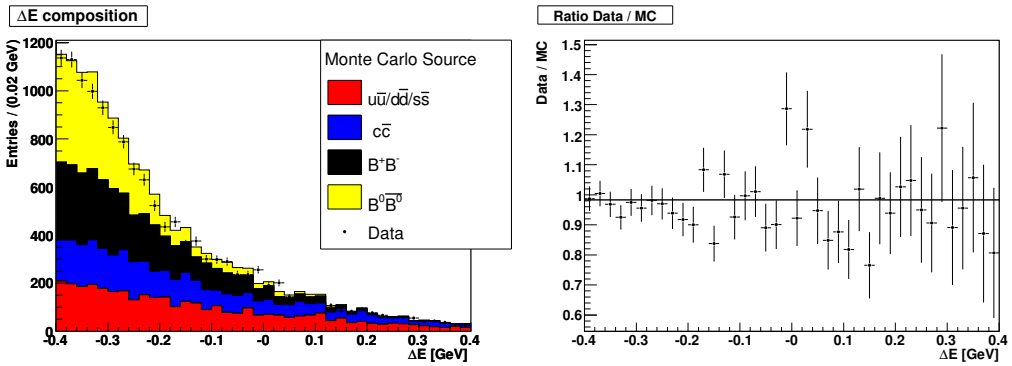

Figure 4.19: Monte Carlo and Data Comparison for the reconstructed decay $B^0 \to D^-\pi^+$ in the defined sideband 1 ($5.24\,\mathrm{GeV}/c^2 < m_{\mathrm{ES}} < 5.26\,\mathrm{GeV}/c^2$). The plot on the right shows the ratio between data and Monte Carlo simulation.

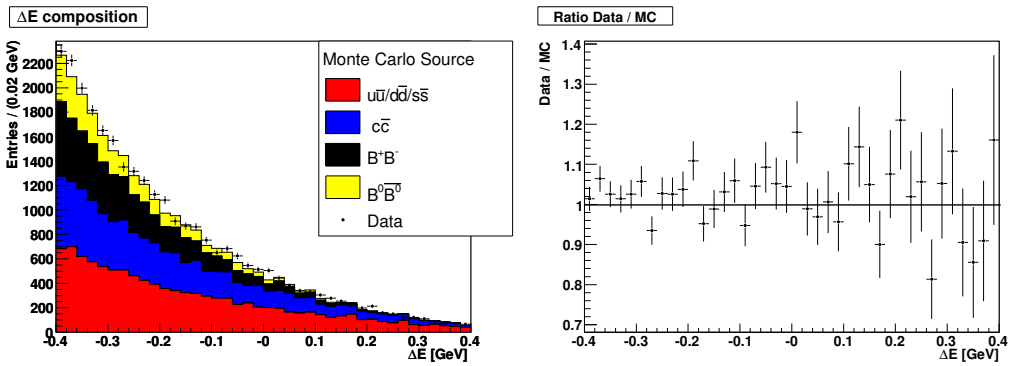

Figure 4.20: Monte Carlo and Data Comparison for the reconstructed decay $B^0 \to D^-\pi^+$ in the defined sideband 2 ($m_{\mathrm{ES}} < 5.24\,\mathrm{GeV}/c^2$). The plot on the right shows the ratio between data and Monte Carlo simulation.

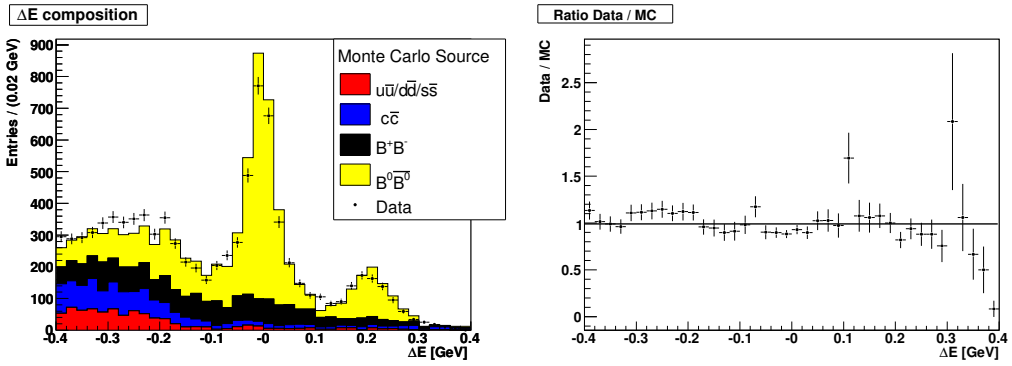

Figure 4.21: Monte Carlo and Data Comparison for the reconstructed decay $B^0 \to D^{*-}\pi^+$ in the defined signal region ($m_{\mathrm{ES}} > 5.26\,\mathrm{GeV}/c^2$). The plot on the right shows the ratio between data and Monte Carlo simulation.

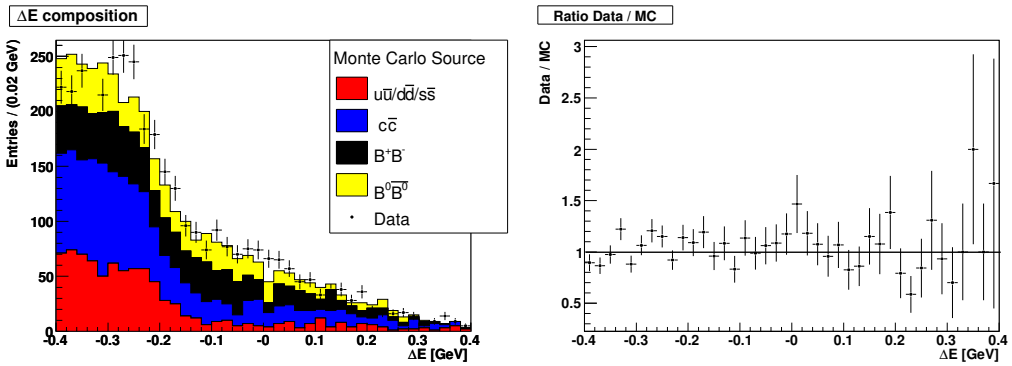

Figure 4.22: Monte Carlo and Data Comparison for the reconstructed decay $B^0 \to D^{*-}\pi^+$ in the defined sideband 1 ($5.24\,\mathrm{GeV}/c^2 < m_{\mathrm{ES}} < 5.26\,\mathrm{GeV}/c^2$). The plot on the right shows the ratio between data and Monte Carlo simulation.

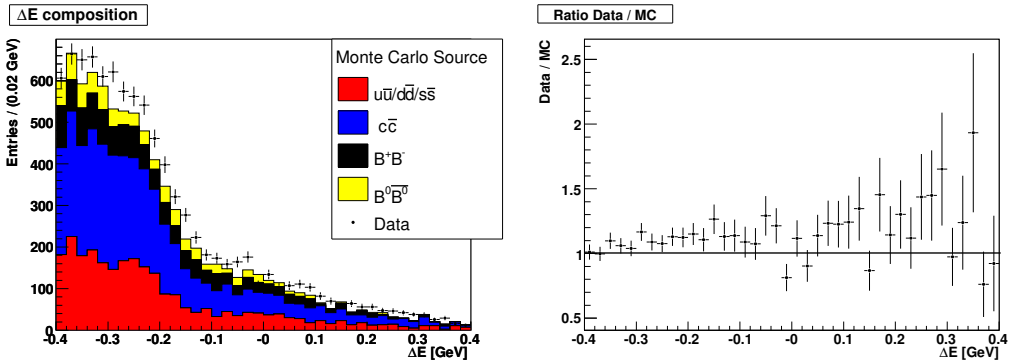

Figure 4.23: Monte Carlo and Data Comparison for the reconstructed decay $B^0 \to D^{*-}\pi^+$ in the defined sideband 2 ($m_{\mathrm{ES}} < 5.24\,\mathrm{GeV}/c^2$). The plot on the right shows the ratio between data and Monte Carlo simulation.

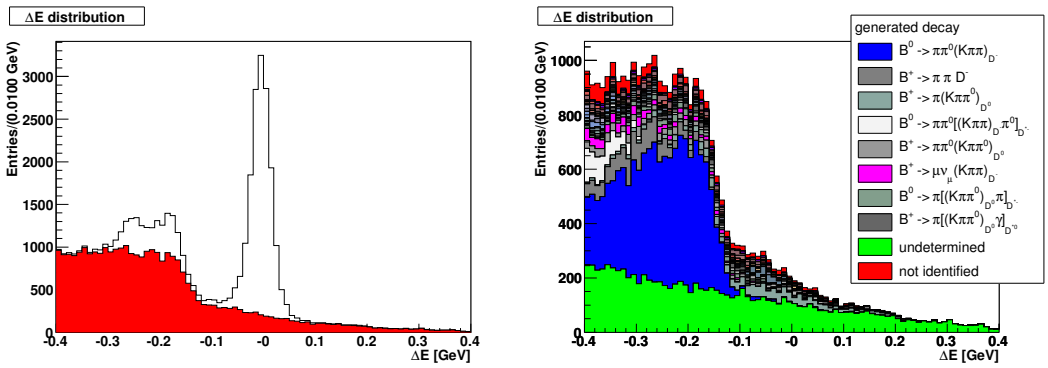

Figure 4.24: The background decomposition in ΔE for the reconstructed decay $B^0 \to D^-\pi^+$ is shown. The peaks in the left plot correspond to the signal ($-0.3\,\text{GeV} < \Delta E < -0.1\,\text{GeV}$) and the pseudo signal ($\Delta E \approx 0$). The background contribution is marked in red. In the plot on the right each simulated and identified background decay is added up and denoted by a unique color. The legend lists the main B background decays.

4.6.2 Background Decomposition in the $B^0 \to D^-\pi^+$ Reconstruction

In this chapter we determine the type and the shape of the background decays in the ΔE spectrum of the reconstructed decay $B^0 \to D^-\pi^+$. Afterwards, we study the single background contributions in details.
In Fig. 4.24 the ΔE distribution of the reconstructed decay $B^0 \to D^-\pi^+$ is shown, decomposed of the signal, the pseudo signal and the background, consisting of all generated decays which are reconstructed as $B^0 \to D^-\pi^+$. In the plot on the right in Fig. 4.24 each background decay which contributes to the ΔE spectrum is added up separately. Almost 96% of the background decays are identified by their decay mode number. A significant part of the background decays peaks in the signal region $-0.3\,\text{GeV} < \Delta E < -0.1\,\text{GeV}$.
We denote background decays as "undetermined" if no simulated B decay mode could be assigned. This kind of background consists mainly of combinatorial background. It is also possible that for a certain B decay no decay mode number could be calculated, but this fraction is rather small.
The main B background decays we have identified are:

- $B^0 \to \pi^+\pi^0 D^-$ (approx. 36%)
- $B^+ \to D^-\pi^+\pi^+$ (approx. 5%)
- $B^+ \to \pi^+ D^0, D^0 \to K^-\pi^+\pi^0$ (approx. 4%)

We expect that the decays listed and especially the decay $B^0 \to \pi^+\pi^0 D^-$ are the main sources of the systematic uncertainties.

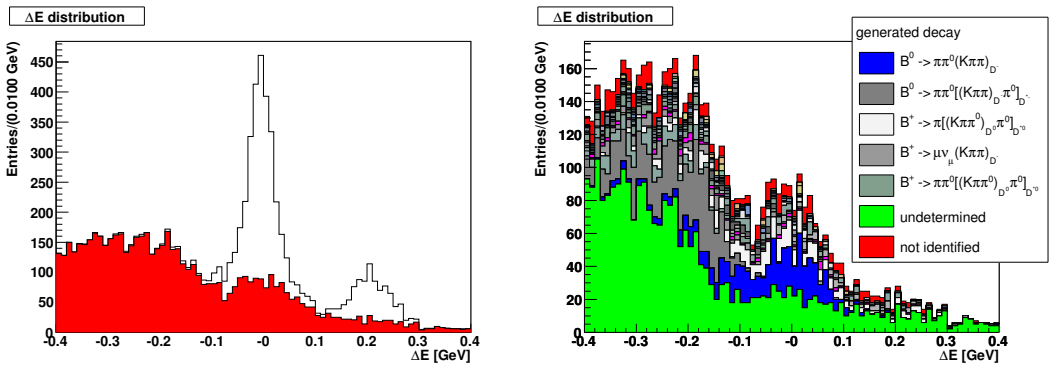

Figure 4.25: The background decomposition in ΔE for the reconstructed decay $B^0 \to D^{*-}\pi^+$ is shown. The complete background is marked in red. The peak at $\Delta E \approx 0$ corresponds to the signal and the peak in the region $0.1\,\text{GeV} < \Delta E < 0.3\,\text{GeV}$ to the pseudo signal. In the plot on the right each simulated and identified background decay is added up and denoted by a unique color. The legend lists the main B background decays.

4.6.3 Background Decomposition in the $B^0 \to D^{*-}\pi^+$ Reconstruction

We have performed the background study also for the reconstructed decay $B^0 \to D^{*-}\pi^+$ in order to determine the type and the shape of the background decays, followed by an analysis of the single background contributions.
Fig. 4.25 shows the ΔE spectrum of the reconstructed decay $B^0 \to D^{*-}\pi^+$ which is decomposed of the signal, the pseudo signal and the background. The background consists of all generated decays reconstructed as $B^0 \to D^{*-}\pi^+$.
In addition each background decay contributing to the ΔE distribution is added up separately in the plot on the right in Fig. 4.25. We identify approximately 95% of the background decays by their decay mode number. Again, a significant part of the background decays peaks in the signal region close to $\Delta E = 0$.
The background is dominated by the following B decays:

- $B^0 \to \pi^+\pi^0 D^{*-}, D^{*-} \to D^-\pi^0$ (approx. 13%)
- $B^0 \to \pi^+\pi^0 D^-$ (approx. 9%)
- $B^+ \to \pi^+ D^{*0}, D^{*0} \to D^0\pi^0$ (approx. 6%)

We expect that the decays $B^0 \to \pi^+\pi^0 D^{*-}$ and $B^+ \to \pi^+ D^{*0}$ also contribute to the systematic uncertainties.

Chapter 5

Binned χ^2 Fit

In this chapter we present the fit procedure, applied to extract the number of signal events $N_{D\pi}$ and $N_{D\pi}^{\pi^0}$. At first we explain the fit strategy and give an introduction of the method, followed by a discussion of the single fit components. Finally, the fit model is tested and validated on the mixed Monte Carlo sample.

5.1 Fit Strategy

We determine the signal yields $N_{D\pi}$ and $N_{D\pi}^{\pi^0}$ in a fit of the ΔE distribution to four different contributions.

1. signal
2. pseudo signal
3. B background
4. combinatorial background mainly coming from continuum events

The background studies performed in chapter 4.6 have shown that a parametrization of signal, pseudo signal and in particular B background is very challenging if not unfeasible. However, the studies suggest that the shape of the combinatorial background could be parametrized by a first or second order polynomial.
Thus, we use the histograms for signal, pseudo signal and B background as parametrization and describe the combinatorial background by an analytical function. We perform a binned χ^2 fit and use the four components as input in the fit.
The free parameters in the fit are:

- the relative contributions of the four components to the ΔE spectrum
- the shape parameters for the combinatorial background

The technical implementation of the fit routine is programmed with the `Minuit` minimization package [27] which is part of the `Root` software. For that purpose, we have written an own minimization routine in order to take the errors from the Monte Carlo histograms explicitly into account.

5.1.1 χ^2 Method

In this section a short introduction into the χ^2 method is given, based on Refs.[28, 29].

The χ^2 method is a common technique for estimating parameters from a given set of observations. A typical problem consists mostly of two different types of variables, precisely known x values and a set of data with N measurements $y_1, y_2, \ldots, y_N$. The theory prediction for any x value is given by the expression $f(x_i, a)$, where a is a parameter. In the χ^2 method the weighted squared difference between this set of N measurements and their prediction $f(x_i, a)$ is minimized with respect to the parameter a in order to provide an estimate for the parameter a.

$$\chi^2 \equiv \sum_{i=1}^{N} \frac{(y_i - f(x_i, a))^2}{\sigma_i^2} \tag{5.1}$$

Here, σ_i is the error on the theoretical prediction. The parameter estimator $\hat{a}$ is given by $\frac{d\chi^2}{da}|_{\hat{a}} = 0$.
The χ^2 method can also be applied on problems with k parameters $a_1, a_2, a_3, \ldots, a_k$ using the matrix notation. In that case the measurements y_i are written as $\boldsymbol{y}$ and the theory prediction $f(x_i, \boldsymbol{a})$ as $\boldsymbol{f}$, where $\boldsymbol{a}$ is a vector of k elements. The variances σ_i^2 can be grouped in a covariance matrix $\boldsymbol{V}$ and Eq. 5.1 can be expressed in matrix notation as

$$\chi^2 = (\boldsymbol{y} - \boldsymbol{f})^T \boldsymbol{V}^{-1} (\boldsymbol{y} - \boldsymbol{f}) \tag{5.2}$$

The parameter estimator $\hat{\boldsymbol{a}}$ is given by solving the k equations $\frac{\partial \chi^2}{\partial a_k}|_{\hat{\boldsymbol{a}}} = 0 \; \forall \; k$.

Fitting binned data

After binning a dataset with N events, every bin i contains n_i events. The prediction for the expected events for each bin i with the width W_i can be approximated as $\mu_i = NW_i f(x_i, a)$ with the probability function $f(x_i, a)$. The number of events per bin i is described by Poisson statistics with the squared error $\sigma_i^2 = \mu_i$.

$$\chi^2 = \sum_{i=1}^{N_{bins}} \frac{(n_i - \mu_i)^2}{\mu_i} \tag{5.3}$$

For large μ_i the variance σ_i^2 of the number of events in bin i is approximately equal to the number of observed events n_i.
With $\sigma_i^2 \approx n_i$ the χ^2 formula can be approximated as:

$$\chi^2 \approx \sum_{i=1}^{N_{bins}} \frac{(n_i - \mu_i)^2}{n_i} \tag{5.4}$$

Our analysis uses the approximate χ^2 computation as given in Eq. 5.4.

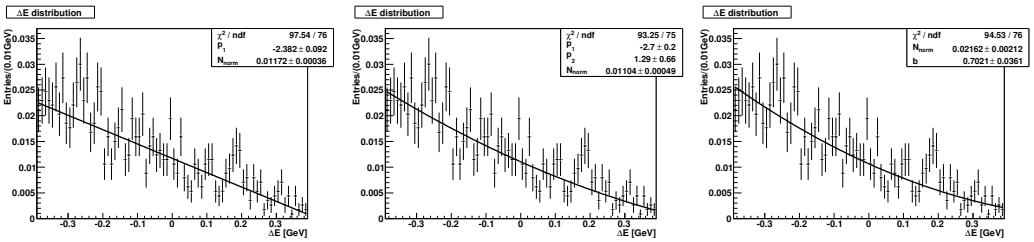

(a) $Prob_{\chi^2} = 4.8\%$ (b) $Prob_{\chi^2} = 7.5\%$ (c) $Prob_{\chi^2} = 7.4\%$

Figure 5.1: Three different functions are fitted to the ΔE distribution of the combinatorial background for the reconstructed decay $B^0 \to D^-\pi^+$. Below, the fit probability is quoted. (a) $f_1(\Delta E) = N_{norm} \cdot (1 + p_1 \cdot \Delta E)$, (b) $f_2(\Delta E) = N_{norm} \cdot (1 + p_1 \cdot \Delta E + p_2 \cdot \Delta E^2)$, (c) $f_3(\Delta E) = N_{norm} \cdot (\Delta E - b)^2$

5.1.2 Building the Monte Carlo Model

The three different input histograms for the fit components signal, pseudo signal and B background are generated with simulated events from the Monte Carlo Model sample and only $B\overline{B}$ decays of this sample are used. In addition a histogram, filled with continuum events from this Monte Carlo sample, is generated and denoted as combinatorial background histogram.
We explain each fit component in the following section for the considered decays separately. All histograms used in the fit are normalized to one.

To improve the agreement between the Monte Carlo simulation and data, we use the latest branching fractions [6] by reweighing the events. A complete list of the reweighed decays is quoted in Tab. 6.6.

Parametrization of the combinatorial background

The background studies, performed in chapter 4.6, suggest that the combinatorial background could be described by a first or second order polynomial. Therefore, we tested three different approaches to parametrize the shape of this background.

1. $f_1(\Delta E) = N_{norm} \cdot (1 + p_1 \cdot \Delta E)$
2. $f_2(\Delta E) = N_{norm} \cdot (1 + p_1 \cdot \Delta E + p_2 \cdot \Delta E^2)$
3. $f_3(\Delta E) = N_{norm} \cdot (\Delta E - b)^2$

N_{norm} is a normalization factor. We have tested all three functions by fitting them to the combinatorial background histogram. Fig. 5.1 shows the results and the corresponding fit probability.
The best result is achieved with the function $f_3(\Delta E) = N_{norm} \cdot (\Delta E - b)^2$.

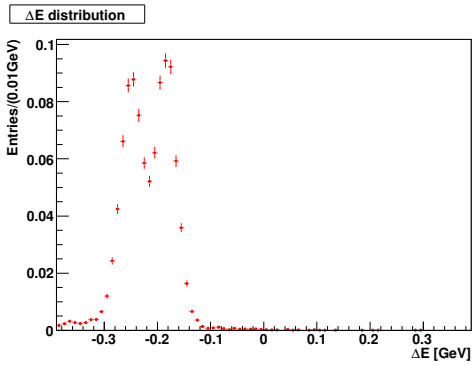

Figure 5.2: ΔE distribution of the signal events $B^0 \to D^{*-}\pi^+$, which are reconstructed as $B^0 \to D^-\pi^+$.

Hence, we parametrize the shape of the combinatorial background by

$$f(\Delta E) = N_{norm} \cdot (\Delta E - b)^2 \tag{5.5}$$

The function is characterized by the normalization factor N_{norm} and the parameter b. For clarification, the global χ^2 fit procedure is performed in two steps concerning the parametrization of the combinatorial background. First the function 5.5 is fitted to the combinatorial background histogram. The values for the parameters, determined in this first step, are used as initial values for the global χ^2 fit, where N_{norm} and b are treated as free parameters.

Monte Carlo Model in the $B^0 \to D^-\pi^+$ Analysis

In the following section we present the individual fit components used in the $B^0 \to D^-\pi^+$ analysis.
Fig. 5.2 shows our signal histogram. The ΔE distribution for the pseudo signal is illustrated in Fig. 5.3. The ΔE spectrum of the B background is shown in Fig. 5.4. In Fig. 5.5 the combinatorial background histogram and the fitted function is shown. A summary of all fit components is given in Tab. 5.1. All histograms are generated with the following settings:

- ΔE range: [-0.39, 0.39] GeV, binwidth = 0.01 GeV
- ΔE fit range: [-0.39, 0.39] GeV
- normalization to one

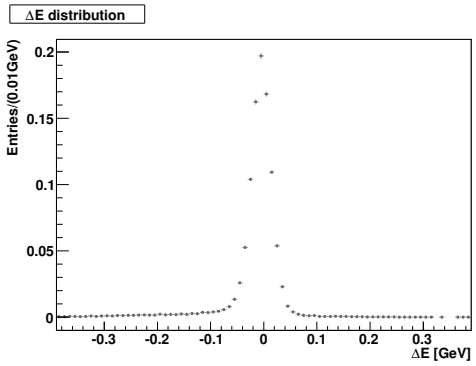

Figure 5.3: ΔE distribution of the pseudo signal. The decay is generated and reconstructed as $B^0 \to D^- \pi^+$.

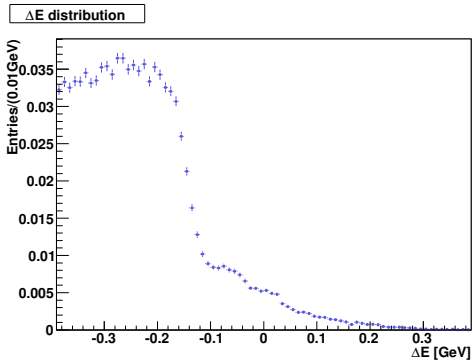

Figure 5.4: ΔE distribution of the B background, which consists of all generated B decays reconstructed as $B^0 \to D^- \pi^+$.

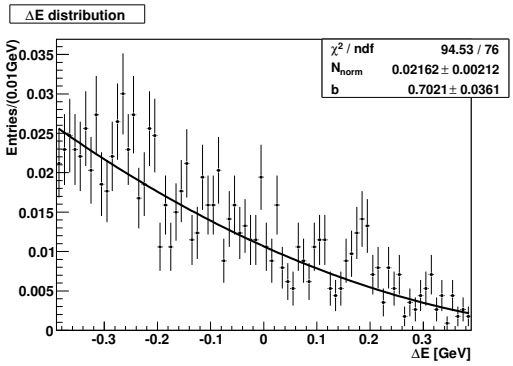

Figure 5.5: ΔE distribution of the combinatorial background in the $B^0 \to D^- \pi^+$ analysis. The shape is fitted with the function $f(\Delta E) = N_{norm} \cdot (\Delta E - b)^2$ (Eq. 5.5).

Fit Components	ΔE distribution for the decay	
	generated as	reconstructed as
signal	$B^0 \to D^{*-}\pi^+$	$B^0 \to D^-\pi^+$
pseudo signal	$B^0 \to D^-\pi^+$	$B^0 \to D^-\pi^+$
B background	all B decay modes (except signal and pseudo signal)	$B^0 \to D^-\pi^+$
combinatorial background	—	$B^0 \to D^-\pi^+$

Table 5.1: Definition of the fit components in the $B^0 \to D^-\pi^+$ analysis

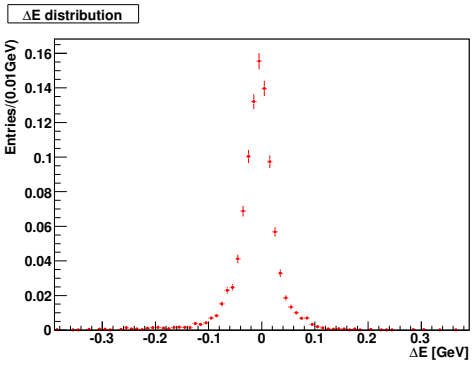

Figure 5.6: ΔE distribution of the signal which is generated and reconstructed as $B^0 \to D^{*-}\pi^+$.

Monte Carlo Model in the $B^0 \to D^{*-}\pi^+$Analysis

In this chapter we present the fit components in the $B^0 \to D^{*-}\pi^+$analysis.
The ΔE spectrum for the signal is shown in Fig.5.6 and for the pseudo signal in Fig. 5.7. The ΔE distribution of the B background is shown in Fig. 5.8. In Fig. 5.9 the combinatorial background histogram and the fitted function are shown.
A summary of all fit components is quoted in Tab. 5.2. The histograms of the ΔE spectrum are generated with the following settings:

- ΔE range: [-0.39, 0.39] GeV, binwidth=0.01 GeV
- ΔE fit range: [-0.1 , 0.39] GeV, binwidth=0.01 GeV
- normalization to one

The reason for the different fit range in ΔE compared to the fit range in the $B^0 \to D^-\pi^+$ analysis is that the shape of the combinatorial background can not be parametrized with the analytical function, described in Eq.5.5, for ΔE values below -0.1 GeV. Thus, we only fit the limited ΔE range, where a parametrization of the combinatorial background by the function, described in Eq.5.5, is possible.

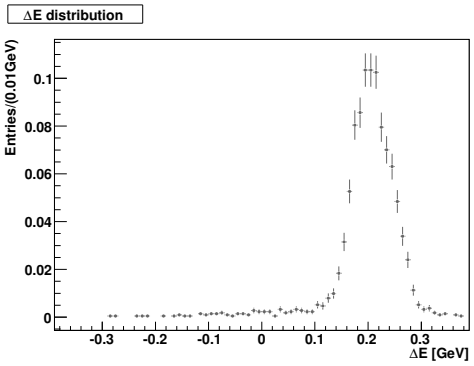

Figure 5.7: ΔE distribution of the pseudo signal. The decay $B^0 \to D^- \pi^+$ is generated and reconstructed as $B^0 \to D^{*-} \pi^+$.

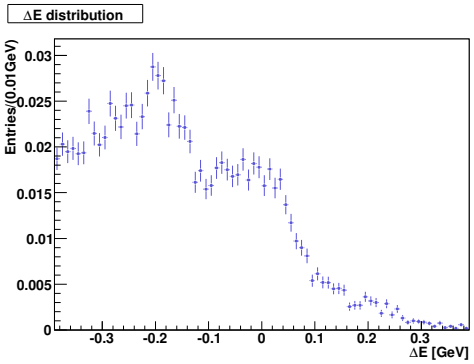

Figure 5.8: ΔE distribution of the B background where all generated B decays which are reconstructed as $B^0 \to D^- \pi^+$ are shown.

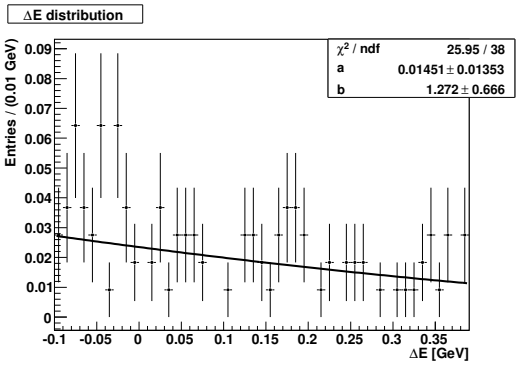

Figure 5.9: ΔE distribution of the combinatorial background in the $B^0 \to D^{*-} \pi^+$ analysis. The shape is fitted with the function $f(\Delta E) = N_{norm} \cdot (\Delta E - b)^2$ (Eq. 5.5).

Fit Components	ΔE distribution for the decay	
	generated as	reconstructed as
signal	$B^0 \to D^{*-}\pi^+$	$B^0 \to D^{*-}\pi^+$
pseudo signal	$B^0 \to D^{-}\pi^+$	$B^0 \to D^{*-}\pi^+$
B background	all B decay modes (except signal and pseudo signal)	$B^0 \to D^{*-}\pi^+$
combinatorial background	—	$B^0 \to D^{*-}\pi^+$

Table 5.2: Definition of the fit components in the $B^0 \to D^{*-}\pi^+$ analysis

5.1.3 Global χ^2 Fit

We define for both both fits, $B^0 \to D^-\pi^+$ and $B^0 \to D^{*-}\pi^+$, the following χ^2 function

$$\chi^2 = \sum_{i=1}^{n_{bins}^{\Delta E}} \frac{(N_{meas}^i - \mu^i)^2}{((\Delta N_{meas}^i)^2 + (\Delta N_{MC}^i)^2)} \tag{5.6}$$

where the sum is over all ΔE bins i and N_{meas}^i is the measured bin content. ΔN_{meas}^i is the statistical error of the measured bin content and ΔN_{MC}^i the statistical error for the Monte Carlo histograms. The model prediction μ^i is given by

$$\begin{aligned} \mu^i &= N_{tot}^{Data}[C_{sig} \cdot n_{sig,MC}^i + C_{pseudosig} \cdot n_{pseudosig,MC}^i + \\ &\quad + C_{BBG} \cdot n_{BBG,MC}^i + \\ &\quad + C_{combBG} \cdot n_{combBG}^i(N_{Norm}, b)] \end{aligned} \tag{5.7}$$

where the coefficients C_j are the relative contributions of the components to the ΔE spectrum and $n_{j,MC}^i$ is the ith bin content of the fit component j. By adding up the histograms for the fit components, the requirement $\mu^i > 10 \ \forall \ i$ for the approximate χ^2 calculation, described in Eq. 5.4, is always justified. All 4 fit components are normalized to one.

$$\sum_{i=1}^{n_{bins}^{\Delta E}} n_{j,MC}^i = 1 \qquad \forall j \tag{5.8}$$

In addition the prediction μ^i is constrained to the total number of events in the data histogram N_{tot}^{Data}.

$$\sum_{i=1}^{n_{bins}^{\Delta E}} \mu^i = N_{tot}^{Data} \tag{5.9}$$

In equation 5.6 the uncertainties from the Monte Carlo histograms are explicitly taken into account. The statistical error for the Monte Carlo histograms is calculated as follows:

$$(\Delta N_{MC}^i)^2 = \sum_{j=1}^{3} \left(\frac{C_j \cdot N_{tot}^{Data}}{N_j} \Delta N_{j,MC}^i \right)^2 \tag{5.10}$$

It represents a sum over the fit input histograms $j = 1, \ldots, 3$.
By using the normalization of the coefficients $\sum_{j=1}^{4} C_j = 1$ the coefficient for the combinatorial background is expressed as:

$$C_{combBG} = 1 - C_{sig} - C_{pseudosig} - C_{BBG} \tag{5.11}$$

Free Fit Parameters	
component	parameter
signal	C_{sig}
pseudo signal	$C_{pseudosig}$
B background	C_{BBG}
combinatorial background	N_{norm}, b

Table 5.3: Definition of the free fit parameters in the global χ^2 fit

The free parameters in the fit are the relative contributions of the fit components to the ΔE distribution and the shape parameters N_{norm} and b for the description of the combinatorial background by the analytic function, described in Eq.5.5. Finally the yields for the fit components are calculated using the coefficients C_j, obtained in the global χ^2 fit.
The number of degrees of freedom (*ndf*) in the fit is the difference between the number of bins in the histograms and the number of free parameters in the fit. Due to the different fit ranges the number of degrees of freedom in the $B^0 \to D^-\pi^+$ analysis is $ndf = 73$, whereas in the $B^0 \to D^{*-}\pi^+$ analysis it is $ndf = 44$. All parameters are summarized in Tab. 5.3.

5.2 Fit Validation

For the validation of the analysis, the histograms for the fit components are generated with the statistical independent events from the Monte Carlo Model sample. The fit is applied on events of the mixed Monte Carlo sample, which is treated as a dataset. The yields for signal, pseudo signal, B background and the combinatorial background are compared with the *MC Truth* information.
The results for the various fit components are summarized in Tab. 5.4. The graphical result of the fit and the individual fit components are shown in Fig. 5.10. In the fit of the reconstructed decay $B^0 \to D^-\pi^+$ we obtain a χ^2 value of $\chi^2 = 65$ (ndf=73) and for the fit of the reconstructed decay $B^0 \to D^{*-}\pi^+$ a χ^2 value of $\chi^2 = 50$ (ndf=44). Both fits have a good fit probability of $Prob_{\chi^2} = 74\%$ for the fit $B^0 \to D^-\pi^+$ and $Prob_{\chi^2} = 25\%$ for the fit $B^0 \to D^{*-}\pi^+$.
The overall results for the extracted yields are consistent with the true values within one standard deviation σ.

Fit results for the decay $B^0 \to D^- \pi^+$		
component	$N_{fit} \pm \Delta N$	N_{true}
signal	4701 ± 253 $(=N_{D\pi})$	4549
pseudo signal	15728 ± 165	15678
B background	22456 ± 755	23183
combinatorial background	7297 ± 813	6843
$\chi^2/ndf = 65/73$, $Prob(65, 73) = 74\%$		

Fit results for the decay $B^0 \to D^{*-} \pi^+$		
component	$N_{fit} \pm \Delta N$	N_{true}
signal	2349 ± 90 $(= N_{D\pi}^{\pi^0})$	2288
pseudo Signal	758 ± 42	705
B background	1497 ± 111	1542
combinatorial background	256 ± 149	392
$\chi^2/ndf = 50/44$, $Prob(50, 44) = 25\%$		

Table 5.4: Fit results on the Monte Carlo sample for the number of signal, pseudo signal, B background and combinatorial background events for both decays $B^0 \to D^- \pi^+$ and $B^0 \to D^{*-} \pi^+$. N_{true} denotes the number of true events obtained from the input histograms and N_{fit} is the number of events extracted from the fit including its fit uncertainty.

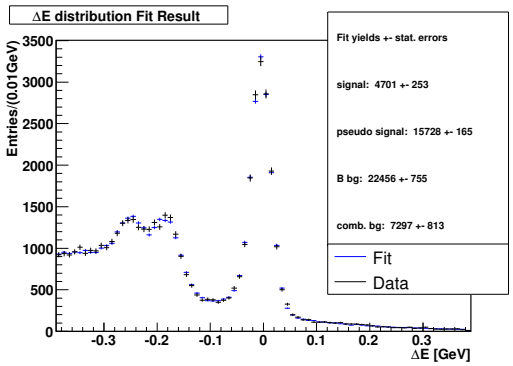

(a) Fit results for the reconstructed decay $B^0 \to D^-\pi^+$

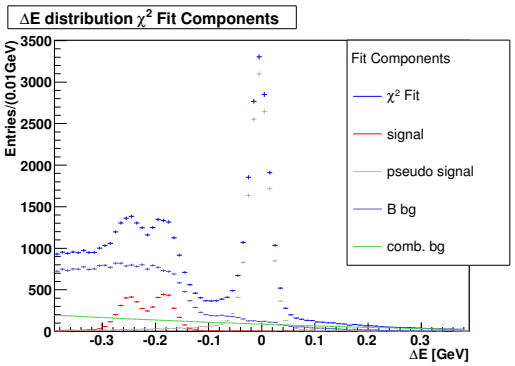

(b) Fit components for the reconstructed decay $B^0 \to D^-\pi^+$

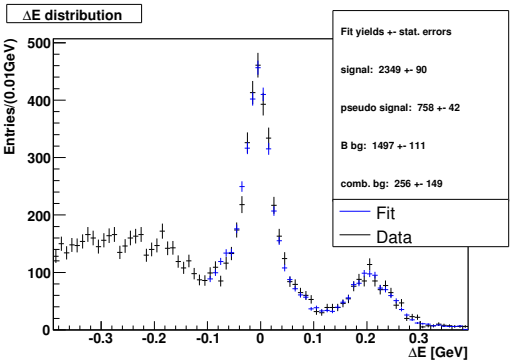

(c) Fit results for the reconstructed decay $B^0 \to D^{*-}\pi^+$

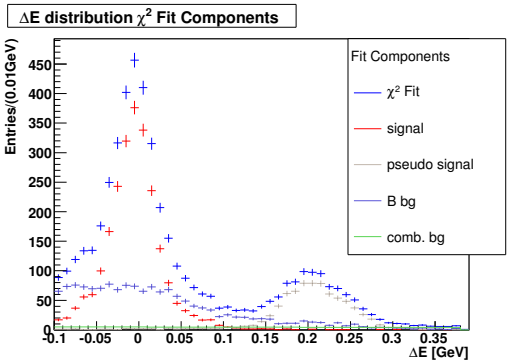

(d) Fit components for the reconstructed decay $B^0 \to D^{*-}\pi^+$

Figure 5.10: Fit results and components obtained in the validation procedure. The blue crosses correspond to the global χ^2 fit result. On the right the individual fit components are shown. Please note that from (c) to (d) the range on the x-axis has been changed.

Chapter 6

Results

In this chapter we present the results of our analysis. Applying the fit model, which is validated on Monte Carlo simulations, to real data yields results for the number of events $N_{D\pi}^{\pi^0}$ and $N_{D\pi}$ for the decay $B^0 \to D^{*-}\pi^+$. The fit results are shown in the first part, followed by two sections explaining the methods to determine the statistical and systematic uncertainties. Finally, the results are compared to previous measurements.

6.1 Results for the π^0 Efficiency in Data and Monte Carlo Simulations

As described in chapter 5, a fit model is developed on Monte Carlo simulations which is able to extract the signal yields $N_{D\pi}^{\pi^0}$ and $N_{D\pi}$ for the decay $B^0 \to D^{*-}\pi^+$ without bias. It uses a Monte Carlo model with four components fully describing the measured ΔE distributions of the reconstructed decays $B^0 \to D^-\pi^+$ and $B^0 \to D^{*-}\pi^+$. The current section focuses on the application of that fit model to the real dataset. Therefore, the ΔE distributions are measured on data applying the reconstruction criteria, described in chapter 4. At the end of this section a summary of all results is shown.

The Monte Carlo model is fitted to the ΔE distributions for the reconstructed decay $B^0 \to D^-\pi^+$ and $B^0 \to D^{*-}\pi^+$, measured on the onpeak dataset.
The fit extracts the yields for the four components, especially the signal yields for the decay $B^0 \to D^{*-}\pi^+$. The ΔE spectra on data are shown in Fig. 6.1 together with the individual fit components. A summary of the signal yields $N_{D\pi}^{\pi^0}$ and $N_{D\pi}$ is quoted in Tab. 6.1 including the results from the fit to the ΔE distributions measured in Monte Carlo simulations. For the fit of the reconstructed decay $B^0 \to D^-\pi^+$ we obtain a large χ^2 value of $\chi^2 = 109$ (ndf=73) with a corresponding fit probability of $Prob_{\chi^2} = 0.4\%$. The origin of this large χ^2 value has not been completly identified but we suppose that our Monte Carlo model describes the data not very well, especially in the signal region. Compared to the fit of the reconstructed

Results on data				
	$N_{fit}^{sig} \pm \Delta N$	$\frac{N_{sig}}{p_{cut}^{\varepsilon}} \pm \Delta N$	χ^2/ndf	$Prob_{\chi^2}$
$B^0 \to D^- \pi^+$	4288 ± 255		109/73	0.4%
$B^0 \to D^{*-} \pi^+$	1949 ± 99	1995 ± 99	45/44	43%
$\varepsilon_{Data} = 1995/4288 = 46.5\%$				

Results on Monte Carlo simulations					
	$N_{fit}^{sig} \pm \Delta N$	$\frac{N_{sig}}{p_{cut}^{\varepsilon}} \pm \Delta N$	χ^2/ndf	$Prob_{\chi^2}$	N_{true}^{sig}
$B^0 \to D^- \pi^+$	4701 ± 253		65/73	74%	4549
$B^0 \to D^{*-} \pi^+$	2349 ± 90	2404 ± 90	50/44	25%	2288
$\varepsilon_{MC} = 2404/4701 = 51.1\%$ ($\varepsilon_{MC}^{true} = 50.3\%$)					

Table 6.1: Fit results for the signal yields $N_{D\pi}^{\pi^0}$ and $N_{D\pi}$ on data and Monte Carlo simulations including its fit uncertainties. We use them to calculate the absolute efficiencies. The signal yields in the decay $B^0 \to D^{*-}\pi^+$ are corrected by a factor $p_{cut}^{\varepsilon} = 0.977$ with respect to the limited fit range. In addition we quote the efficiency, the χ^2 value of the fit, the number of degrees of freedom (ndf) and the fit probability. For the fit on Monte Carlo simulations we quote also the number of true events N_{true} using *MC Truth information* and calculate the efficiency ε_{MC}^{true} with these numbers.

decay $B^0 \to D^-\pi^+$ we obtain a good χ^2 value of $\chi^2 = 45$ (ndf=44) in the fit of the reconstructed decay $B^0 \to D^{*-}\pi^+$. The corresponding fit probability is $Prob_{\chi^2} = 43\%$. The correlation matrices for the fit parameters of both fits, quoted in Tab. 6.2, show that the parameters are highly correlated (e.g. up to 97% for b and N_{norm}).
In our analysis we calculate the π^0 efficiency on data and on the Monte Carlo simulation according to Eq. 3.3. with respect to the limited fit range in the fit of the reconstructed decay $B^0 \to D^{*-}\pi^+$ as

$$\varepsilon(\pi^0) = \frac{N_{D\pi}^{\pi^0}/p_{cut}^{\varepsilon}}{N_{D\pi}}. \tag{6.1}$$

where p_{cut}^{ε} is the cut efficiency in the fit of the decay $B^0 \to D^{*-}\pi^+$.
The results of our analysis for the π^0 efficiency and the ratio between the efficiency on data and Monte Carlo simulations are

$$\begin{aligned} \varepsilon_{Data} &= (46.5 \pm 2.8_{stat} \pm 3.2_{sys})\% \\ \varepsilon_{MC} &= (51.1 \pm 2.8_{stat} \pm 3.4_{sys})\% \\ \frac{\varepsilon_{Data}}{\varepsilon_{MC}} &= (90.0 \pm 6.6_{stat} \pm 0.4_{sys})\% \end{aligned}$$

We discuss the statistical and systematic uncertainties and the procedure to determine the efficiency ratio in the next sections.

Decay $B^0 \to D^- \pi^+$					
	C_{sig}	$C_{pseudosig}$	C_{BBG}	N_{norm}	b
C_{sig}	1.000	-0.062	-0.721	0.487	-0.483
$C_{pseudosig}$	-0.062	1.000	0.167	-0.028	0.188
C_{BBG}	-0.721	0.167	1.000	-0.762	0.849
N_{norm}	0.487	-0.028	-0.762	1.000	-0.950
b	-0.483	0.188	0.849	-0.950	1.000

Decay $B^0 \to D^{*-} \pi^+$					
	C_{sig}	$C_{pseudosig}$	C_{BBG}	N_{norm}	b
C_{sig}	1.000	-0.075	-0.657	0.520	-0.451
$C_{pseudosig}$	-0.075	1.000	0.298	-0.159	0.216
C_{BBG}	-0.657	0.298	1.000	-0.840	0.867
N_{norm}	0.520	-0.159	-0.840	1.000	-0.973
b	-0.451	0.216	0.867	-0.973	1.000

Table 6.2: Parameter correlations in the fit of the reconstructed decay $B^0 \to D^- \pi^+$ and $B^0 \to D^{*-} \pi^+$ on data.

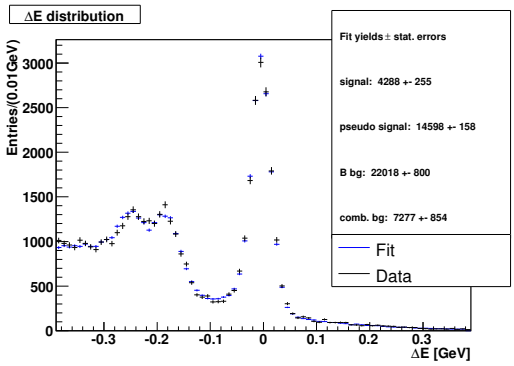

(a) Fit results for the reconstructed decay $B^0 \to D^-\pi^+$

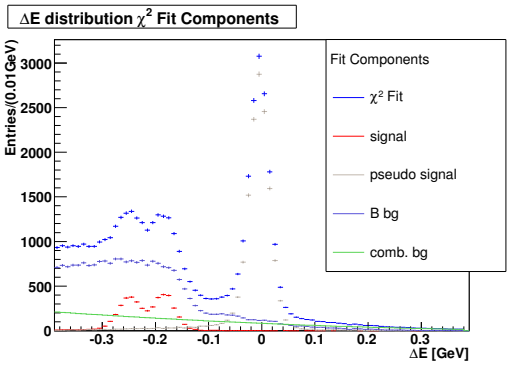

(b) Fit components for the reconstructed decay $B^0 \to D^-\pi^+$

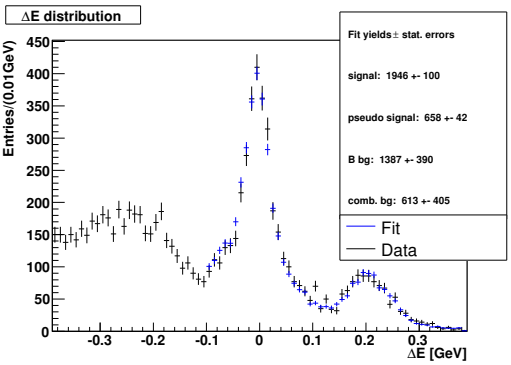

(c) Fit results for the reconstructed decay $B^0 \to D^{*-}\pi^+$

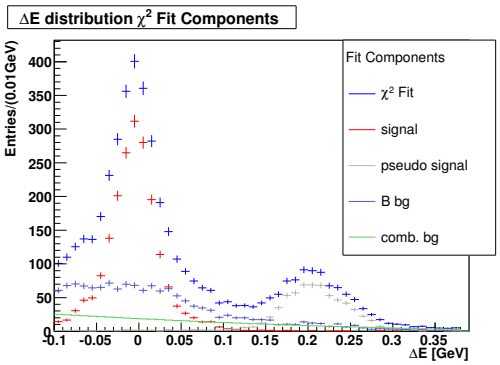

(d) Fit components for the reconstructed decay $B^0 \to D^{*-}\pi^+$

Figure 6.1: Fit results and components for the decay $B^0 \to D^-\pi^+$ and $B^0 \to D^{*-}\pi^+$ on data. Please note that from (c) to (d) the range on the x-axis has been changed.

	Data		Monte Carlo	
	$B^0 \to D^- \pi^+$	$B^0 \to D^{*-} \pi^+$	$B^0 \to D^- \pi^+$	$B^0 \to D^{*-} \pi^+$
$N_{fit}^{sig} \pm \Delta N$	4337 ± 231	1999 ± 87	4706 ± 226	2442 ± 71
χ^2/ndf	131/73	53/44	79/73	78/44

Table 6.3: Fit results for the signal yields on data and Monte Carlo simulations including its fit uncertainties. The uncertainties ΔN_{MC} of the Monte Carlo model are not taken into account. We use them to calculate the efficiency ratio $\frac{\varepsilon_{Data}}{\varepsilon_{MC}}$.

Cut Efficiency in the Decay $B^0 \to D^{*-} \pi^+$

As discussed in chapter 5.1.2, the ΔE fit range for the reconstruction of the decay $B^0 \to D^{*-} \pi^+$ has to be limited to $\Delta E \in [-0.1, 0.39]\,\mathrm{GeV}$. This leads to a reconstruction efficiency for real $B^0 \to D^{*-} \pi^+$ decays smaller than one. This fact has to be taken into account for the calculation of the π^0 efficiency by a factor $\frac{1}{p_{cut}^{\varepsilon}}$. The factor p_{cut}^{ε} is determined by using the ratio of the simulated signal events of the mixed Monte Carlo sample in the decay $B^0 \to D^{*-} \pi^+$ before (N_{sig}^{before}) and after (N_{sig}^{after}) the cut.

$$\begin{aligned} N_{sig}^{before} &= 2288 \\ N_{sig}^{after} &= 2235 \\ \Rightarrow p_{cut}^{\varepsilon} &= 97.7\% \end{aligned}$$

The factor p_{cut}^{ε} cancels out in the calculation of the ratio between the efficiency on data and Monte Carlo, but is important for the absolute π^0 efficiency on data and Monte Carlo simulations.

Determination of the Efficiency Ratio

Taking the uncertainties from the Monte Carlo model into account in the χ^2 minimization, described in Eq. 5.6, leads to correlations between the fitted parameters on data and on Monte Carlo simulations. This fact is especially important for the calculation of the ratio $\frac{\varepsilon_{Data}}{\varepsilon_{MC}}$. To circumvent this correlation, we repeat the fit without the uncertainties ΔN_{MC} and use these results for the calculation of the ratio $\frac{\varepsilon_{Data}}{\varepsilon_{MC}}$, as they are considered to be uncorrelated. We obtain the signal yields, quoted in Tab. 6.3, and a efficiency ratio of $\frac{\varepsilon_{Data}}{\varepsilon_{MC}} = 90.0\%$.

6.2 Statistical Uncertainties

To determine the statistical uncertainty on the absolute efficiencies and the efficiency ratio between data and Monte Carlo simulations correctly, the correlation between signal and background events in both fits has to be taken into account. An appropriate method, based on a recipe from [30], is derived by reformulating the problem.

To clarify the method, we repeat our definition for the variables $N_{D\pi}$ and $N_{D\pi}^{\pi^0}$ as described in chapter 3 and introduce a new variable N_X.

$N_{D\pi}$**:** is the number of decays $B^0 \to D^{*-}\pi^+$ which are reconstructed as $B^0 \to D^-\pi^+$ where the π^0 is not required for the reconstruction.

$N_{D\pi}^{\pi^0}$**:** is the number of decays $B^0 \to D^{*-}\pi^+$ where the π^0 is required for the reconstruction of the decay $B^0 \to D^{*-}\pi^+$. These events are included in the number of events $N_{D\pi}$.

N_X**:** is the number of decays $B^0 \to D^{*-}\pi^+$ reconstructed as $B^0 \to D^-\pi^+$, but which do not include the number of events $N_{D\pi}^{\pi^0}$.

To evaluate the statistical uncertainty on the efficiency, we use the fact $N_{D\pi}^{\pi^0}$ and N_X are uncorrelated. Although N_X is not measured directly it can be predicted from the measured numbers $N_{D\pi}$ and $N_{D\pi}^{\pi^0}$, using $N_{D\pi} = N_{D\pi}^{\pi^0} + N_X$. Thus, the efficiency calculates

$$\varepsilon(\pi^0) = \frac{N_{D\pi}^{\pi^0}}{N_{D\pi}} = \frac{N_{D\pi}^{\pi^0}}{N_{D\pi}^{\pi^0} + N_X}$$

The uncertainty on the efficiency can be computed by using simple error propagation because $N_{D\pi}^{\pi^0}$ and N_X are uncorrelated and is given by the following expression.

$$\Delta\varepsilon = \sqrt{\left(\frac{\partial\varepsilon}{\partial N_{D\pi}^{\pi^0}}\right)^2 \cdot (\Delta N_{D\pi}^{\pi^0})^2 + \left(\frac{\partial\varepsilon}{\partial N_X}\right)^2 \cdot (\Delta N_X)^2}$$

By evaluating the partial derivatives

$$\frac{\partial\varepsilon}{\partial N_{D\pi}^{\pi^0}} = \frac{N_X}{(N_X + N_{D\pi}^{\pi^0})^2} \qquad \textit{and} \qquad \frac{\partial\varepsilon}{\partial N_X} = \frac{-N_{D\pi}^{\pi^0}}{(N_X + N_{D\pi}^{\pi^0})^2}$$

the error $\Delta\varepsilon$ can be written as

$$\Delta\varepsilon = \sqrt{\left(\frac{N_X \cdot \Delta N_{D\pi}^{\pi^0}}{(N_X + N_{D\pi}^{\pi^0})^2}\right)^2 + \left(\frac{N_{D\pi}^{\pi^0} \cdot \Delta N_X}{(N_X + N_{D\pi}^{\pi^0})^2}\right)^2}$$

Proceeding from the relation $N_{D\pi} = N_{D\pi}^{\pi^0} + N_X$, the equation for the errors $(\Delta N_{D\pi})^2 = (\Delta N_{D\pi}^{\pi^0})^2 + (\Delta N_X)^2$ should be valid as well. After eliminating the unmeasured quantities N_X and ΔN_X we obtain the following formula

$$\Delta\varepsilon = \sqrt{\left(\frac{\varepsilon \cdot \Delta N_{D\pi}}{N_{D\pi}}\right)^2 + (1 - 2 \cdot \varepsilon)\left(\frac{\Delta N_{D\pi}^{\pi^0}}{N_{D\pi}}\right)^2} \tag{6.2}$$

The statistical error on the absolute efficiencies and on the efficiency ratio is calculated according to this formula 6.2. For the absolute efficiencies the statistical

	σ_{stat}	$\frac{\sigma_{stat}}{\varepsilon}$
Data	0.028	6.2 %
Monte Carlo	0.026	5.4 %

Table 6.4: Statistical uncertainties for the absolute efficiencies on data and Monte Carlo simulations. The errors are calculated according to the signal yields from Tab. 6.1.

	σ_{stat}	$\frac{\sigma_{stat}}{\varepsilon}$
Data	0.025	5.5 %
Monte Carlo	0.024	4.8 %

Table 6.5: Statistical uncertainties for the efficiency ratio $\frac{\varepsilon_{Data}}{\varepsilon_{MC}}$ on data and Monte Carlo simulations. The errors are calculated according to the signal yields from Tab. 6.3.

uncertainties are summarized in Tab. 6.4 and for the efficiency ratio $\frac{\varepsilon_{Data}}{\varepsilon_{MC}}$ they are quoted in Tab. 6.5.

6.3 Systematic Uncertainties

The systematic uncertainties which arise in the presented analysis are discussed in this section.

We assume that for the determination of the π^0 efficiency according to Eq. 3.3 the $\pi^{\pm}$ and kaon efficiencies cancel in good approximation.
The background from B decays is considered as the main source of systematic uncertainties. By identifying the single contributing decays it turns out that in most cases large uncertainties are assigned to the branching fractions. Besides, we observe a strong anti-correlation between signal and B background of 72% in the fit of the decay $B^0 \to D^-\pi^+$ and of 66% in the fit of the decay $B^0 \to D^{*-}\pi^+$, as quoted in the correlation matrices in Tab. 6.2. According to these observations the branching fractions of the 13 main B background decays are varied within the uncertainties, given in [6], to determine the systematic uncertainties. Technically this is implemented by reweighing the events. A complete list of these decays is quoted in Tab.6.6.
The variation is done simultaneously for both reconstructed decays, $B^0 \to D^-\pi^+$ and $B^0 \to D^{*-}\pi^+$, and is performed a hundred times. During this procedure a random number x is picked out of a gaussian distribution with mean $\mu = 0$ and a standard deviation $\sigma = 1$. With that number a new branching fraction $\mathcal{B}_{new}$ is calculated using the error $\sigma_{\mathcal{B}}$ on the branching fraction $\mathcal{B}$ from [6].

$$\mathcal{B}^i_{new} = \mathcal{B}^i + x^i\sigma^i_{\mathcal{B}} \qquad with \qquad i = 1 \ldots 13$$

All 13 decays are varied simultaneously but with different x. A summary of the branching fractions and the errors on the branching fractions is also quoted in Tab.6.6.

Decay	$\mathcal{B}_{gen.MC}$	$\mathcal{B}_{PDG}$	$\frac{\mathcal{B}_{gen.MC}}{\mathcal{B}_{PDG}}$
$B^+ \to \pi^+(K\pi\pi^0)_{\bar{D^0}}$	$(4.60) \cdot 10^{-3}$	$(4.92 \pm 0.20) \cdot 10^{-3}$	1.07
$B^+ \to (\pi^+\pi^0)_{\rho^+} D^0$	$(1.34) \cdot 10^{-2}$	$(1.34 \pm 0.18) \cdot 10^{-2}$	1.00
$B^0 \to \pi^+\pi^0(D^-\pi^0)_{D^{*-}}$	$(6.80) \cdot 10^{-3}$	$(6.80 \pm 0.90) \cdot 10^{-3}$	1.00
$B^+ \to \mu^+\nu_\mu D$	$(2.24) \cdot 10^{-2}$	$(2.12 \pm 0.20) \cdot 10^{-2}$	0.96
$B^+ \to \pi^+\pi^+ D^-$	$(1.02) \cdot 10^{-3}$	$(1.02 \pm 0.16) \cdot 10^{-3}$	1.00
$B^0 \to \pi^+(D^0\pi^-)_{D^{*-}}$	$(2.80) \cdot 10^{-3}$	$(2.76 \pm 0.21) \cdot 10^{-3}$	0.99
$B^+ \to \pi^+(D^0\pi^0)_{\bar{D^{*0}}}$	$(4.60) \cdot 10^{-3}$	$(4.60 \pm 0.40) \cdot 10^{-3}$	1.00
$B^0 \to (\pi^+\pi^0)_{\rho^+} D^-$	$(7.70) \cdot 10^{-3}$	$(7.50 \pm 1.20) \cdot 10^{-3}$	0.97
$B^0 \to a_1^+(1260) D^-$	$(8.34) \cdot 10^{-3}$	$(6.00 \pm 3.30) \cdot 10^{-3}$	0.72
$B^+ \to (\pi^+\pi^0)_{\rho^+}(D^0\pi^0)_{\bar{D^{*0}}}$	$(9.80) \cdot 10^{-3}$	$(9.80 \pm 1.70) \cdot 10^{-3}$	1.00
$B^0 \to (\pi^+\pi^0)_{\rho^+}(D^0\pi^-)_{D^{*-}}$	$(6.80) \cdot 10^{-3}$	$(6.80 \pm 0.90) \cdot 10^{-3}$	1.00
$B^+ \to \pi^+\bar{D^0}$	$(5.00) \cdot 10^{-3}$	$(4.92 \pm 0.20) \cdot 10^{-3}$	0.98
$B^+ \to \pi^+(D^0\gamma)_{\bar{D^{*0}}}$	$(4.60) \cdot 10^{-3}$	$(4.60 \pm 0.40) \cdot 10^{-3}$	1.00

Table 6.6: Branching fractions and errors on the main B background decays. Additionally the branching fractions as they are used in the generic Monte Carlo simulations are compared to the nominal values from the PDG [6].

Afterwards the fit is repeated on data and on the Monte Carlo simulation and the determined absolute efficiency is filled in a histogram. The resulting distributions are shown in Fig. 6.2.
We take the root mean square (RMS) of these distributions as estimate for the systematic uncertainty.

$$\sigma^{Data}_{Bdecays} = 0.032 \quad \Rightarrow \quad \frac{\sigma^{Data}_{Bdecays}}{\varepsilon_{Data}} = 7\%$$

$$\sigma^{MC}_{Bdecays} = 0.034 \quad \Rightarrow \quad \frac{\sigma^{MC}_{Bdecays}}{\varepsilon_{MC}} = 6.7\%$$

Subsequent to this general analysis a more detailed study of those B decays, contributing most to the systematic uncertainty, is performed.
Decays with large branching fractions compared to the other and a ΔE distribution similar to signal or leaking into the ΔE signal region are selected and are listed below.

1. $B^0 \to \pi^+\pi^0 D^-$
2. $B^0 \to \pi^+\pi^0 D^{*-}, D^{*-} \to D^-\pi^0$
3. $B^+ \to \pi^+\pi^+ D^-$

Then, the whole variation procedure described before is repeated for every selected decay separately. This means only one branching fraction is varied according to a

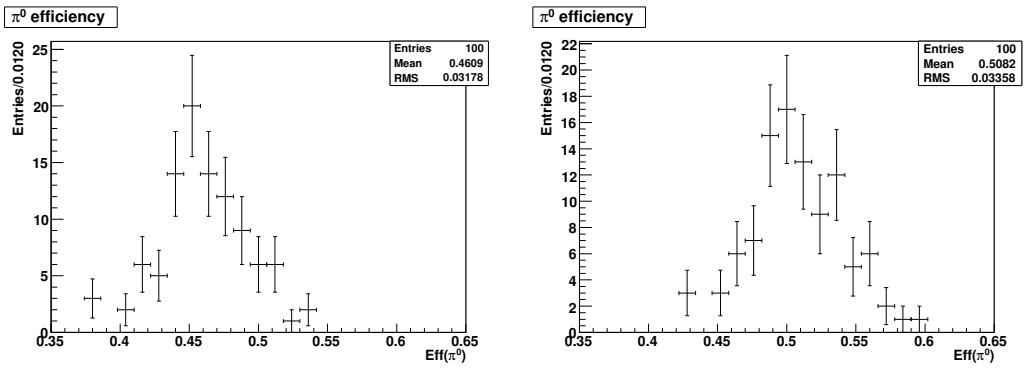

(a) Absolute efficiency on data

(b) Absolute efficiency on Monte Carlo simulations

Figure 6.2: Results of the study of systematic uncertainties from B background decays on data and Monte Carlo simulations. The distributions of the absolute efficiencies obtained during the variation procedure are shown.

gaussian distribution while keeping the other ones constant. The resulting distributions of the absolute efficiencies in data and Monte Carlo simulations are shown in Fig. 6.3.
The decay $B^0 \to \pi^+\pi^0 D^-$ is identified as main source of the systematic uncertainty from B background decays. We obtain a RMS from the efficiency distribution on data of $\sigma^{Data}_{B^0\to\pi^+\pi^0 D^-} = 0.025$ and on the Monte Carlo simulations a RMS of $\sigma^{MC}_{B^0\to\pi^+\pi^0 D^-} = 0.027$.

Systematic Error on the Efficiency Ratio $\frac{\varepsilon_{Data}}{\varepsilon_{MC}}$

To determine the systematic uncertainty from B background decays on the efficiency ratio $\frac{\varepsilon_{Data}}{\varepsilon_{MC}}$, we have repeated the whole variation procedure of the 13 main B background decays but without taking the uncertainties ΔN_{MC} from the Monte Carlo model into account. During this procedure the efficiency ratio $\frac{\varepsilon_{Data}}{\varepsilon_{MC}}$ is calculated every time with the determined efficiency on data and Monte Carlo simulations and is filled into a histogram. The resulting distribution for the efficiency ratio $\frac{\varepsilon_{Data}}{\varepsilon_{MC}}$ is shown in Fig. 6.4.
We find that the systematic uncertainties from B background decays do not cancel completely in the efficiency ratio between data and Monte Carlo simulations. Thus, we take the RMS of the distribution, shown in Fig. 6.4, as estimate for the systematic uncertainty on the efficiency ratio $\frac{\varepsilon_{Data}}{\varepsilon_{MC}}$.

$$\sigma_{ratio} = \quad 0.004 \qquad \Rightarrow \qquad \frac{\sigma_{ratio}}{\frac{\varepsilon_{Data}}{\varepsilon_{MC}}} = 0.5\%$$

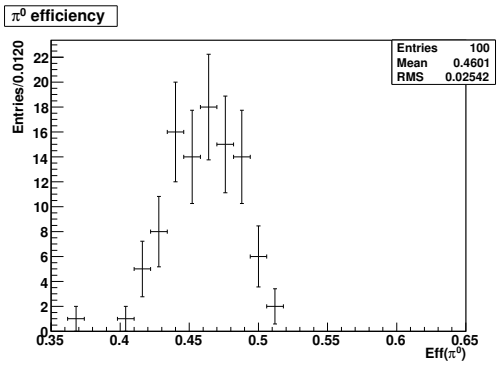

(a) Varied decay: $B^0 \to \pi^+\pi^0 D^-$

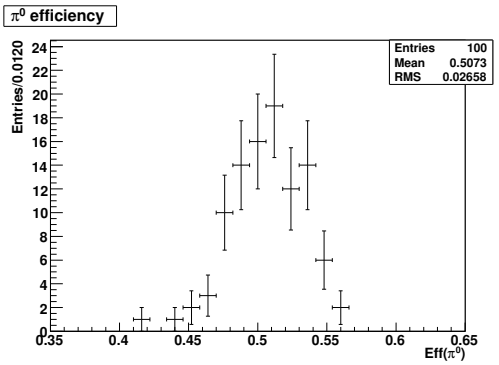

(b) Varied decay: $B^0 \to \pi^+\pi^0 D^-$

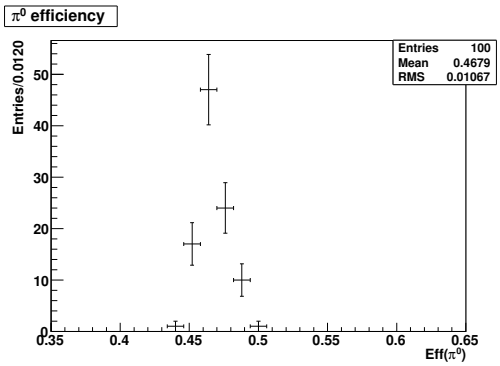

(c) Varied decay: $B^0 \to \pi^+\pi^0 D^{*-}$

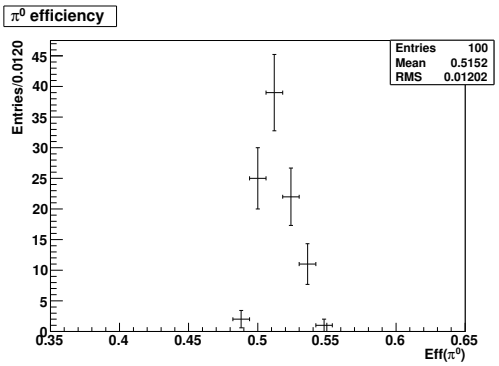

(d) Varied decay: $B^0 \to \pi^+\pi^0 D^{*-}$

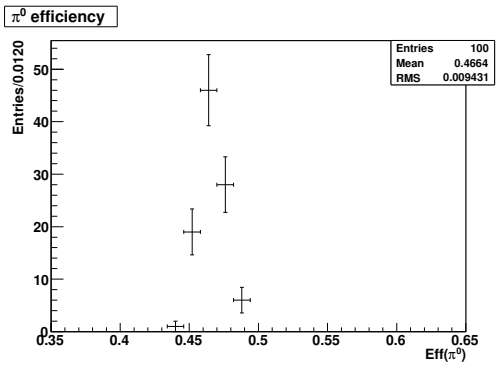

(e) Varied decay: $B^+ \to \pi^+\pi^+ D^-$

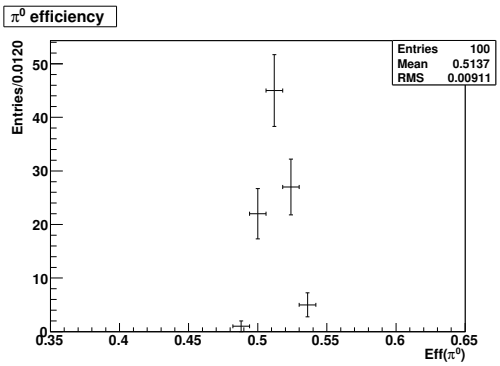

(f) Varied decay: $B^+ \to \pi^+\pi^+ D^-$

Figure 6.3: Detailed study of systematic uncertainties from certain B background decays. The distributions of the absolute efficiencies obtained during the variation procedure are shown. The left plots show the results on data and the right one the results on Monte Carlo simulations.

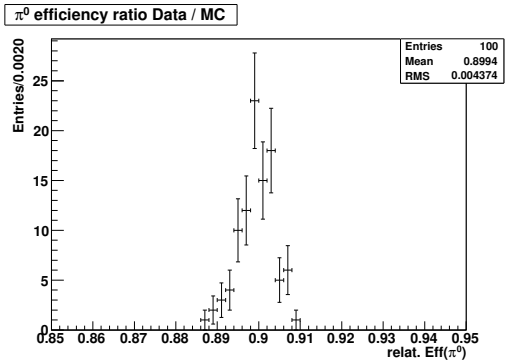

Figure 6.4: Distribution of the efficiency ratio $\frac{\varepsilon_{Data}}{\varepsilon_{MC}}$ in the study of systematic uncertainties from B background decays.

Systematic Error on the Cut Efficiency p^{ε}_{cut}

A small systematic uncertainty in the fit of the decay $B^0 \to D^{*-}\pi^+$ arises from the cut efficiency p^{ε}_{cut}. This efficiency has an uncertainty due to the limited statistics of the Monte Carlo sample. With the uncertainties $\Delta N^{before}_{sig} = \sqrt{N^{before}_{sig}}$ and $\Delta N^{after}_{sig} = \sqrt{N^{after}_{sig}}$, the expected error from Binomial statistics on the cut efficiency is calculated as follows.

$$\begin{aligned} \Delta p^{\varepsilon}_{cut} &= \sqrt{\frac{p^{\varepsilon}_{cut}(1-p^{\varepsilon}_{cut})}{N^{before}_{sig}}} \\ &= 0.003 \end{aligned}$$

The resulting systematic error on the cut efficiency p^{ε}_{cut} is negligible and therefore it is not considered in the systematic uncertainty on the π^0 efficiency.

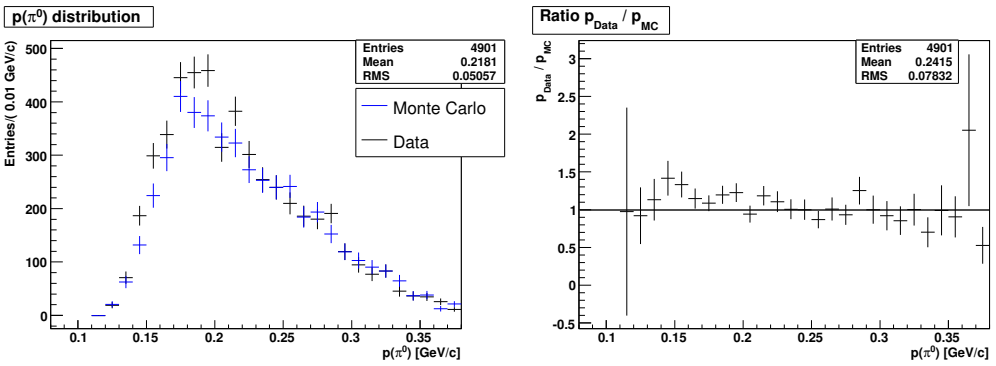

Figure 6.5: The reconstructed π^0 momentum distribution of the signal events in data and Monte Carlo simulations for the decay $B^0 \to D^{*-}\pi^+$(left). The plot on the right shows the ratio between data and Monte Carlo simulations.

6.4 Comparisons with Previous Measurements

To compare our results with existing studies, we measure the average momentum of the π^0 meson in the laboratory frame for signal events in the decay $B^0 \to D^{*-}\pi^+$. Therefore, the measured π^0 momentum spectra for the three background components are scaled with the fractions derived from the fit and subtracted from the total measured π^0 momentum spectrum in data or Monte Carlo simulations respectively. The resulting π^0 momentum distribution of the signal events is shown in Fig. 6.5. The ratio between data and Monte Carlo simulations is flat and compatible with one. Thus, a common average value for the reconstructed momentum $\overline{p}_{\pi^0}$ and a reconstructed momentum range of the π^0 meson can be specified.

$$0.11\,\mathrm{GeV}/c < p_{\pi^0} < 0.38\,\mathrm{GeV}/c$$
$$\overline{p}_{\pi^0} = 0.22\,\mathrm{GeV}/c$$

We compare our results with the ratio of the π^0 reconstruction efficiency of the *BABAR* detector between data and Monte Carlo simulations, derived in the τ analysis, for the π^0 selector list *pi0DefaultMass*. In Fig. 6.6 the π^0 efficiency ratio of the *BABAR* detector is shown as a function of the π^0 momentum.

We find that our result for the relative ratio $\frac{\varepsilon_{Data}}{\varepsilon_{MC}}$ of the π^0 efficiency of the *BABAR* detector between data and simulated events is compatible with the result of the τ analysis within the errors.
A comparison with the measurement using D^0 meson decays is not possible due to the different π^0 selector lists.

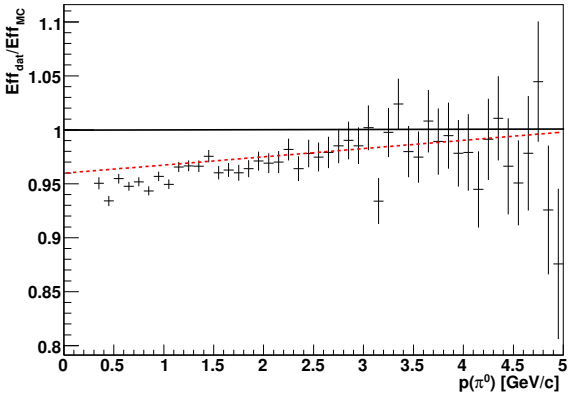

Figure 6.6: Resulting plot from the τ analysis for the ratio of the π^0 efficiency of the *BABAR* detector in data and Monte Carlo simulations. The dashed line corresponds to the linear efficiency correction for the used π^0 list (*pi0DefaultMass*). Only statistical errors are plotted.

Chapter 7

Outlook

In this chapter we give a short outlook about all open tasks in our analysis and include suggestions and techniques to improve our method.

The following aspects concerning the statistical and systematic error treatment still need to be verified.

- The dependence of the signal yields on the shift in ΔE between data and Monte Carlo simulations has to be studied.
- To find the best value for the shift in ΔE between data and Monte Carlo simulations, this value could be added to the fit procedure as a free parameter. Technically, this could be implemented by generating a large set of ΔE distributions with different shifts in ΔE. While fitting the ΔE spectrum, the histogram with the optimal shift in ΔE is selected.
- It has to be verified that the formula for the calculation of the statistical uncertainties, described in Eq. 6.2, yields an appropriate estimate for the efficiency. Therefore, Toy Monte Carlo studies have to be performed, based on Monte Carlo histograms for signal and backgrounds for the decay $B^0 \to D^-\pi^+$ and $B^0 \to D^{*-}\pi^+$.
- We have identified the decay $B^0 \to \pi^+\pi^0 D^-$ as main source of the systematic uncertainty from B background decays. A veto on the reconstruction of this decay would reduce the systematic and statistical error significantly.
- The large uncertainty on the signal yield arises mostly from the parametrization of the combinatorial background with a polynomial with a free shape in the fit. The errors on the signal yield could be reduced fixing the shape of the combinatorial background on data by using the m_{ES} sideband.

Chapter 8

Conclusion

The presented analysis has determined the efficiency for the reconstruction of low energy π^0 mesons with the *BABAR* detector on a dataset corresponding to a luminosity of $190.45\,\mathrm{fb}^{-1}$.

We have performed our study in a dedicated B decay environment with low energy π^0 mesons using the decay channel $B^0 \to D^{*-}\pi^+$ with $D^{*-} \to D^-\pi^0$ ($D^- \to K^+\pi^-\pi^-$). On the one hand we reconstruct this decay $B^0 \to D^{*-}\pi^+$ without requiring the π^0 meson for the reconstruction as $B^0 \to D^-\pi^+$. They generate a characteristic bump in the spectrum of the variable $\Delta E = E^*_B - E^*_{beam}$, defined in the e^+e^- center-of-momentum frame, at negative values. The "*" denotes that the variables are also defined in the e^+e^- center-of-momentum frame. On the other hand we require the reconstruction of the π^0 meson for the reconstruction of the decay $B^0 \to D^{*-}\pi^+$. These decays peak in the ΔE spectrum of the reconstructed decay $B^0 \to D^{*-}\pi^+$ at $\Delta E = 0$. In both cases we perform a binned χ^2 fit to the measured ΔE distributions for the reconstructed decay $B^0 \to D^-\pi^+$ and $B^0 \to D^{*-}\pi^+$ in order to extract the number of events $B^0 \to D^{*-}\pi^+$ which are reconstructed as $B^0 \to D^-\pi^+$ or as $B^0 \to D^{*-}\pi^+$. The π^0 efficiency of the *BABAR* detector is determined using the ratio between the events where the π^0 is required for the reconstruction of the B meson decay to the number of events where the π^0 is not required for the reconstruction.
To suppress backgrounds, several selection criteria are used. In particular a neural net, combining several discriminating variables, is trained and applied. The fit has been validated and tested successfully on Monte Carlo simulations.

For an average reconstructed momentum of the π^0 meson of $\overline{p}_{\pi^0} = 0.22\,\mathrm{GeV}/c$ in the laboratory frame, we measure a relative ratio of the π^0 efficiency of the *BABAR* detector between data and simulated events of $\frac{\varepsilon_{Data}}{\varepsilon_{MC}} = (90.0 \pm 6.6_{stat} \pm 0.4_{sys})\%$. The result of our analysis is consistent with previous measurements within the errors.

Further improvements of our study are possible and described in chapter 7.

Appendix A

Origin of the Double Peak Structure

In this appendix we explain the double peak structure in the ΔE spectrum of the reconstructed decay $B^0 \to D^- \pi^+$ from events $B^0 \to D^{*-} \pi^+$ with $D^{*-} \to D^- \pi^0$, as shown in Fig. 4.1. First, the decay and the properties of the involved particles are examined. The D^{*-} meson consists of a d and a $\bar{c}$ quark which form a spin triplet with an angular momentum $j = 1$. Therefore, it belongs to the vector mesons. The D^- and the π^0 are pseudoscalar mesons with $j = 0$. A summary of the particle properties in the final and initial state is quoted in Tab. A.1. The decay of the D^{*-} meson is mediated by the isospin conserving strong interaction and the corresponding Feynman-Graph is shown in Fig. A.1.

To understand the double peak structure, the quantum mechanical state $\big|\psi\big\rangle = \big|jm\big\rangle$ is regarded, where j and m are eigenstates of the angular momentum operator J^2 and the third component of the angular momentum operator J_3. Both operators commute and consequently they share a complete set of eigenvectors. First we study the mathematical formalism when a state $\big|\psi\big\rangle$ is rotated by an angle ϕ about one axis. There, the state $\big|jm\big\rangle$ is transformed by the operator D into a state $\overline{\big|\psi\big\rangle} = D\big|\psi\big\rangle$ which is a linear combination of the $2j+1$ states $\big|jm'\big\rangle$ with $m' = -j, -j+1, \ldots, j$.

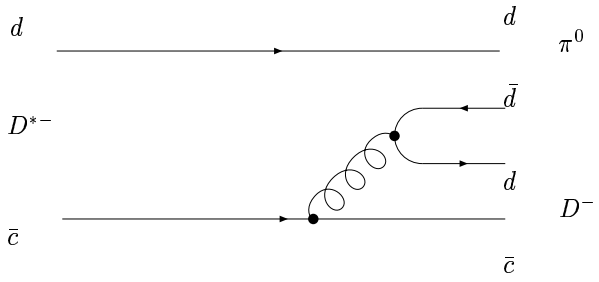

Figure A.1: Feynman-Graph for the decay $D^{*-} \to D^- \pi^0$

	Spin s	(J^P)	I	I_3	$q\bar{q}$
D^{*-}	1	1^-	1/2	-1/2	$d\bar{c}$
D^-	0	0^-	1/2	-1/2	$d\bar{c}$
π^0	0	0^-	1	0	$\frac{1}{\sqrt{2}}(d\bar{d} - u\bar{u})$

Table A.1: Particle properties of the decay $B^0 \to D^{*-}\pi^+$

The physics is unchanged by this operation which means that the operator D has to be unitary.

$$\langle\overline{\psi}|\overline{\psi}\rangle = \langle\psi|\psi\rangle \;\rightarrow\; D^\dagger = D^{-1}$$

As shown in [31, 32], a rotation by the angle ϕ about the 2-axis is generated by the hermitian rotation operator

$$D = \exp(\imath J_2 \phi) \tag{A.1}$$

where J_2 is the second component of the angular momentum operator J.
The resulting formula for rotating a state $|\psi\rangle = |jm\rangle$ by the angle ϕ about the 2-axis is given by

$$\exp(-\imath\phi J_2)|jm\rangle = \sum_{m'} d^j_{m'm}(\phi)|jm'\rangle \tag{A.2}$$

The coefficients $d^j_{m'm}(\phi)$ are denoted as rotation matrices and are tabulated in [6]. The elements of the matrix can be evaluated as the following.

$$d^j_{m'm}(\phi) = \langle jm'|\exp(-\imath\phi J_2)|jm\rangle \tag{A.3}$$

This calculus is used to explain the double peak structure in the ΔE spectrum of the reconstructed decay $B^0 \to D^-\pi^+$. If the decay $D^{*-} \to D^-\pi^0$ is considered in the D^{*-} meson rest frame, the initial state is given by $|\psi\rangle_i = |j = 1, m = 0\rangle$. For conservation of angular momentum reasons the D^- meson and the π^0 meson must have an angular momentum $l = 1$, which means $j = l + s = 1$. Thus, the final state can be written as $|\psi\rangle_f = |j = 1, m = 0\rangle$ too. In addition the 2-axis is identified with the direction of flight of the D^{*-} meson in the $\Upsilon(4S)$ rest frame and the angle ϕ is substituted by the helicity angle θ^*_{hel}.

helicity angle θ^*_{hel}: The helicity angle θ^*_{hel} is defined in the center-of-momentum frame of the D^{*-} meson as the angle of emission of the π^0 and the direction of flight of the D^{*-} meson in the $\Upsilon(4S)$ rest frame.

The resulting formula

$$d^1_{00}(\theta^*_{hel}) = \langle 10|\exp(-\imath\theta^*_{hel}J_2)|10\rangle \tag{A.4}$$

can be evaluated by expanding the exponential term

$$\exp(-\imath\theta^*_{hel}J_2) = 1 - \imath\theta^*_{hel}J_2 - \frac{\theta^{*2}_{hel}}{2!}J_2^2 + \ldots \tag{A.5}$$

and using the definition of the step operators.

$$\begin{aligned} J_+ &= J_1 + \imath J_2 \\ J_- &= J_1 - \imath J_2 \\ \Rightarrow J_2 &= -\frac{\imath}{2}(J_+ - J_-) \end{aligned} \tag{A.6}$$

The computation of the expression

$$J_2\big|10\big\rangle = -\frac{\imath}{2}(J_+ - J_-)\big|10\big\rangle$$

with the step operator formalism

$$\begin{aligned} J_+\big|10\big\rangle = &\quad \sqrt{1(1+1)-0}\big|11\big\rangle \\ J_-\big|10\big\rangle = &\quad \sqrt{1(1+1)-0}\big|1-1\big\rangle \end{aligned}$$

gives the following result.

$$\Rightarrow J_2\big|10\big\rangle = J_2^{2k+1}\big|10\big\rangle = -\frac{\imath}{\sqrt{2}}(\big|11\big\rangle - \big|1-1\big\rangle) \qquad k \in \mathbb{N} \tag{A.7}$$

On the other hand, evaluating

$$J_2^2\big|10\big\rangle = -\frac{\imath}{\sqrt{2}}(J_2\big|11\big\rangle - J_2\big|1-1\big\rangle)$$

results in this final expression.

$$\Rightarrow J_2^2\big|10\big\rangle = J_2^{2k}\big|10\big\rangle = \big|10\big\rangle \qquad k \in \mathbb{N} \tag{A.8}$$

With this algebra and the expansion of the exponential function, the matrix element $d^1_{00}(\theta^*_{hel})$ can be computed.

$$\begin{aligned} \big\langle 10\big|\exp\left(-\imath\theta^*_{hel}J_2\right)\big|10\big\rangle = &\quad 1 - \imath\theta^*_{hel}\big\langle 10\big|J_2\big|10\big\rangle + \imath\tfrac{\theta^{*3}_{hel}}{3!}\big\langle 10\big|J_2^3\big|10\big\rangle + \ldots \\ = &\quad 1 \end{aligned} \tag{A.9}$$

In addition the orthogonality relation for the states $\big|jm\big\rangle$ is used.

$$\begin{aligned} \big\langle 10\big|\exp\left(-\imath\theta^*_{hel}J_2\right)\big|10\big\rangle = &\quad -\tfrac{\theta^{*2}_{hel}}{2!}\big\langle 10\big|J_2^2\big|10\big\rangle + \tfrac{\theta^{*4}_{hel}}{4!}\big\langle 10\big|J_2^4\big|10\big\rangle + \ldots \\ = &\quad -\tfrac{1}{2!}\theta^{*2}_{hel} + \tfrac{1}{4!}\theta^{*4}_{hel} + \ldots \end{aligned} \tag{A.10}$$

The resulting identity represents the Taylor series of the cosine. Thus, the rotation matrix can be written as

$$d^1_{00}(\theta^*_{hel}) = \cos\theta^*_{hel} \tag{A.11}$$

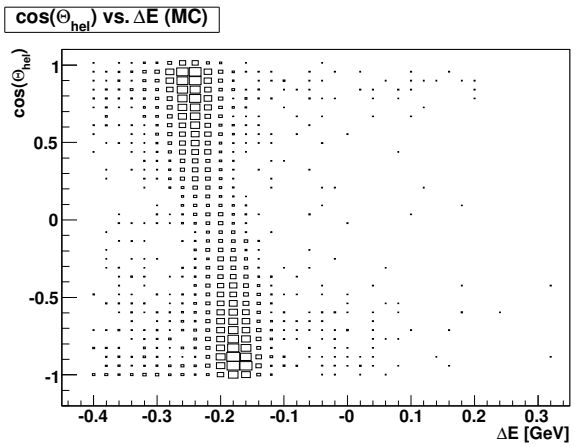

Figure A.2: $\cos\theta^*_{hel}$ versus ΔE distribution for the π^0 meson. The generated decay $B^0 \to D^{*-}\pi^+$ is reconstructed as $B^0 \to D^-\pi^+$ using $B\overline{B}$ Monte Carlo without applying any cuts.

and hence the predicted angular distribution reads as follows.

$$|d^1_{00}(\theta^*_{hel})|^2 = \cos^2\theta^*_{hel} \tag{A.12}$$

Fig. A.2 shows that this expectation matches the simulation very well. The π^0 is emitted preferably in or against the direction of flight of the D^{*-}, which causes a slight difference in energy and generates the double peak structure in the ΔE spectrum of the reconstructed decay $B^0 \to D^-\pi^+$.

Appendix B

List of B and D Meson Decay Modes

In this appendix we quote a list of the B and D meson decay modes which are necessary to calculate the decay mode number, assigned to a B meson decay. In addition the technical implementation of the decay $B^0 \to D^{*-}\pi^+$ is explained.

For our analysis we have produced an own skim, denoted as *modified BSemiExcl* skim, which selects 14 different B decays, summarized in Tab. B.1. The B decays are written using a specific notation. For example, the representation $B^0 \to \pi^+(K\pi\pi)_{D^-}$ stands for the decay $B^0 \to \pi^+ D^-$ with $D^- \to K\pi\pi$.

Technical Implementation of the Decay $B^0 \to D^{*-}\pi^+$

This paragraph explains briefly, why there are two different decay mode numbers assigned to the decay $B^0 \to D^{*-}\pi^+$ with $D^{*-} \to D^-\pi^0$, quoted in Tab. B.1. During the reconstruction on `Beta` level, the decay $B^0 \to D^{*-}\pi^+$ is selected by means of the difference of the invariant masses ΔM between the combination of the particles $(K\pi\pi)\pi^0$ and $(K\pi\pi)$.

$$\Delta M = |m_{(K\pi\pi)\pi^0} - m_{K\pi\pi}|$$

The decay is added to the skim if ΔM is in the range $0.1366\,\mathrm{GeV}/c^2 < \Delta M < 0.1446\,\mathrm{GeV}/c^2$. In that case the decay mode number 12131 is assigned.
The decay $B^0 \to D^{*-}\pi^+$ is additionally selected if $\Delta M < 0.16\,\mathrm{GeV}/c^2$ and the decay mode number 12103 is assigned. All decays which are already assigned to the mode number 12131 are excluded there. This means that technically both decay mode numbers has to be used for the reconstruction in order to cover the complete $\Delta M < 0.16\,\mathrm{GeV}/c^2$ range, which is illustrated in Fig. B.1.

Decay	Decay Mode number
$B^0 \to \pi^+(K\pi\pi)_{D^-}$	12101
$B^+ \to \pi^+(K\pi)_{D^0}$	11001
$B^0 \to \pi^+[(K\pi)_{D^0}\pi^-]_{D^{*-}}$	13001
$B^+ \to \pi^+[(K\pi)_{D^0}\pi^0]_{D^{*0}}$	14001
$B^0 \to \pi^+[(K\pi\pi^0)_{D^0}\pi^-]_{D^{*-}}$	13101
$B^+ \to \pi^+[(K\pi\pi^0)_{D^0}\pi^0]_{D^{*0}}$	14101
$B^0 \to \pi^+[(K\pi\pi)_{D^-}\pi^0]_{D^{*-}}$	12103,12131
$B^0 \to \pi^+\pi^0[(K\pi)_{D^0}\pi^-]_{D^{*-}}$	13003
$B^+ \to \pi^+\pi^0[(K\pi)_{D^0}\pi^0]_{D^{*0}}$	14003
$B^+ \to \pi^+\pi^-\pi^+[(K\pi)_{D^0}\pi^0]_{D^{*0}}$	14009
$B^0 \to \pi^+\pi^-\pi^+[(K\pi)_{D^0}\pi^-]_{D^{*-}}$	13009
$B^0 \to \pi^+[(K\pi\pi\pi)_{D^0}\pi^-]_{D^{*-}}$	13201
$B^+ \to \pi^+[(K\pi\pi\pi)_{D^0}\pi^0]_{D^{*0}}$	14201

Table B.1: Decay modes selected by our *modified BSemiExcl* skim

D mode	Decay	D mode	Decay
110	$D^0 \to K\pi$	140	$D^{*0} \to D^0\pi^0, D^0 \to K\pi$
111	$D^0 \to K\pi\pi^0$	141	$D^{*0} \to D^0\pi^0, D^0 \to K\pi\pi^0$
112	$D^0 \to K\pi\pi\pi$	142	$D^{*0} \to D^0\pi^0, D^0 \to K\pi\pi\pi$
113	$D^0 \to K_s\pi$	143	$D^{*0} \to D^0\pi^0, D^0 \to K_s\pi\pi$
115	$D^0 \to \ell X$	145	$D^{*0} \to D^0\pi^0, D^0 \to \ell X$
120	$D^\pm \to K_s\pi$	150	$D^{*0} \to D^0\gamma, D^0 \to K\pi$
121	$D^\pm \to K\pi\pi$	151	$D^{*0} \to D^0\gamma, D^0 \to K\pi\pi^0$
122	$D^\pm \to K_s\pi\pi^0$	152	$D^{*0} \to D^0\gamma, D^0 \to K\pi\pi\pi$
123	$D^\pm \to K\pi\pi\pi^0$	153	$D^{*0} \to D^0\gamma, D^0 \to K_s\pi\pi$
124	$D^\pm \to K_s\pi\pi\pi$	155	$D^{*0} \to D^0\gamma, D^0 \to \ell X$
125	$D^\pm \to \ell X$		
130	$D^* \to D^0\pi, D^0 \to K\pi$		
131	$D^* \to D^0\pi, D^0 \to K\pi\pi^0$		
132	$D^* \to D^0\pi, D^0 \to K\pi\pi\pi$		
133	$D^* \to D^0\pi, D^0 \to K_s\pi\pi$		
135	$D^* \to D^0\pi, D^0 \to \ell X$		

Table B.2: List of the D meson decay modes. The symbol X corresponds to an arbitrary particle and $\ell = \{e, \mu, \tau\}$

B mode	Decay	B mode	Decay
1	$B \to D\pi$	20	$B \to DK\pi\pi\pi^0\pi^0$
2	$B \to DK$	22	$B \to D\pi\pi\pi\pi\pi$
3	$B \to D\pi\pi^0$	23	$B \to DK\pi\pi\pi$
4	$B \to DK\pi^0$	24	$B \to DKK\pi\pi\pi$
5	$B \to DK_s\pi$	25	$B \to D\pi\pi\pi\pi\pi\pi^0$
6	$B \to DKK_s$	26	$B \to DK\pi\pi\pi\pi^0$
7	$B \to D\pi\pi^0\pi^0$	27	$B \to DKK\pi\pi\pi^0$
8	$B \to DK\pi^0\pi^0$	31	$B \to D^*\pi, D^* \to D\pi^0$
9	$B \to D\pi\pi\pi$		
10	$B \to DK\pi\pi$		
13	$B \to DK\pi\pi\pi^0$		
15	$B \to D\pi\pi^0K_s$		
16	$B \to DK\pi^0K_s$		
17	$B \to DK\pi^0\pi^0K_s$		
19	$B \to D\pi\pi\pi\pi^0\pi^0$		

Table B.3: List of the B meson decay modes

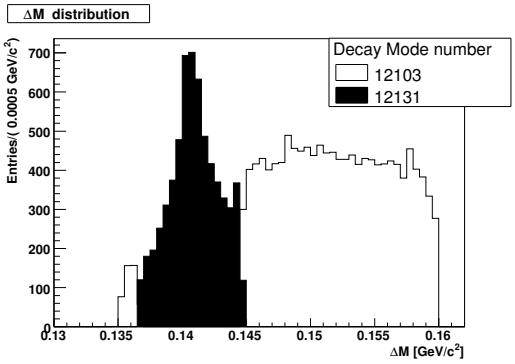

Figure B.1: ΔM spectrum for the reconstructed decay $B^0 \to D^{*-}\pi^+$. The colors distinguish the different decay mode numbers which are assigned to the decay $B^0 \to D^{*-}\pi^+$. For example, the decay mode number 12131 is characterized by ΔM in the range $0.1366\,\mathrm{GeV}/c^2 < \Delta M < 0.1446\,\mathrm{GeV}/c^2$.

Appendix C

π^0 Momentum Distributions

This appendix shows a summary of the momentum spectra of the low energy π^0 mesons in the considered decays applying all reconstruction criteria as described in chapter 4. The generated π^0 momentum distribution for the generated decay $B^0 \to D^{*-}\pi^+$, reconstructed as $B^0 \to D^-\pi^+$, is shown in Fig. C.1.
The reconstructed momentum spectrum of the π^0 for the reconstructed decay $B^0 \to D^{*-}\pi^+$ on the Monte Carlo simulation and on data is illustrated in Fig. C.2 All spectra consist of signal and background events.

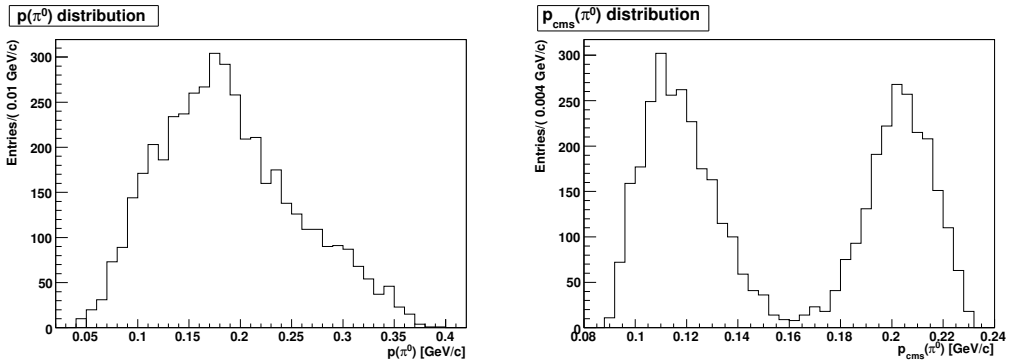

(a) laboratory frame (b) $\Upsilon(4S)$ rest frame

Figure C.1: Simulated π^0 momentum spectrum for the generated decay $B^0 \to D^{*-}\pi^+$ which is reconstructed as $B^0 \to D^-\pi^+$ in the (a) laboratory frame and (b) $\Upsilon(4S)$ rest frame.

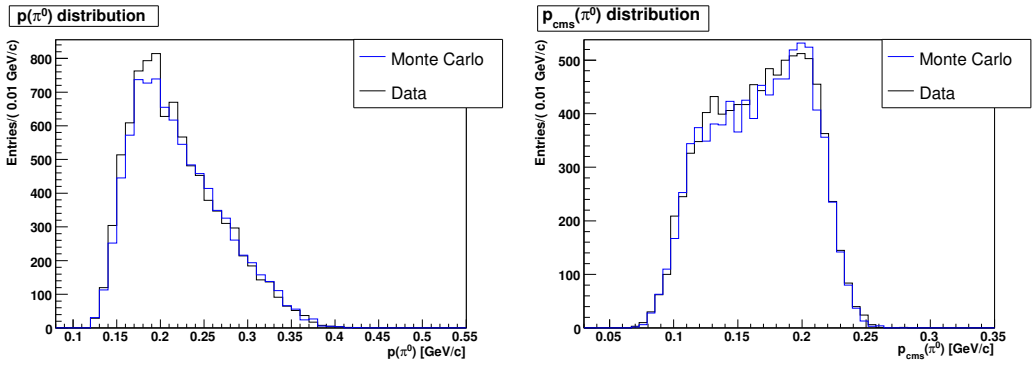

(a) laboratory frame (b) $\Upsilon(4S)$ rest frame

Figure C.2: Reconstructed π^0 momentum spectrum for the reconstructed decay $B^0 \to D^{*-}\pi^+$ on the Monte Carlo simulation and on data in the (a) laboratory frame and (b) $\Upsilon(4S)$ rest frame .

Bibliography

[1] S. Hawking, *A Brief History of Time*, Bantam Books, 1988.

[2] N. Cabibbo, *Unitary Symmetry and Leptonic Decays*, Phys. Rev. Lett. **10 12**, 531–533 (Jun 1963).

[3] M. Kobayashi and T. Maskawa, *CP Violation in the Renormalizable Theory of Weak Interaction*, Prog. Theor. Phys. **49**, 652–657 (1973).

[4] e. Harrison, P. F. and e. Quinn, Helen R. (*BABAR*), *The BABAR physics book: Physics at an asymmetric B factory* Papers from Workshop on Physics at an Asymmetric B Factory (*BABAR*Collaboration Meeting), Rome, Italy, 11-14 Nov 1996, Princeton, NJ, 17-20 Mar 1997, Orsay, France, 16-19 Jun 1997 and Pasadena, CA, 22-24 Sep 1997.

[5] B. Aubert *et al.* (*BABAR*), *The BABAR detector*, Nucl. Instrum. Meth. **A479**, 1–116 (2002), hep-ex/0105044.

[6] W.-M. Yao *et al.*, *Review of Particle Physics*, Journal of Physics G 33, 1+ (2006), http://pdg.lbl.gov.

[7] B. Aubert *et al.* (*BABAR*), *A measurement of the total width, the electronic width, and the mass of the* $\Upsilon(10580)$ *resonance*, Phys. Rev. **D72**, 032005 (2005), hep-ex/0405025.

[8] M. Allen (*BABAR*), *A measurement of the* π^0 *efficiency using* $\tau \to \rho\nu$ *and* $\tau \to \pi\nu$ *decays* , *BABAR* Analysis Document 870v3.

[9] V. Klose (*BABAR*), *A measurement of the* π^0 *efficiency using* D^0 *decays into* $K^{\mp}\pi^{\pm}\pi^0$, *BABAR* Analysis Document 1194v1.

[10] D. del Re (*BABAR*), *Semi-Exclusive B reconstruction* , *BABAR* Analysis Document 271v1.

[11] *BABAR Physics Releases web page*, http://www.slac.stanford.edu/BFROOT/www/Physics/PhysicsReleases/.

[12] A. Ryd, `EvtGen` *documentation*, http://www.slac.stanford.edu/BFROOT/www/Physics/Tools/generators /EvtGen/EvtGen.html.

[13] T. Sjoestrand, *PYTHIA 5.7 and JETSET 7.4 Physics and Manual*, http://dino.ip.fmph.uniba.sk/pythia_html3/pythia57.html.

[14] `GEANT` *4 web page*, http://geant4.web.cern.ch/geant4/.

[15] *BABAR Neutral Reconstruction AWG web page, Neutrals Corrections*, http://www.slac.stanford.edu/BFROOT/www/Physics/Analysis/AWG/Neutrals/validation/recipie18.html.

[16] *ROOT web page*, http://root.cern.ch/.

[17] *BABAR Particle Identification web page, Likelihood Selectors*, http://www.slac.stanford.edu/BFROOT/www/Physics/Tools/Pid/Hadrons/Description_of_the_LH_selectors.html.

[18] G. C. Fox and S. Wolfram, *Observables for the Analysis of Event Shapes in e^+e^- Annihilation and Other Processes*, Phys. Rev. Lett. **41 23**, 1581–1585 (Dec 1978).

[19] W. P. W. S. McCulloch, *A Logical Calculus of Ideas Immanent in Nervous Activity*, Bulletin of Mathematical Biophysics **5**, 115–133 (1943).

[20] F. Rosenblatt, *The Perceptron: A probabilistic model for information storage in the brain*, Psychological review **65**, 386–408 (1958).

[21] R. A. Fisher, *The use of multiple measurements in taxonomic problems*, Annals of Eugenics **7 2**, 179–188 (1936).

[22] *TMVA web page*, http://tmva.sourceforge.net/.

[23] S. Brandt, C. Peyrou, R. Sosnowski and A. Wroblewski, *The Principal axis of jets. An Attempt to analyze high- energy collisions as two-body processes*, Phys. Lett. **12**, 57–61 (1964).

[24] J. D. Bjorken and S. J. Brodsky, *Statistical Model for Electron-Positron Annihilation into Hadrons*, Phys. Rev. D **1 5**, 1416–1420 (Mar 1970).

[25] P. Gay, B. Michel, J. Proriol and O. Deschamps, *Tagging Higgs bosons in hadronic LEP2 events with neural networks* (1995), prepared for 4th International Workshop on Software Engineering and Artificial Intelligence for High-energy and Nuclear Physics (AIHENP 95), Pisa, Italy, 3-8 April 1995.

[26] K. Ulmer, $m_{\rm ES}$ *corrections*, http://babar-hn.slac.stanford.edu:5090/HyperNews/get/physAnal/2450.html.

[27] *MINUIT Reference Manual (Version 94.1)*, http://wwwasdoc.web.cern.ch/wwwasdoc/minuit/minmain.html.

[28] R. J. Barlow, *Statistics*, John Wiley & Sons, 1989.

[29] L. Lyons, *Statistics for nuclear and particle physicists*, Cambridge University Press, 1986.

[30] *CDF Statistics Committee web page*, http://www-cdf.fnal.gov/physics/statistics/statistics_faq.html.

[31] D. H. Perkins, *Hochenergiephysik*, Addison-Wesley (Deutschland), 1990.

[32] F. Halzen and A. D. Martin, *Quarks and leptons*, John Wiley & Sons, 1984.

Danksagung

Zu Beginn möchte ich mich ganz besonders bei meinen Eltern für die Unterstützung während der Studienzeit bedanken. Weiterhin danke ich meiner lieben Maja für ihre seelische und moralische Unterstützung in der Prüfungszeit und während der Diplomarbeit.

Des weiteren möchte ich mich bei Dr. Heiko Lacker und Prof. Michael Kobel für das interessante Diplomthema, sowie die erstklassige Betreuung während der Bearbeitung bedanken. Sie haben sich immer die Zeit genommen, meine Fragen ausführlich zu beantworten. Außerdem bedanke ich mich bei allen Doktoranden und Diplomanden der *BABAR* Gruppe in Dresden, die mir vor allem bei technischen Schwierigkeiten schnell weiterhelfen konnten. Hervorzuheben ist dabei Dr. Thorsten Brandt, ohne dessen Engagement in der Anfangsphase die Diplomarbeit in diesem Rahmen nicht möglich gewesen wäre. Verena Klose sei für ihr geduldiges Korrekturlesen meiner Arbeit gedankt.

Für das reibungslose Funktionieren der Institutsrechner, sowie deren Wartung danke ich im Besonderem Andreas Petzold und Dr. Rainer Schwierz.

Erklärung

Hiermit versichere ich, daß ich die vorliegende Arbeit selbständig und ohne Benutzung anderer als der angegebenen Hilfsmittel angefertigt habe. Die aus fremden Quellen direkt oder indirekt übernommenen Resultate sind als solche kenntlich gemacht.

Dresden, den 19.03.2007 Clemens Räder